Monochromator-based absolute calibration of radiation thermometers for thermodynamic temperature measurements of high-temperature fixed-points

vorgelegt von
M.Sc. Thada Keawprasert
aus Trang (Thailand)

Von der Fakultät IV – Elektrotechnik und Informatik
der Technischen Universität Berlin
zur Erlangung des akademischen Grades
Doktor der Ingenieurwissenschaften
- Dr.-Ing. -

genehmigte Dissertation

Promotionsausschuss:

Vorsitzender: Prof. Dr. Raisch
Berichter: Prof. Dr. Völker
Berichter: Prof. Dr. Schierz
Berichter: Prof. Dr. Hartmann

Tag der wissenschaftlichen Aussprache: 11. August 2011

Berlin 2011
D 83

Die Messunsicherheit bei der Realisierung der Internationalen Temperaturskala (ITS-90) nimmt oberhalb der Kupfererstarrungstemperatur von 1084,62 °C stetig zu, da die Skala hier über eine Extrapolation basierend auf dem Planckschen Strahlungsgesetz und ausgehend von den Temperaturen des erstarrenden Silber, Gold oder Kupfers definiert ist. Alternativ dazu erlaubt die absolute radiometrische Strahlungsmessung eine direkte Temperaturbestimmung rückgeführt auf ein kryogenes elektrisches Substitutionsradiometer als primäres Detektornormal. Aus diesem Grund wurde ein neuer auf einem Monochromator und einem Ulbrichtkugelstrahler basierender Vergleichsmessplatz entwickelt, der es erlaubt die spektrale Empfindlichkeit von Hochtemperatur-Strahlungsthermometern mit einer relativen Standardunsicherheit im sichtbaren Wellenlängenbereich von unter 0,17 % (k = 1) zu kalibrieren. An einem lasergestützten Messplatz konnte eine relative Standardunsicherheit der spektralen Empfindlichkeit von unter 0,14 % (k = 1) erreicht werden. Die daraus resultierende geringe Messunsicherheit der Temperaturbestimmung von 0,14 K und 0,16 K konnte an einem Goldfixpunkt (1337,33 K) bestätigt werden. Mit dem absolut kalibrierten Strahlungsthermometer wurden die thermodynamische Phasenübergangstemperaturen der eutektischen Fixpunkte Co-C (1597 K), Pt-C (2012 K) und Re-C (2748 K) mit einer Messunsicherheit (k = 1) von maximal 0,7 K direkt bestimmt.

Schlagworte: Internationale Temperaturskala, Thermodynamische Temperatur, Strahlungsthermometer, Detektorradiometrie, Hochtemperaturfixpunkte

According to the International Temperature Scale of 1990 (ITS-90), the temperature (T_{90}) above the copper freezing temperature (1084 °C) is realized using Planck's law and one of the silver, gold or copper fixed-point as the reference source. Due to this extrapolation method the realization uncertainty at high temperatures is much higher than at lower temperatures. An alternative to the dissemination of temperature based upon the ITS-90 is the direct realization of thermodynamic temperatures (T) by means of absolute spectral radiometry with high accuracy radiation thermometers, whose spectral radiance responsivity is traceable to the optical power measured by the PTB primary cryogenic radiometer.

In this work, for the first time a new monochromator-integrating sphere based spectral comparator facility was developed and fully investigated to calibrate radiation thermometers of the type LP3 in terms of absolute spectral radiance responsivity in the wavelength range from 370 nm to 1100 nm. The absolute responsivity calibration was performed by using a 75 W Xenon lamp with a reflective mirror and imaging optics to achieve a relative measurement uncertainty lower than 0.17 % (k = 1). The absolute calibration of the same radiation thermometer was also performed at a tuneable laser-based facility with a relative measurement uncertainty of 0.14 % (k = 1) in order to compare the performance and accuracy of both facilities. With the absolutely calibrated radiation thermometer, a thermodynamic temperature uncertainty of 0.14 K and 0.16 K can be achieved at 1337.33 K with the calibration results at the laser-based facility and the new monochromator based facility, respectively.

To verify the calibration accuracy, the absolutely calibrated radiation thermometer was used to measure the thermodynamic freezing temperatures of the PTB primary gold-and copper fixed-point blackbodies, resulting in T-T_{90} values for the gold and copper fixed-point temperatures. Applying the same radiation thermometer, the thermodynamic temperatures of the melting points of Co-C, Pt-C and Re-C eutectic fixed-point cells in WP4 of the CCT-WG5 high-temperature fixed-point research plan were directly determined in radiance mode with standard uncertainties (k = 1) below 0.7 K at 2748 K. Finally measurement results are presented for each material and compared with previous determinations of other national metrology institutes, which could be useful for a revision of the International Temperature Scale above 1300 K in the near future.

Keyword: International Temperature Scale of 1990, thermodynamic temperature, radiation thermometer, detector-based radiometry, high-temperature fixed-points

Content

Parts of this work have been published in the following publications:

1. K. Anhalt, A. Zelenjuk, D. R. Taubert, T. Keawprasert, J. Hartmann, New PTB setup for the absolute calibration of the spectral responsivity of radiation thermometers, Int J Thermophys **30**, 192-202 (2009)

2. T. Keawprasert, K. Anhalt, D. R. Taubert, A. Abd-ElMageed, A. Sperling, J. Hartmann, Absolute calibration of spectral responsivity for a radiation thermometer, in *Proceeding of NEWRAD2008*, Daejeon, South Korea, P283

3. T. Keawprasert, K. Anhalt, D. R. Taubert, J. Hartmann, Monochromator-based absolute calibration for radiation thermometers, International Journal of Thermophysics DOI 10.1007/s10765-011-1031-x (2011)

1 Introduction

The major challenges for mankind in the 21st century are climate change and rapidly increasing energy prices. As far as global warming is concerned, a solution can only be found in the reduction of greenhouse gas emissions, i.e. by decreasing the consumption of fossil fuels and the introduction of renewable energy sources. To achieve this aim, the energy efficiency for a wide variety of processes has to be improved. These processes range from private households, to industrial sites and scientific applications. A key area are energy intensive high-temperature processes, which are often run ineffectively due to heat loss combined with imprecise temperature measurement and control as these processes are found in harsh industrial environments and are often difficult to access. In particular, this is valid for the measurement and control of temperatures above 1000 °C. The technologies in this temperature regime require a lot of energy for heating, thus a precise high-temperature measurement is essential for an increase of energy efficiency and a reduction of the environmental impact. Such high-temperature processes with a need for a more accurate measurement of temperature can be found in diverse industrial areas such as steel making, ceramics, semiconductors, aerospace, novel nuclear power generation and lighting industry. An outstanding example are tungsten-filament lamps, whose filament temperature (~2800 °C) affects their efficiency, but also their life time.

Besides the importance of energy efficiency in these industries, an improved high-temperature measurement has a fundamental impact on our knowledge of the earth's most important energy source, the sun, a hot thermal source of about 5500 °C. The solar irradiance fluctuates with the 11-year-solar-cycle at the level of 0.1 % and as such has a significantly influence on the global radiation budget and the earth's surface temperature. It is believed that in time intervals of decreasing solar irradiance, the anthropogenic effects for the increasing surface temperature will be compensated [1]. In the laboratory, a typical high-temperature blackbody furnace can reach a maximum temperature of around 3000 °C. At this temperature and for a wavelength of 555 nm, a 0.1 % variation in irradiance corresponds to a temperature change of 0.4 K.

In spite of the technological importance in this temperature range, the temperature measurement is principally limited with the current definition of the International Temperature Scale. Presently the temperature scale above 961.78 °C is realized by relative radiation thermometry i.e. by comparison with respect to one of the freezing temperatures of silver (961.78 °C), gold (1064.18 °C) and copper (1084.62 °C) according to the International Temperature Scale of 1990 (ITS-90) [2]. Unfortunately, the uncertainty associated with the method ascribed in the ITS-90 propagates drastically towards higher temperatures with the square of the ratio of the measured temperature to the reference fixed-point temperature. Moreover, the ITS-90 scale is also non-unique due to the choice of any one of the three fixed-points as the basis for the scale. For improving the accuracy of the temperature measurement at high temperatures, more fixed-points at temperatures above the freezing temperature of Cu are required to realize a high-temperature scale via an interpolating procedure. Therefore, high-temperature fixed points are the topic of recent

scientific projects and the developed solution so far is based on the successful implementation of metal-carbon (M-C) eutectic alloys as the fixed-point material [3]. However, before implementing these novel high-temperature fixed-points into the International Temperature Scale, the thermodynamic temperature of their phase-transition must be assigned with the lowest possible measurement uncertainty to yield a reduced uncertainty in practical thermometry and radiometry. This can only be achieved using thermodynamic temperature measurement results by means of absolute radiometry performed at national metrology institutes (NMIs) around the world.

An alternative to the ITS-90 at high temperatures is a direct realization of thermodynamic temperature by means of absolute radiometry. At the Physikalisch-Technische Bundesanstalt (PTB), such a direct measurement of the thermodynamic temperature is well established using filter radiometers (FRs) in irradiance mode. With its low measurement uncertainty this method can be used to test the ITS-90 for systematic discrepancies with respect to the thermodynamic temperature [4]. However, these non-imaging filter radiometers require a thermal source with a large opening, as precision apertures are used to define the optical geometry and an increasing diffraction occurs with smaller aperture size. Typically, a furnace aperture of about 20 mm in diameter is used. In contrast to this, high-temperature fixed-points have typically an opening of about 3 mm in diameter [5]. Such a small diameter opening is necessary, as the overall cell dimensions should be adequate to use these fixed-points in existing high-temperature furnaces and the diameter to length ratio of the fixed-point cavity, which defines its emissivity, should be kept smaller than 1/10. For larger apertures, a longer cavity and thus a fixed-point cell with larger dimensions is required to meet this criterion. Therefore, as advancement from the non-imaging filter radiometer technique – which has a large field-of-view – a more practical measurement of the thermodynamic temperature should be based on a measurement of spectral radiance. This can be realized with optical imaging systems, such as a radiation thermometer equipped with a lens, that allows to sense radiation from a small target area such as the small opening fixed-point cavity.

For this purpose, a novel experimental scheme has been developed and realized within this work that allows the calibration of an imaging filter radiometer or radiation thermometer with respect to absolute spectral radiance responsivity traceable to the primary cryogenic radiometer of PTB. Based on the experience in the calibrations of the filter radiometers with respect to absolute irradiance responsivity [4] and the limited applicability of laser radiation when narrow-band interference filter are characterized (as it is the case for most radiation thermometers in the high temperature range), the new set-up is based on a monochromator system and a broadband light source by applying an integrating sphere as a homogeneous-lambertian source. A Si trap detector allows the determination of the optical flux from an integrating sphere, in which the spectrally resolved radiation by the monochromator is coupled. Both, the monochromator and the light source had to be optimized to achieve the high optical output power necessary for this experimental scheme. A thorough characterization and optimization of the integrating sphere is essential, as the field of view for trap detector and radiation thermometer differs considerably.

At PTB, high accuracy radiation thermometers of type LP3 have been commonly used to measure the temperature of blackbodies, especially for fixed-point blackbodies, because of their small target size and low influence due to object size, i.e. low size-of-source effect. For an application in high temperature measurements, a 650 nm interference filter has been selected for these radiation thermometers. Therefore the LP3 radiation thermometer will be carefully investigated and calibrated absolutely with this filter at the newly developed set-up. The scope of this work is not to develop and characterize the M-C eutectic blackbody cells, but to determine the thermodynamic temperatures of existent M-C fixed-point blackbodies using an absolutely calibrated radiation thermometer.

The present work is organized in the following manner. First, the principles of temperature measurement are presented in Chapter 2, and then the objectives for this new way of dissemination of temperature using an absolutely calibrated radiation thermometer are formulated (Chapter 3). Chapter 4 deals with the development of the absolute calibration set-up for radiation thermometers. Calibration results for a radiation thermometer at the developed set-up are described in Chapter 5. Methods for thermodynamic temperature determination of Au and Cu fixed-point blackbodies by the absolutely calibrated radiation thermometer are the topic of Chapter 6. Finally, the determined thermodynamic temperatures of the novel M-C high-temperature fixed-points are presented in Chapter 7.

2 Theory

In this chapter, the theory and the fundamental concepts for this work will be described.

2.1 Temperature and its measurement

Temperature is one of the most important physical quantities, which affects our everyday life from the weather to industrial processes. Excepting from time, temperature seems to be the most frequently measured physical quantity. For industrial processes, temperature plays an important role as an indicator of the condition of a product, both in manufacturing and in quality control. That is accurate temperature measurements can significantly increase the value, effectiveness and quality of a product. For this reason, the International Temperature Scale has been established since 1927 to harmonize the world wide practical temperature measurement.

2.1.1 Thermodynamic temperature

Thermodynamic temperature, symbol T, is a fundamental physical quantity indicating the average translational kinetic energy associated with the disordered microscopic motion of atoms and molecules. According to the so called zeroth law of thermodynamics, a system of $2T$ can not be realized by joining two systems of T, i.e. temperature is an intensive quantity, not an extensive quantity like mass or length.

Based on the second law of thermodynamics, it is well known that the lowest possible thermodynamic temperature is limited, yielding the absolute zero temperature of 0 K. In 1854, William Thomson, later known as Lord Kelvin, proposed a new concept for realization a temperature scale from that zero temperature to one fixed-point temperature. This concept has been used about 100 years later to define the unit of thermodynamic temperature in 1954 by the 10^{th} General Conference on Weights and Measures (CGPM), which selected the triple point of water as a fundamental fixed point with an assigned temperature value of exactly 273.16.

The unit of thermodynamic temperature is the kelvin, symbol K, defined by the 13^{th} CGPM (1967/1968) as follows

> *The kelvin, unit of thermodynamic temperature, is the fraction 1/273.16 of the thermodynamic temperature of the triple point of water.*

This definition can be realized by the use of water triple point cells, yielding an agreement on temperature within ± 50 μK for good cells but possible to > 200 μK for poor cells. Because this definition is based on the property of a substance, it is well known that differences on temperature between individual cells result from the isotropic composition of the water. In 2005, the International Committee for Weights and Measures (CIPM)

clarified the definition of the triple point of water by specifying the isotopic composition of the water to be that of Vienna Standard Mean Ocean Water (V-SMOW) [6].

It is well known to express temperature, but not thermodynamic temperature, in terms of its difference from the ice point temperature T_0 = 273.15 K. This difference is the so called Celsius temperature, symbol *t*, defined by

$$t/°C = T/K - 273.15.$$

The unit of the Celsius temperature is the degree Celsius, symbol °C, which is by this definition equal in magnitude to the unit kelvin. The degree Celsius is probably preferred to use in everyday life and industrial, more than in the temperature metrology communities.

In near future, a new definition of the kelvin will no longer be based on any artefact or materials property, but linked to a fundamental constant, similar to the second or the metre. Since the temperature is related to the thermal energy with the Boltzmann constant via *kT*, the kelvin will be defined by adopting the best possible value of the Boltzmann constant as the basis of the unit of temperature in the near future. For example: 1) The kelvin is the change of thermodynamic temperature that results in a change of thermal energy *kT* by exactly 1.380 650 5 × 10^{-23} J, or 2) The kelvin, unit of thermodynamic temperature, is such that the Boltzmann constant is exactly 1.380 650 5 × 10^{-23} J / K [7].

It is worth noting that the assigned thermodynamic temperature at the water triple point was approximately defined by means of temperature measurement via fundamental relations and physical constants, known as primary thermometry [2]. In addition, the triple point of water cell alone is not a sufficient condition to allow other temperatures to be measured, it is also necessary to have a practical description for temperature measurement. Therefore it is worth to provide the basis of the primary thermometry and also the practical temperature scale in the next sections.

2.1.2 Primary thermometry

For measuring the thermodynamic temperature, a physical system whose equation of state is accurately known, must be chosen and the variables of state as the temperature is changed, are measured. For example: *PV= nRT*, when *n* and *V* are controlled parameters and *R* is the gas constant, then the measured variable is the pressure *P*, which changes by varying the temperature *T*. This is the concept of the most popular version of gas thermometry, the constant volume gas thermometry (CVGT), which is used to measure the thermodynamic temperature both, in low temperature ranges down to 4.2 K [8] and the middle temperature range up to 904 K [9]. In addition, CVGT is also a prescribed interpolation method of the current International Temperature Scale at low temperatures. However the accuracy of this method is limited by the need of the mole number of the used gas, and also gas sorption and thermal expansion at high temperatures.

Other gas thermometry methods are acoustic gas thermometry (AGT), which detects the speed of sound as a function of temperature, applied in temperature ranges from 4 K to 552 K [10, 11], and dielectric constant gas thermometry (DCGT) determining the dielectric constant as a function of temperature, used especially in the very low temperature range from 4.2 K to 24.6 K [12]. Since both, AGT and DCGT, are based on the variation of temperature of an intensive properties of the gas (speed of sound and dielectric constant), it is possible to obtain an accuracy in the order of parts per million.

At high temperatures, as the accuracy obtained by these gas thermometry methods decreases, other types of primary methods, independent of the gas law, have been used, e.g. Johnson noise thermometry and radiation thermometry. Measurements by means of noise thermometry have been used over the temperature range from the Zn point (419.527 °C) [13] to the Cu point (1084.62 °C) and even higher [14]. However, long time measurements are required to achieve the highest accuracy.

Radiation thermometry is a general concept, which can be realised in different schemes, depending on the part of the emitted thermal radiation used for the actual measurement. Total radiation thermometry, which uses nearly the whole spectrum of the emitted thermal radiation, was originally used to determine the Stefan-Boltzmann constant with high accuracy [15] although not as successfully as intended with respect to the accuracy and therefore is not routinely practiced for the purpose of practical temperature measurement [16], because it depends on a lot of parameters and is therefore too difficult and extremely time- consuming.

In contrast to the method above, the spectral radiation thermometry based on Planck's law of thermal radiation, which uses only a small spectral part of the emitted thermal radiation, has been successfully applied over a wide temperature range from 730 K up to over 3,200 K [5, 17, 18].

An overview over the fundamental physical laws for these primary thermometers is given in Table 2.1.

Table 2.1 Summary of the different methods of primary thermometry: u_0 is the zero-frequency zero-pressure limit; M is the molar mass of the gas; R is the gas constant; γ_0 is the ratio of the heat capacity; k the Boltzmann constant; ε_0 the dielectric constant in vacuum; α_0 is the static electric dipole polarizability; V is the mean square electrical noise voltage across a resistor R in a frequency band Δf**;** L is the total radiance; c_0 is the speed of light in vacuum, h is the Planck constant

Primary method	Physical law
Acoustic gas thermometer	$u_0 = \sqrt{\frac{\gamma_0 RT}{M}}$ (2.1)
Dielectric constant gas thermometer	$p = kT\frac{\varepsilon - \varepsilon_0}{\alpha_0}$ (2.2)
Quasi-spherical cavity-resonator thermometer	$p = kT\frac{(n^2-1)\varepsilon_0}{\alpha_0}$ .....(2.3)
Noise thermometer	$\overline{V}^2 = 4kTR\Delta f$ ……..(2.4)
Total radiation thermometer	$L = \frac{M}{\pi} = \frac{2\pi^4 k^4}{15c_0^2 h^3}T^4$ …...…(2.5)

The purpose of most of the primary thermometry methods is to assign the best thermodynamic temperature value to the practical fixed-points for improving the accuracy of the current International Temperature Scale, and determining the Boltzmann constant with the lowest possible uncertainty, as well as redefining the Kelvin in the *Mise en pratique* guideline [19]. Two recent reviews on the status of the primary thermometry can be found in Rusby et al. [20] and Fischer et al. [7].

2.1.3 Practical temperature scale: the International Temperature Scale of 1990

Since the primary thermometry methods are time consuming and costly, a series of reproducible fixed-points, whose thermodynamic temperatures were determined by primary thermometry, are used to realize the practical temperature scale for the day-to-day work, the so-called International Temperature Scale. The International Temperature Scale is revised regularly by taking account of advances in science and technology to approximate the measured temperatures of these fixed-points closest to the corresponding thermodynamic temperatures. Currently, the International Temperature Scale of 1990 (ITS-90), adopted by the CIPM in 1989, and the Provisional Low Temperature Scale (PLTS-2000), adopted by the CIPM in 2000 are used as important parts of the International System of Units to support science and industry.

For the ITS-90, these defining temperatures are in the temperature range from the vapour pressure point of helium (0.65 K) up to the copper freezing point (1377.33 K). Between these fixed-point temperatures, a variety of standard thermometers are used to interpolate

the temperature scale for a particular sub-range of temperature by the following techniques defined in ITS-90 documents [2] as illustrated in **Fig**. 2.1. The measured temperatures obtained by means of the ITS-90 are the so-called T_{90} or t_{90} values, because they are only, even though the best possible, approximations to the thermodynamic temperatures. However, the kelvin and the degree Celsius are also the units of the ITS-90.

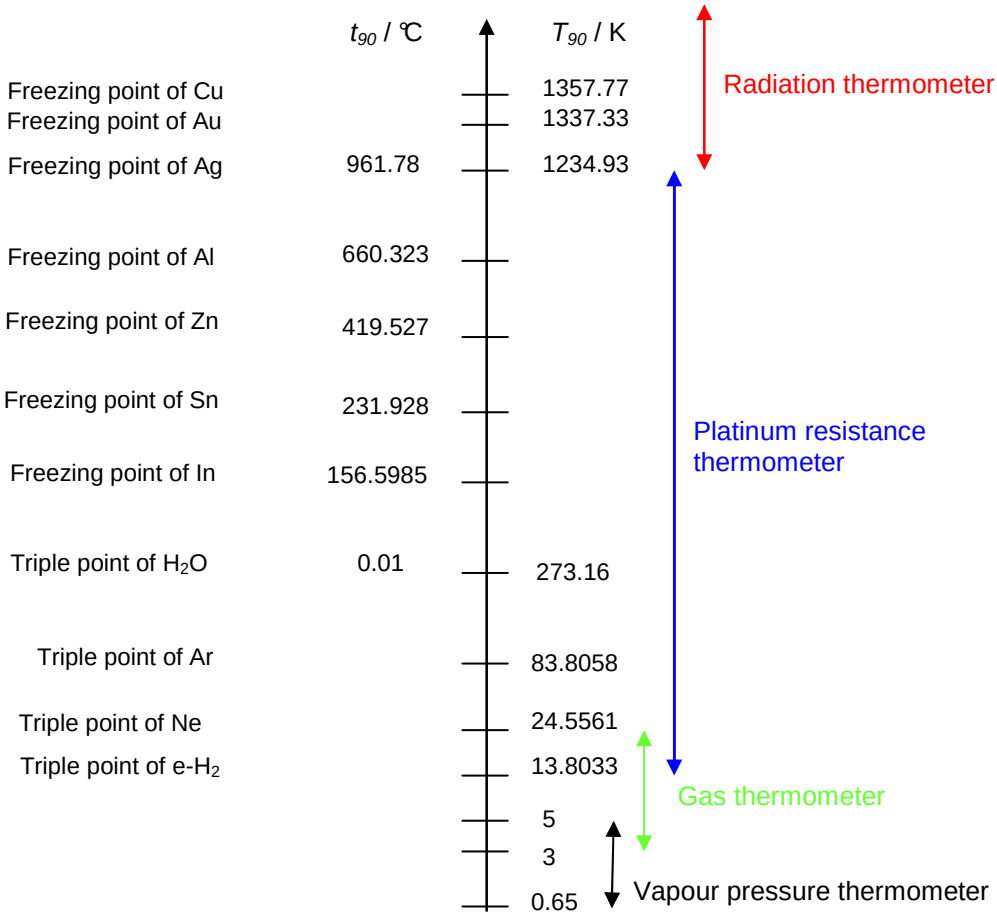

Figure 2.1 Illustration of the fixed-points and the interpolating instruments assigned in the ITS-90.

Briefly, in the range from 3 K to 24.5561 K, the ITS-90 can be realized by means of a helium gas thermometer. The interpolating instrument in the most important range from 13.8033 K (triple point of hydrogen) to 961.78 °C (freezing point of silver) is the platinum resistance thermometer. Above the silver freezing point, temperatures are determined with radiation thermometers using Planck's law and spectral radiance ratios to one of the Ag-, Au- or Cu freezing temperature blackbodies.

The PLTS-2000 provides an extension to the ITS-90 from 0.902 mK up to 1 K using the melt pressure of ^{3}He to define the T_{2000}, with closer approximation to the thermodynamic temperature than using the ITS-90 in the overlap region between 0.65 K and 1 K.

2.2 Blackbody radiation

Above the absolute zero temperature all objects emit an amount of energy via thermal radiation, depending on their temperature and the wavelength. Therefore, a measurement of thermal radiation can be applied to determine the object temperature in case the relation between the temperature and the thermal radiation is precisely known. In 1899, the spectral distribution of the blackbody radiation was studied in experiments performed at the Physikalisch-Technische Reichsanstalt (PTR) by *Lummer* and *Pringsheim* [21], and explained by *Max Planck* in 1900 [22], using Planck's law of thermal radiation. For an ideal blackbody, the spectral radiance, $L_{\lambda,s}$ – the radiant power per unit area per unit solid angle per unit wavelength interval - at any thermodynamic temperature T and wavelength λ, can be described by Planck's law of thermal radiation as follows

$$L_{\lambda,s}(\lambda,T)=\frac{2hc^2}{n^2\lambda^5}\left[\frac{1}{e^{hc/n\lambda kT}-1}\right], \tag{2.6}$$

where h is Planck's constant, k is the Boltzmann constant, c is the speed of light in vacuum and n is the refractive index of the medium in the optical path. This relation is based on the assumption that an oscillation of atoms or molecules which generates the thermal energy can not emit energy continuously but only in discrete energy steps.

Using a Taylor expansion, Planck's equation can be approximated by the classical thermodynamic theory based Wien's formula in case of high temperatures and short wavelengths ($hc/\lambda T >> kT$) by [23]

$$L_{\lambda,s}(\lambda,T)=\frac{2hc^2}{n^2\lambda^5}\left[\frac{1}{e^{hc/n\lambda kT}}\right], \tag{2.7}$$

and also in the opposite region of long wavelengths ($hc/\lambda T << kT$) by the Rayleigh-Jeans formula [24]

$$L_{\lambda,s}(\lambda,T)=\frac{2ckT}{n^2\lambda^4}. \tag{2.8}$$

According to these equations, it is evident that the thermodynamic temperature is directly related to the spectral radiance. Applying Planck's law, the spectral radiances for several temperatures are shown in Fig. 2.2.

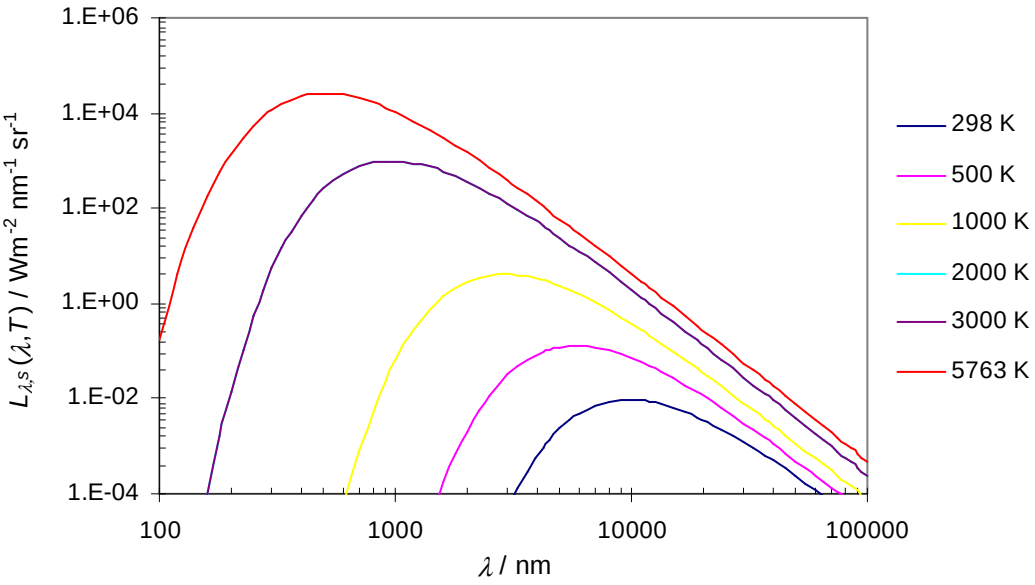

Figure 2.2 Spectral radiance emitted from a blackbody at some temperatures by using Planck's Law

According to Wien's approximation, the relation between the peak wavelength of the blackbody spectrum and the radiation wavelength can be described by Wien's law of displacement as

$$\lambda_{\max} T = 2897.7686 \qquad (\mu\text{m K}). \qquad (2.9)$$

It can be seen that a blackbody at temperature near 5800 K peaks in the visible range and emits significant radiation over a wide wavelength range from 200 nm to 3000 nm.

By integration over all wavelengths, the total power per unit area emitted by the ideal blackbody in all directions, E, is given by Stefan-Boltzmann law as follows [25, 26]

$$E = n^2 \sigma T^4, \qquad (2.10)$$

where σ is the Stefan-Boltzmann constant and n is assumed to be wavelength independent. However, it is a wider practice to determine the radiance of the blackbody within a small solid angle and use this equation in radiance form, i.e. $L = E/2\pi$.

Consequently, the blackbody temperature can be determined by a radiometric measurement of the spectral radiance based on Planck's law or total radiation based on Stefan-Boltzmann' law. However, the total radiation thermometry still has errors due to the difficulty in determining of some factors, limiting its accuracy in temperature measurement.

Based on Wien's approximation formula, the derivative of the spectral radiance of the blackbody radiation with respect to temperature can be used to calculate the change of temperature with respect to the relative change in the spectral radiance by

$$dT = \frac{\lambda T^2}{c_2} \cdot \frac{dL}{L}, \tag{2.11}$$

where c_2 is the second radiation constant, given by $c_2 = hc/k$. A meaning of the above equation in the field of metrology is that an uncertainty of the temperature measurement based on Planck's radiation law, depends on a relative uncertainty of the spectral radiance measurement and the quadrate of temperature as shown in **Fig**. 2.3.

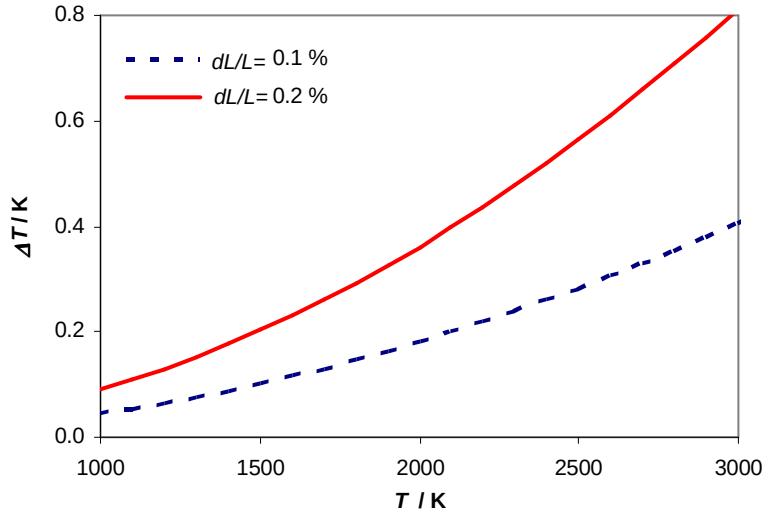

Figure 2.3 Change of temperature as a function of temperature for different uncertainties of the measured spectral radiance at a wavelength of 650 nm

In a similar way but based on the derivative of the spectral radiance of the blackbody radiation with respect to the wavelength, the relative change of the spectral radiance with wavelength is found according

$$\frac{dL}{L} = (-5 + \frac{c_2}{\lambda T}) \cdot \frac{d\lambda}{\lambda} \tag{2.12}$$

With (2.12) the accuracy of the spectral radiance measurement depends on the accuracy of the wavelength measurement.

For real objects, the amount of emitted thermal radiation depends on the emissivity of the object surface, which usually depends on wavelength, temperature and angle of view as

$$L_\lambda(\lambda, T, \theta) = \varepsilon(\lambda, T, \theta) L_{\lambda,s}(\lambda, T) \quad . \tag{2.13}$$

From the above equation, it is evident that the emissivity of any real surface can be measured by comparing the spectral radiance from the surface to that from a nearly ideal blackbody.

Based on Kirchhoff's law, a perfect absorber is also a perfect thermal emitter, an approximate blackbody can be technically realized by means of a cavity radiator with small opening to achieve an emissivity close to unity. A simple model for calculating the emissivity of a cavity radiator with an inner wall emissivity $\varepsilon_{\text{wall}}$, length l and radius r was given by [27] as

$$\varepsilon_{\text{cavity}} = 1 - \frac{1-\varepsilon_{\text{wall}}}{\varepsilon_{\text{wall}}} \cdot \frac{1}{1+(l^2/r^2)}. \tag{2.14}$$

This model shows that the cavity emissivity can be increased by increasing the wall emissivity and the cavity length, and reducing the cavity radius.

In reality, the temperature of any blackbody is not perfectly uniform, especially in the high temperature range. The best temperature uniformity can be achieved by selecting a blackbody material with high thermal conductivity and heat capacity, as well using a relative small opening of the blackbody. However, some applications i.e. remote sensing, need a large area blackbody radiator. In such cases more complex simulations based on sophisticated Monte-Carlo methods are required to consider the non-isothermal behaviour of the blackbody [28, 29, 30, 31]. The non-isothermal behaviour of the large aperture blackbody is due to the heat losses to the ambient via the opening and affects the spectral radiance as follows

$$L_\lambda(\lambda, T-\Delta T) \approx \varepsilon \left[1 - \frac{c_2}{\lambda T^2}\Delta T\right] L_{\lambda,s}(\lambda, T). \tag{2.15}$$

Thus, in order to calculate the emissivity of the non-isothermal blackbody, the temperature profile both, across the length and the aperture are required.

2.3 Radiation thermometry

In radiometry, a blackbody source with known emissivity can be used as a radiance standard by measuring its temperature, T_{90}, traceable to the ITS-90 or directly determining its thermodynamic temperature, T, by means of detector-based absolute radiometry using FRs, with the spectral responsivity traceable to the electrical SI unit Ampere. For application in radiation thermometry, the blackbody source with accurately known temperature can be also used to calibrate radiation thermometers. With detector-based radiometric standards achieving very small uncertainties within 0.01%, several NMIs now measure the thermodynamic temperature by radiometric means, rather than using an ITS-90 derived source-based radiance temperature scale [32]. However, the spectral responsivity of filter radiometers can drift, age and undergo step changes, which force these filter radiometers to be checked regularly, requiring expensive and time-consuming re-calibration.

In radiation thermometry, some reliable blackbody sources can be assigned to be reference sources, if the blackbody temperature is precisely known and highly reproducible, i.e. yield the same temperature at any time used. In practice, such reference blackbodies can be realized by means of fixed-point blackbodies, based on phase-transition temperatures of materials and a cavity radiator immersed in the material stored in a crucible. At the fixed-point temperature, such as melting or freezing points, the temperature remains stable within a very small temperature range, because the fixed-point material requires the additional amount of energy to melt completely, before it can be used to further increase its internal energy. Only fixed-point blackbodies with high reproducibility can be used as reference sources for source-based radiation thermometry.

2.3.1 ITS-90 fixed-point blackbody

Some fixed-point temperatures in the ITS-90, in particular the high-temperature fixed-points Ag, Au and Cu can be also established for radiation thermometry by implementing them into a blackbody, a so-called ITS-90 fixed-point blackbody. In fact, the lowest temperature of practical ITS-90 fixed-point blackbodies used is currently down to the In point (156.5985 °C) due to long wavelength limitation of the radiation thermometers used as transfer thermometers. The highest temperature of the ITS-90 fixed-point blackbodies is currently limited at the Cu freezing point (1084.62 °C), the highest fixed-point of the current ITS. Due to the contamination of graphite to fixed-point material at high temperatures, no higher temperature fixed-points are available in the current ITS.

Below the Cu freezing point, a radiance temperature scale approximating the ITS-90 can be realized by calibrating a radiation thermometer against at least three different fixed-point blackbodies, and an interpolation using of the Planck version of Sakuma-Hattori, resp. Jung-Verch equation as

$$S(T_{FP}) = C\frac{1}{\exp(\frac{c_2}{AT_{FP}+B})-1}, \tag{2.16}$$

where $S(T_{FP})$ is the signal of the radiation thermometer at any fixed-point temperature, T_{FP}, c_2 is the second Planck radiation constant, and A, B and C are the parameters for fitting. With the determined coefficients, an interpolated temperature scale can be disseminated over the whole temperature range of the used fixed-points. Using this multiple fixed-point method, the best measurement uncertainty is below 100 mK.

Above the Ag freezing point (971.78 °C), one of the Ag, Au or Cu fixed-point blackbody can be used as a reference source and a transfer radiation thermometer is required to extrapolate the temperature scale according the method prescribed in the ITS-90 using the Planck's law and the spectral radiance ratio

$$\frac{L_{\lambda,s}(T_{90})}{L_{\lambda,s}(T_{90}(x))} = \frac{\exp(c_2/\lambda T_{90}(x))-1}{\exp(c_2/\lambda T_{90})-1}, \tag{2.17}$$

where x refers to any one of the silver, the gold or the copper fixed-point temperature and $L_\lambda(T_{90})$ and $L_\lambda(T_{90}(x))$ are the spectral concentrations of the radiance of a blackbody at the wavelength λ at T_{90} and at $T_{90}(x)$ respectively. **Fig**. 2.4 shows the temperature scales obtained by the radiation thermometry.

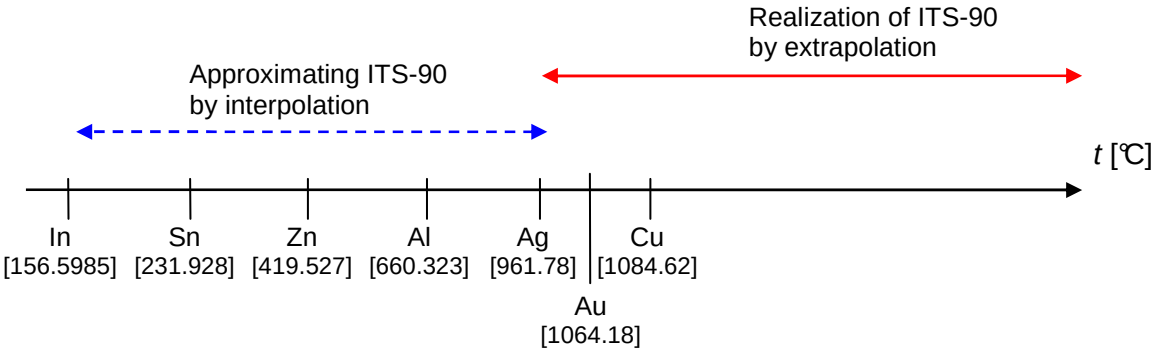

Figure 2.4 Radiance temperature scales obtained by the radiation thermometry according to the ITS-90 and approximating the ITS-90.

For temperatures above the fixed-point temperature, the temperature uncertainty according to the ITS-90 is theoretically limited by the temperature uncertainty of the reference fixed-points $U(T_{90}(x))$ and increases as the square of the temperature ratio due to the extrapolation equation by

$$U(T_{90}) = (\frac{T_{90}}{T_{90}(x)})^2 \cdot U(T_{90}(x)) \,. \qquad (2.18)$$

When the uncertainty contribution due to the transfer radiation thermometer is considered, the total uncertainty is still further increased.

Fig. 2.5 illustrates the temperature uncertainty according to the method prescribed in the ITS-90 calculated with Eq. 2.18. Even the best reference fixed-points with an expanded uncertainty in thermodynamic temperature of 100 mK for Au and a high accuracy transfer radiation thermometer with the relative expanded uncertainty of 0.2 % and an effective wavelength of 650 mm, the temperature uncertainty is still more than 1 K at 3200 K. Therefore the uncertainty of the ITS-90 in the high-temperature range has its main origin in the uncertainty of the radiation thermometer and in the thermodynamic temperature uncertainty of the reference fixed-point.

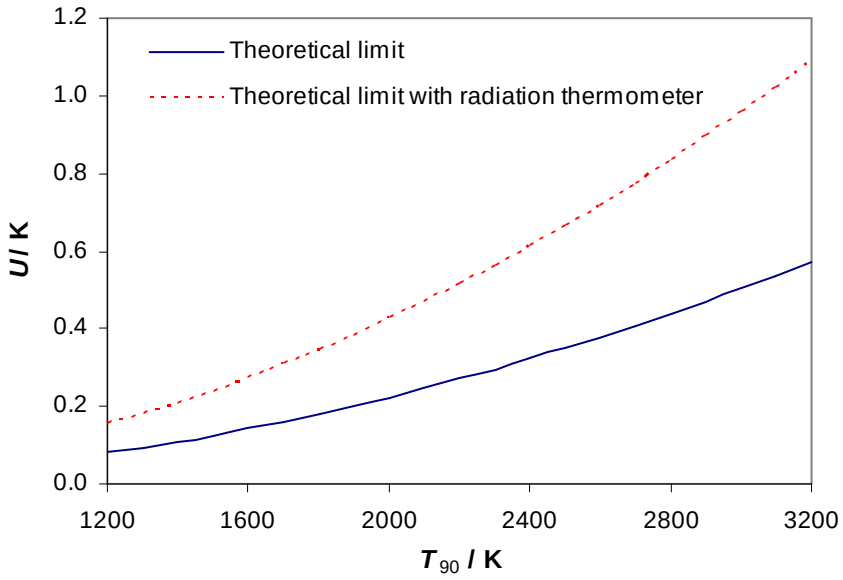

Figure 2.5 Theoretical approach to show the expanded uncertainty according to the ITS-90 at high temperatures

To reduce the temperature uncertainty above the Cu freezing point, it would be desirable to have an interpolation scale for a new temperature scale rather than the current extrapolation method used in the ITS-90. Furthermore, the temperature scale realized by the ITS-90 technique is non-unique, because different reference fixed-point blackbodies are allowed. Therefore, additional high-temperature fixed-point blackbodies with high reproducibility are highly desirable to be implemented in a future temperature scale.

2.3.2 High- temperature fixed-point blackbody

Due to the use of graphite as crucible material of the blackbody source, the contamination of graphite to the pure metal in the crucible may occur in particular at high temperatures, affecting the fixed-point temperature. Although some type of ceramics may be used for the construction of the crucibles up to 2000 °C, they suffer from high fragility and low emissivity for temperatures above 1500 °C. For this reason any pure metal fixed-point blackbody with a temperature higher than the copper point were not applied in the ITS-90 due to its poor reproducibility. However, already in 1996, the Consultative Committee for Thermometry (CCT) recommended that high-temperature fixed-points yielding a reproducibility of 100 mK at temperatures above 2300 K are highly desirable [33]. Since Yamada proved that the new type of high-temperature fixed-points based on metal carbon and metal carbide-carbon (M(C)-C) alloy can be used as possible fixed-point materials in 1999 [3], it is now possible to achieve high-temperature fixed-point cells with high reproducibility, satisfying the requirements of the CCT/CCPR recommendation [33].

The fixed-point temperature of such alloy is due to the phase equilibrium of metal and graphite, the well-known eutectic point. As long as the graphite of the crucible is as pure as the graphite of the eutectic, contamination due to graphite from the crucible will have no effect to the fixed-point temperature anymore, as graphite is also one component of the fixed-point material. A schematic of the phase diagram for a M-C and its freezing curve are shown in **Fig**. 2.6.

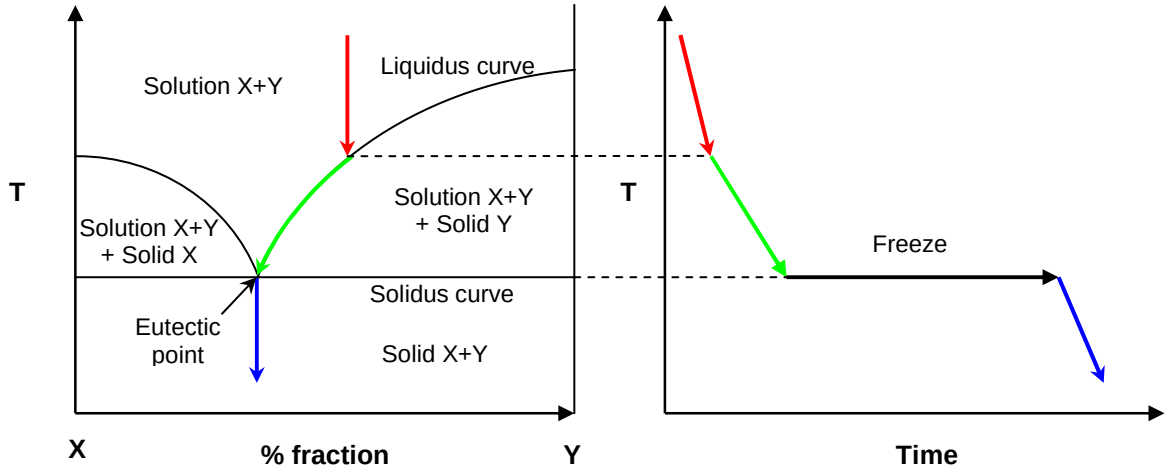

Figure 2.6 Typical schematic phase diagram and the freezing curve of a M-C eutectic point.

In brief, when the liquid mixture of metal and carbon with a carbon concentration above the eutectic composition is slowly cooled down until reaching the liquidus curve, then the carbon starts to freeze, increasing the metal content in the melt. When the system is cooled further, the liquid composition will move along the liquidus curve until reaching the eutectic point. At the eutectic point – similar to the freezing of one-component fixed-

points, although the liquid mixture is cooled down, the freezing liquid still stays at a constant temperature until the freezing is finished.

In case of the melting point, a typical melting curve illustrated in **Fig.** 2.7 can be described in the following. When the solid mixture is slowly heated up until reaching the solidus curve, the system will shift laterally along the solidus curve to the eutectic point since the carbon begins to melt, increasing the component of metal in the freeze. At the eutectic point, both metal and carbon continues to melt in the same time, yielding the melting plateau with a very small temperature range. When the melt is completed, the system will leave the eutectic point and move along the liquidus curve until reaching the point at the starting fraction.

It is worth noting that the M-C mixture with a carbon concentration of slight below the eutectic composition can also yield the eutectic point by taking some part of carbon from the crucible, but it may generate the risk to break the cell crucible.

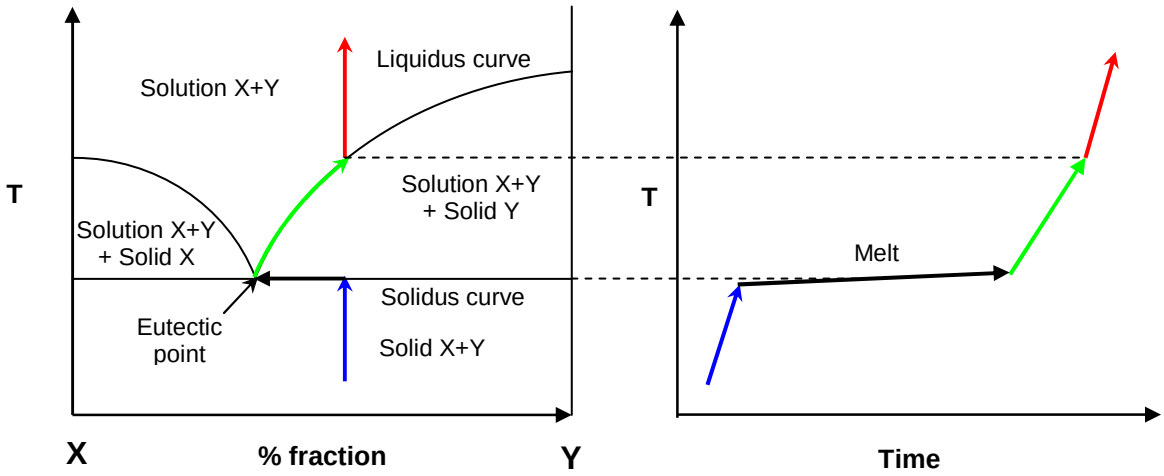

Figure 2.7 Typical schematic phase diagram and the melting curve of a M-C eutectic point.

A variety of metal-carbon alloys has been studied so far as possible fixed-point materials for high-temperature blackbodies. Their approximate temperatures are shown in Table 2.2. In practice, the inflection point of the melting curve is used as the reference point because of its higher reproducible and independence on the thermal history of the blackbody compared to the freezing curve.

Table 2.2 Metal-carbon eutectic alloys and their approximate transition temperature

Eutectic alloy	Approximate temperature, K
Fe-C	1426
Co-C	1597
Ni-C	1602
Pd-C	1765
Rh-C	1930
Pt-C	2011
Ru-C	2227
Ir-C	2564
Re-C	2747

A fundamental requirement for M–C fixed-points to be used as reference sources in radiation thermometry is the high reproducibility of the transition temperature. Extensive experiments reveal that only Co-C, Pt-C and Re-C blackbodies have the reproducibility and repeatability of better than 100 mK [5]. However, other materials can at least be used as secondary fixed-points to calibrate radiation thermometers and thermocouples. There are commonly two basic designs for M-C fixed-point cells: a small cell design for application in radiance mode and a large cell design for applications in irradiance mode. Both designs are shown in **Fig.** 2.8.

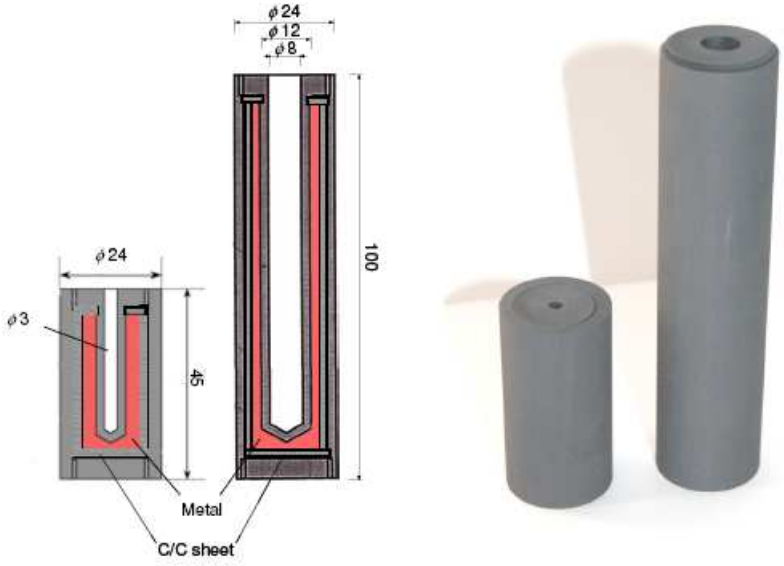

Figure 2.8 Basic designs for radiance and irradiance eutectic fixed-point cells [34].

In near future, the high temperature fixed-point blackbodies with small opening will possibly play an important role in radiation thermometry. Also in radiometry and photometry, it is possible that these high-temp fixed-points with the large opening design could replace FEL lamps in case they have a high reproducibility with accurately known thermodynamic temperatures [35].

2.4 Detector-based absolute radiometry

Radiometry is one of the fundamental areas of metrology, relating to the measurements of radiation as physical quantity. The most important application of radiometry in the optical range is photometry by taking into account the effect on human eyes using $V(\lambda)$. This means that radiometry has a fundamental importance in the lighting industry. Presently absolute radiometry plays an important role both in high accuracy temperature measurements and solar radiation observations for studying the climate change. This chapter provides basic quantities and basic concepts used in radiometric measurements.

2.4.1 Radiometry terms and concepts

Radiant flux, Φ, is the total radiant power or the total energy Q per unit time radiated by a source in all directions, expressed as

$$\phi = \frac{dQ}{dt}. \tag{2.19}$$

The unit of radiant flux is W (J s^{-1}).

Irradiance, E, is the flux incident on a surface A_2, defined by the radiant flux per unit area

$$E = \frac{d\phi}{dA_2}, \tag{2.20}$$

with unit W m^{-2}.

Radiance, L is the radiant flux emitted from a surface of source A_1 in a given direction through a particular solid angle Ω_1, defined as the radiant flux per unit solid angle per unit area in a specified direction deviated from the perpendicular to the surface.

$$L = \frac{d^2\phi}{d\Omega_1 dA_1 \cos\theta_1}. \tag{2.21}$$

Radiance has the unit W m^{-2} sr^{-1}.

Table 2.3 Summary of the definition and unit of radiometric quantity.

Symbol	Quantity	Definition	Unit
Φ	Radiant flux	$\phi = \frac{dQ}{dt}$	W or (J s^{-1})
E	Irradiance	$E = \frac{d\phi}{dA_2}$	W m^{-2}
L	Radiance	$L = \frac{d^2\phi}{d\Omega_1 dA_1 \cos\theta_1}$	W m^{-2} sr^{-1}

In order to measure these radiometric quantities, optical detectors are required to obtain the output quantity from the detector for a given input quantity. Therefore an important quantity in radiometry is the ratio between the input quantity and the output quantity which depends on the wavelength of the incident radiation, the so-called spectral responsivity. Consequently any traceable detectors are calibrated in terms of their spectral responsivity.

2.4.2 Calibration chain in Radiometry

Since the spectral responsivity of most of the high accuracy optical detectors are commonly traceable to the primary detectors, this primary method is so called detector-based absolute radiometry. Currently, the highest accuracy primary detectors are well known as cryogenic radiometers, which can measure the power of optical radiation by the electrical substitution method with an uncertainty of 0.01 % in the visible spectral region. In practical use, an accuracy of the primary detector is transferred to the instrument via transfer detectors in terms of absolute spectral power responsivity $s(\lambda)$ as shown in **Fig**. 2.9 [36].

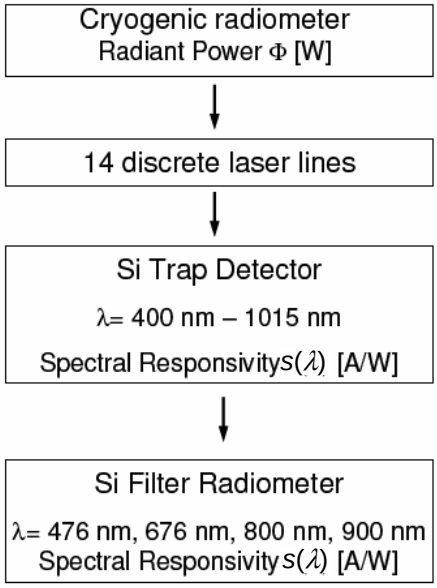

Figure 2.9 Calibration scheme in detector-based radiometry

2.4.3 Primary cryogenic radiometer, PCR

In order to measure the incident radiant power with highest accuracy, the electrical substitution method has to be applied for the primary radiometer. In brief, a cavity is heated by an electrical heater and controlled at a constant temperature. When the incident radiation hits the temperature-controlled cavity, the heating power will be lower due to the absorbed radiant power. Therefore, the absorbed radiation power can be directly

determined via the change of the electrical heating power. In order to obtain the optimum condition for highest accuracy, the copper cavity is cooled down to temperatures below 6 K by using liquid helium. As a result, this type of primary detector is so called primary cryogenic radiometer (PCR). Furthermore, the cavity is operated in vacuum to reduce the influences from the ambient air (convection losses and absorption). The principle of the measurements applied in the cryogenic radiometer is shown in **Fig**. 2.10. Due to its highest accuracy and high grade of independency on wavelength this type of radiometer is worldwide used as primary detector in many NMIs.

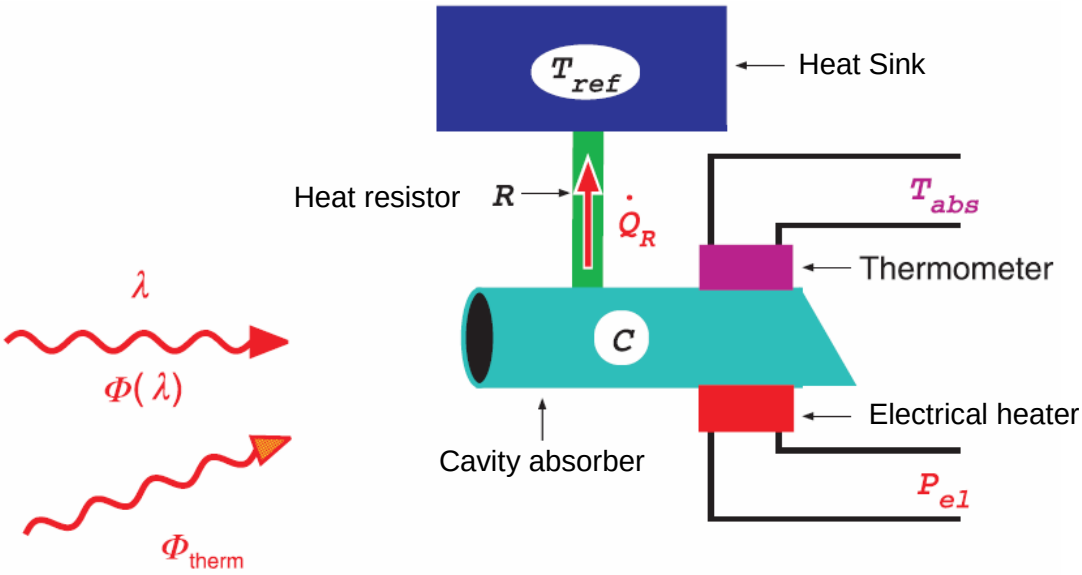

Figure 2.10 Schematic diagram of the Cryogenic primary radiometer [37]

The measurement of the spectral radiant power $\phi(\lambda)$ of the incident monochromatic radiation can be described by the following equation

$$\dot{Q}_{\mathrm{R}} = \varepsilon(\phi(\lambda) + \phi_{\mathrm{back}}) + P_{\mathrm{elec}} \ , \tag{2.22}$$

where $\dot{Q}_{\mathrm{R}}$ is the heat exchange between the cavity and heat reservoir which is kept constant

ε is the effective emissivity of the blackbody cavity

ϕ_{back} is the background radiation due to thermal radiation coming to the cavity.

P_{elec} is the change of electrical power.

2.4.4 Transfer standard detector

In order to disseminate the accurate radiant power measurement at the PCR in the common radiometry and thermometry laboratory, a transfer detector is required since the PCR can measure only the radiant power of the incident radiation and requires a clean room environment. The transfer standard can yield certain photocurrents at various spectral radiant powers and the ratio between the measured photocurrent and the obtained spectral radiant power is the so-called spectral responsivity. Presently, Si photodiodes are used in the wavelength range from 400 nm– 1100 nm, while InGaAs photodiodes are applied from 1100 nm to 2100 nm. In the UV region, Si photodiodes are also used but they are not considered to be stable enough due to the UV exposure [38].

For highest accuracy, so-called trap detectors consisting of 3 or more windowless single Si photodiodes in a trap configuration are used. This configuration eliminates the specular radiation losses from the single silicon photodiode detector and also to increases its spatial uniformity with respect to the responsivity [39]. A schematic arrangement of silicon photodiodes for a trap detector is shown in **Fig**.2.6. Since the incident radiation is reflected by the photodiode surfaces five times, an effective reflectivity of the trap detector is a multiple of five reflectance coefficients. Therefore the reflectivity of the trap detector is close to zero.

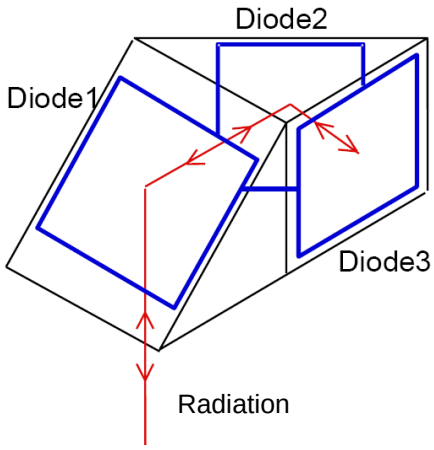

Figure 2.10 Optical arrangement of a 3 Si photodiodes trap detector [40].

In order to measure the spectral responsivity of the trap detector at the PCR, a variety of lasers were used and the spectral responsivity at the discrete laser lines can be experimentally obtained by [41, 42]

$$s(\lambda) = \frac{I_{\mathrm{ph,det}}}{P_{\mathrm{PCR}}}. \qquad (2.23)$$

Since the trap detector is based on a semiconductor material, its spectral responsivity depends on the detected radiation wavelength. Based on a physical model for Si photodiodes, the spectral responsivity can be exactly determined in the VIS and near IR by

interpolation between the laser wavelengths from values obtained experimentally at discrete laser wavelengths using [41].

$$s(\lambda) = [1 - \rho(\lambda)] n_{\text{air}} \eta_{\text{i}}(\lambda) \frac{e\lambda}{hc}, \tag{2.24}$$

where n_{air} is the refractive index in air at wavelength λ
$\eta_{\text{i}}(\lambda)$ is the internal quantum efficiency of the detector
e is the electron charge
$\rho(\lambda)$ is the reflectance of the detector for wavelength λ.

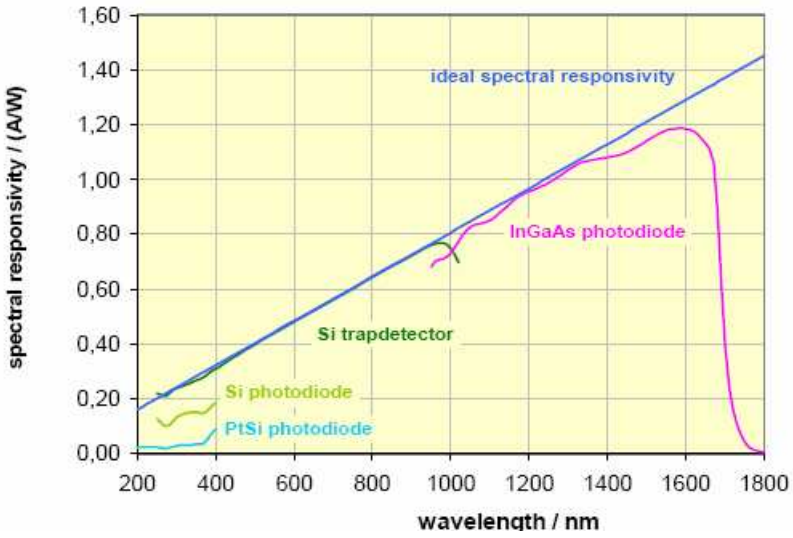

Figure 2.11 Typical spectral responsivity of a single Si photodiode, a Si trap detector and an InGaAs photodiode

2.4.5 Spectral radiometer

In many applications of optical radiation measurement, the optical radiation in a wavelength band is required, which can be achieved using spectral radiometers. An example of a spectral radiometer is a photometer, which responses to the radiation only in the visible region matching the $V(\lambda)$ function of the human eye. Presently, spectral radiometers are widely used in the application of thermodynamic temperature measurement due to higher accuracy than broadband radiometers. In principle, the spectral radiometers consist of two main components: a detector and a spectrally selective filter. With this combination, the emitted spectral radiant power from a thermal source can be measured. According to Planck's law, measuring spectral radiance requires an optical component, such as apertures and lenses, to define the geometry factor.

Generally measuring the spectral radiance can be achieved by means of two methods: the radiance method and the irradiance method.

1) **Radiance method** Using a number of lenses, the spectral radiance of any radiation source can be directly measured. By focusing an image of the source onto a precision aperture at a certain position in front of an interference filter, the spectral radiance can be directly measured using the following equation

$$L_\lambda = \frac{\phi_\lambda}{A_2 \cdot \pi \sin^2 \theta} = \frac{E_\lambda}{\pi \sin^2 \theta}, \tag{2.25}$$

where θ is the half angle of the field of view behind the lens. An example of the spectral radiometer based on this method in the application of temperature measurement is a radiation thermometer.

An advantage of this method is the ability to measure high signals even with small sources, because the large throughput due to the imaging optics. Since the measured spot can be smaller than 1 mm, radiation thermometers can be used to measure the radiance temperature of small blackbody sources. However, the measurement error may be dependent on the diameter of the radiation source in comparison to the diameter of the source the radiation thermometer has been calibrated with. This effect is the so-called size of source effect, however the effect is less than 10^{-3} for high accuracy radiation thermometers.

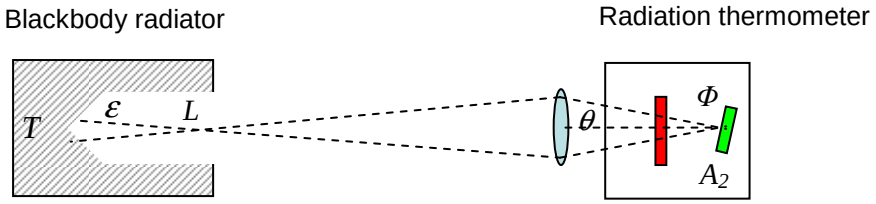

Figure 2.12 Schematic diagram of radiance measurements by means of a lens-based imaging radiometer**.**

As can be seen in **Fig.** 2.12, the radiance method yields the radiance radiating from a single point over a small area within a solid angle.

2) **Irradiance method** Spectral radiance can be determined via spectral irradiance measurement at an aperture in front of the spectral radiometer. With the geometry of the measurement, the spectral radiance can be calculated approximately by Equation 2.26. Spectral radiometers based on this principle are so called filter radiometers, FRs.

$$L_\lambda \approx \phi_\lambda \cdot \frac{d^2}{A_1 A_2} = E_\lambda \cdot \frac{d^2}{A_1}, \tag{2.26}$$

where A_1 and A_2 are the aperture areas in front of the radiation source and the detector, and d is the distance between the two apertures.

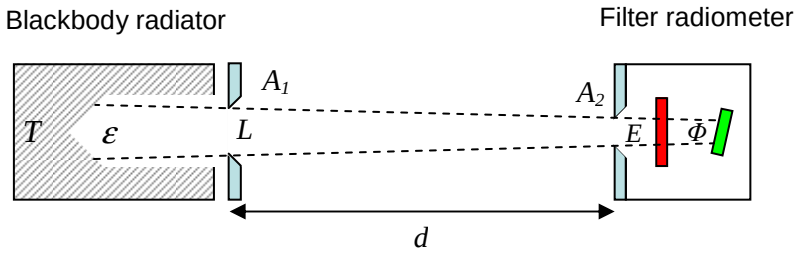

Figure 2.13 Schematic diagram of radiance measurements by means of two apertures.

As can be seen in **Fig.** 2.13, the irradiance method yields the mean radiance across the source aperture from a large field of view through the bottom of the cavity.

More accurate details on calculation of the measurement geometric factor can be described in the following. The radiant flux $d\Phi_{1\to2,\lambda}$ from one area element dA_1 of the aperture A_1 to an area element dA_2 of the aperture A_2 is

$$d\phi_{1\to2,\lambda} = L_\lambda \cdot \frac{dA_1 \cos\upsilon_1 \cdot dA_2 \cos\upsilon_2}{d'^2}, \tag{2.27}$$

where d' is the distance between the two area elements and υ_1, υ_2 are the angles between the normal vectors of the area elements. The total radiation transport between source and detector can then be expressed as

$$\phi_{1\to2,\lambda} = L_\lambda \cdot \int_{A_1} \int_{A_2} \frac{dA_1 \cos\upsilon_1 \cdot dA_2 \cos\upsilon_2}{d'^2}. \tag{2.28}$$

For the experimental set-up used here an analytical solution is given by

$$\phi_{1\to 2,\lambda} = L_\lambda \frac{2\pi r_1^2 \cdot \pi r_2^2}{r_1^2 + r_2^2 + d^2 + \sqrt{(r_1^2 + r_2^2 + d^2)^2 - 4r_1^2 r_2^2}}. \tag{2.29}$$

From (2.29) follows for the spectral irradiance at the detector aperture by the equation 2.20 as

$$E_\lambda = L_\lambda \frac{2\pi r_1^2}{r_1^2 + r_2^2 + d^2 + \sqrt{(r_1^2 + r_2^2 + d^2)^2 - 4r_1^2 r_2^2}} = L \cdot G, \tag{2.30}$$

where G is the geometric factor of the measurement using the two apertures.

A sophisticated application requiring absolute radiometry with ultimate low uncertainties is to measure the thermodynamic temperature of a blackbody. In principle, at any source of thermal radiation, the absolutely calibrated radiometers can be used to measure directly an absolute value of radiance over a narrow or broad spectral band of wavelengths and convert the signal to temperature by Planck's radiation law or Stefan-Boltzmann's law. The temperature determined by means of absolute radiometry is a so-called thermodynamic temperature, because it is directly determined from an equation of state without referring to the defined temperature of the ITS- 90.

In case of the spectral band radiometer based on photodiodes, the photocurrent I_{ph} varies with temperature and spectral responsivity $s(\lambda)$ by

$$I_{\mathrm{ph}}(T) = \varepsilon_{\mathrm{BB}}\, G \int s(\lambda) \cdot L(\lambda, T_{\mathrm{BB}})\, d\lambda, \tag{2.31}$$

where $\varepsilon_{\mathrm{BB}}$ is the emissivity of the blackbody
G is the geometric factor of the measurement set-up
$s(\lambda)$ is the spectral responsivity of the spectral radiometer.

At PTB, the FRs have been used to determinate thermodynamic temperatures of a thermal blackbody source in the temperature range from 420 °C to 3000 °C [43, 44] . However, this method requires a large aperture radiation source to avoid large diffraction errors.

3 Objectives

According to the definition in the International Temperature Scale ITS-90, the temperature scale above 961.78 °C has two fundamental limitations, namely large uncertainties at high temperatures due to the extrapolation of the scale and non-unique of the scale due to the choice of the freezing temperature of silver, gold or copper [45]. To improve the temperature scale at high temperatures, absolute spectral radiometry can be used as a solution by a direct realization of the thermodynamic temperature via Planck's law of thermal radiation.

At PTB, filter radiometers (FRs) are used to measure thermodynamic temperatures of a blackbody in irradiance mode [4], which requires a thermal source with a large opening to achieve a temperature uncertainty comparable to the ITS-90. Therefore, a more practical realization of thermodynamic temperature requires imaging filter radiometers, such as radiation thermometers. Presently, many national metrology institutes have attempted to realize a thermodynamic temperature scale by using a radiation thermometer [46, 47, 48, 49 and 50]. For that purpose, such a radiation thermometer is calibrated in terms of absolute spectral radiance responsivity at a tuneable laser-based facility using an integrating sphere as a lambertian source. However, due to the interference fringes in spectral radiance responsivity, this method is extremely time consuming for a complete measurement over the whole bandpass of the interference filter within the radiation thermometer. Moreover a number of tuneable lasers with different wavelength range are also required to cover the desired wavelength range for such measurements.

Therefore, a source producing a monochromatic radiation with an optimal bandwidth is required for the absolute calibration of radiation thermometers. At the beginning of this work, a conventional halogen lamp based monochromator facility was applied for illuminating an integrating sphere to provide monochromatic-lambertian radiation in the spectral range between 400 nm to 1100 nm [51]. One advantage of this attempt is that an optimal spectral bandwidth can be selected in order to avoid any interference fringes in spectral radiance responsivity. However, the output power obtained from the monochromator using such lamp is not sufficient for the absolute calibration of radiation thermometers.

For this reason, a monochromator-based set-up will be newly developed to calibrate radiation thermometers in terms of absolute spectral radiance responsivity for realizing the thermodynamic temperature above 1377.33 K, independent from the ITS-90. Since an integrating sphere will be used as a lambertian source, a high spectral output power from the monochromator is required to achieve enough spectral radiance for the set-up. Therefore, various types of broadband radiation sources will be tested and optimized at the new set-up to provide an optimal calibration light source. For the absolute calibration, a Si trap detector, traceable to the primary cryogenic radiometer of PTB, will be used as the transfer detector. The integrating sphere and the trap detector must be fully characterized to

ensure reliable and validated calibration results. The expected calibration uncertainty should be at the same level or better than the uncertainty obtained at the laser-based facility.

In this work, a radiation thermometer of type LP3 is selected to be calibrated at this new set-up. For the LP3-type radiation thermometer, the targeted calibration uncertainty is expected to be less than the calibration uncertainty based on ITS-90 i.e. 0.12 % with the coverage factor k=1, equivalent to about 400 mK at 2800 K using a 650 nm interference filter. In order to check the accuracy of the absolute calibration at the developed set-up, the LP3 will also be absolutely calibrated at a tuneable laser facility (TULIP) of PTB.

In the next step, the thermodynamic temperatures of the gold and copper freezing point blackbodies of PTB will be measured for verifying the accuracy of the absolute radiometric thermometry in comparison to the assigned values in the ITS-90. Resulting estimated values for T-T_{90} are important secondary objectives of this work.

Finally, the absolutely calibrated radiation thermometer will be applied to measure the thermodynamic melting temperatures of a set of selected small aperture high-temperature fixed-point blackbodies, namely Co-C, Pt-C and Re-C. The results will be compared with results obtained by means of indirect measurements using filter radiometers for confirming an agreement between the already established approach of PTB and the newly developed approach in this work.

4 Development of the monochromator-based absolute calibration set-up

4.1 Introduction

Most national metrology laboratories have recently used tuneable lasers or fixed-wavelength lasers as radiation sources for spectral responsivity calibrations of detectors, because these lasers supply high output power and accurate and stable wavelengths [46, 48, 50, 52, 53]. For calibration in radiance mode, the laser output is coupled into an integrating sphere to generate a uniform lambertian radiance at a desired radiance level. To cover a wide wavelength range from the near UV to the near IR, the laser-based method requires a series of tuneable lasers to measure the absolute radiance responsivity directly or a laser providing single wavelengths around the center wavelength of the spectral bandwidth of the radiation thermometer in combination with a relative calibration from the conventional monochromator based method using halogen lamps [50]. However, due to the high coherence, multiple reflections of the laser radiation in the optical system of radiation thermometers occur, resulting in interference fringes, especially around the wavelength of the bandpass of the radiation thermometers [54, 55]. In this case, complete measurements with small wavelength steps well below the period of the interference fringes are necessary to follow the interference pattern continuously to achieve high accuracy results. However, measurements over the whole bandpass with such small wavelength steps are extremely time consuming and not practical in every case, thus, a resulting incomplete averaging may introduce significantly large uncertainties due to the interference effect. In addition, a measurement with single wavelength lasers in combination with a relative calibration probably may give a significant error due to an unknown amplitude of the interference effect at the laser wavelength [50].

Therefore, a monochromator-integrating sphere-based facility has been developed at PTB within this work, because the spectral bandwidth of the monochromator can be adjusted to avoid any interference fringes in the spectral radiance responsivity. In this case, spectrally broadband light sources have to be applied for the monochromator. However the spectral power dynamic range of a traditional quartz tungsten halogen lamp (< 1 μW/nm) is lower than that of a laser (mW/nm up toW/nm) by more than 3 orders of magnitude, which limits the standard uncertainty of the measurements [51]. Since the calibration uncertainty due to noise decreases with increasing radiant power, the standard uncertainty of the calibration at the monochromator-based facility can be in principle reduced by increasing the input radiant power of the monochromator. For this reason, a variety of broadband light sources have been evaluated during this work to find the optimum source for this set-up.

The ultimate goal of this study is to develop a monochromator based facility for absolute radiance calibration of radiation thermometers with the measurement uncertainty comparable to that of the laser-based facilities and that for the irradiance calibration of

usual non-imaging filter radiometers. Descriptions of the developed set-up are presented in the following sections and all parameters affecting the uncertainty are described.

4.2 Monochromator-based absolute radiance calibration set-up

For the purpose of temperature scale realization, many national metrology laboratories have used a monochromator system based on lamp sources to measure the relative spectral responsivity of their radiation thermometers. However, in this case, one of the standard reference fixed-point blackbodies is still required to realize the temperature scale in such as scheme as

$$S(T) = a\int L_{\lambda,s}(\lambda,T)\cdot R(\lambda)d\lambda\,, \tag{4.1}$$

when $S(T)$ being the signal from the radiation thermometer at a blackbody temperature T, a is the constant obtained from the measured signal at the fixed-point and $R(\lambda)$ is the measured relative spectral responsivity. This approach is a method to realize the current temperature scale in the ITS-90, because the absolute value a for the spectral responsivity results from the ITS-90 temperature of the used reference fixed-point.

In this work, I aimed at developing a monochromator system to measure the absolute spectral responsivity of any radiation thermometer for realizing the temperature scale without a standard fixed-point blackbody, i.e. independent from the ITS-90, enabling a thermodynamic temperature determination. Therefore, more care had to be taken at the new set-up to meet the requirements. The concepts of this set-up for absolute calibration of radiation thermometer are

1) to obtain spectral radiation with adjustable spectral bandwidth in the wavelength range from 400 nm to 1000 nm.

2) to produce a quasi and uniform lambertian source with highest possible radiating power for any radiance measurements.

3) the ability to calculate the geometric factor of the absolute radiance measurement using a standard detector in irradiance mode.

4) to perform an absolute calibration of a radiation thermometer by means of direct substitution method i.e. placing the reference detector in the place of the radiation thermometer under test.

A schematic diagram of the conceptual design for this monochromator-based facility is shown in **Fig**. 4.1. Basically, the system consists of a lamp source with a condensing lens unit, a single monochromator and an integrating sphere. In brief, the lamp radiation is imaged onto the entrance slit of the monochromator with matching *f* number using a pair of achromatic lenses. An appropriate filter is required to suppress higher orders of the spectral radiation. Although the stray light is slightly larger than 10^{-5} when using a single

monochromator, it can be neglected for measurements with an uncertainty of larger than 10^{-3}, but is considered as a source of uncertainty.

In contrast to measurements in irradiance mode [4], which require a collimated beam, the radiation behind the exit slit is focused onto the entrance port of an integrating sphere using a mirror system to produce a lambertian radiation source at another port of the sphere. Since many reflections occur inside the sphere, the output light is unpolarized. A precision aperture is used at the sphere opening to accurately define the radiating opening for the absolute measurement. A monitor diode is also installed to correct for short term variations of the lamp source output during the measurements. A reference detector is placed on two orthogonal axial precise translation stages in front of the radiation thermometer in a light tight box. One direction is used in the comparison process and the other one is used for setting the distance between the sphere and the reference trap detector. An interferometer is used to determine the distance between the trap detector aperture and integrating sphere aperture accurately. To minimize the effect of diffuse radiation, a baffle is installed between the sphere and the detectors during any measurements.

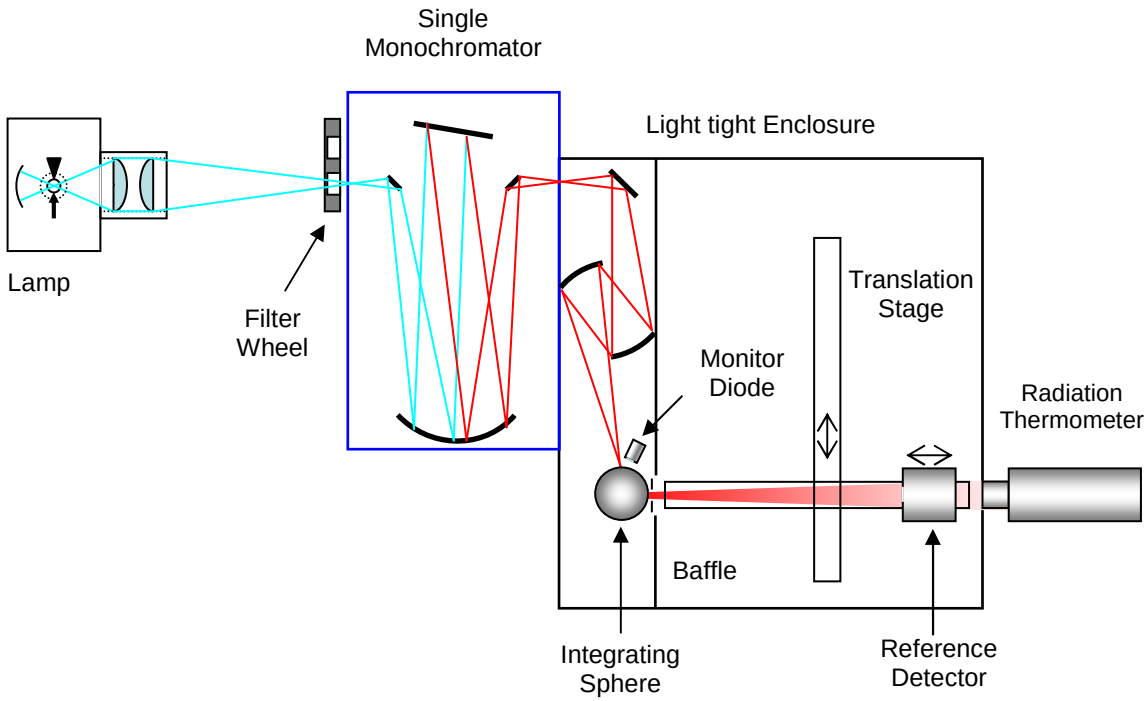

Figure 4.1 Schematic diagram of the monochromator-based calibration facility

Based upon long term experiences of PTB, a Zeiss mirror monochromator model SPM2 was selected due to its high performance and its great operating convenience [56]. Using the excellent imaging qualities of an off-axis parabolic mirror, the resulting image on the slit is free from chroma and astigmatism. Using this monochromator, several gratings can

be interchanged to select the desired wavelength. Therefore, high precision diffraction gratings with groove density of 650 lines/mm, 1302 lines/mm and 2400 lines/mm were tested at the monochromator with respect to the maximum output power at the desired wavelength. In principle, the diffraction grating with the maximum groove density should transmit the maximum spectral output due to the lowest reciprocal dispersion (1 nm/mm). Unfortunately, the blazed wavelength of the 2400 l/mm grating does not match the desired wavelength in the VIS region due to its original purpose for application in the UV region. For this reason, the selection of spectral radiation is performed by using the precision diffraction grating with 1302 lines/mm (reciprocal dispersion of about 2 nm/mm) and the blaze wavelength of 575 nm nearest to the centre of the desired wavelength range, and driven by a stepping motor. For this grating, one step of the stepping motor changes the output wavelength by 13 pm. The wavelength calibration is performed at 50 spectral lines of different spectral lamps in the wavelength range from 370 nm to 720 nm. The calibration result is fitted by a ninth order polynomial equation to be used as a calibration curve for wavelength selection with a standard uncertainty of 26 pm in the visible region. The reproducibility of the wavelength is better than 13 pm, due to excellent temperature stability of the monochromator and careful wavelength initialization with a mercury lamp at 546.075 nm prior to every measurement.

4.3 Evaluation of radiation sources

Since the purpose of the new set-up is to apply an integrating sphere for producing lambertian radiation, the output power from the monochromator should be as high as possible, especially for a calibration over the whole wavelength range. For this reason various types of commercially available broadband light sources were investigated at this set-up by coupling the radiation of these lamps into the entrance port and measuring their output power at the exit port of the monochromator as well as their output stability. However, the coupling for each lamp is quite different depending on their radiating areas and field of views.

In principle, the input power is limited by 2 factors; the slit width and the *f* number of the monochromator. The slit width can be adjusted to obtain the required spectral bandwidth depending on the spectral dispersion of the grating used in the monochromator. In case of the output power, if the width of the input and output slit is doubled then the output power is increased quadratically. Thus, an important parameter to select a radiation source is the spectral radiance of the lamps and their stability.

1) Halogen lamp At the beginning, a 400 W halogen lamp model HLX 64665 from OSRAM was tested at the set-up. The dimension of the lamp filament is approximately 10 mm in height and 5 mm in width. For such an extended light source, an image at the entrance slit of the monochromator must be coupled with the magnification of 1:1 to achieve the best efficiency. As the *f* number of the monochromator should be larger than 9, a spherical mirror with f = 60 mm and a plane mirror were used as given in **Fig.** 4.2. To obtain the optimal position of the lamp, the output radiation at the exit slit was monitored by a Si photodiode.

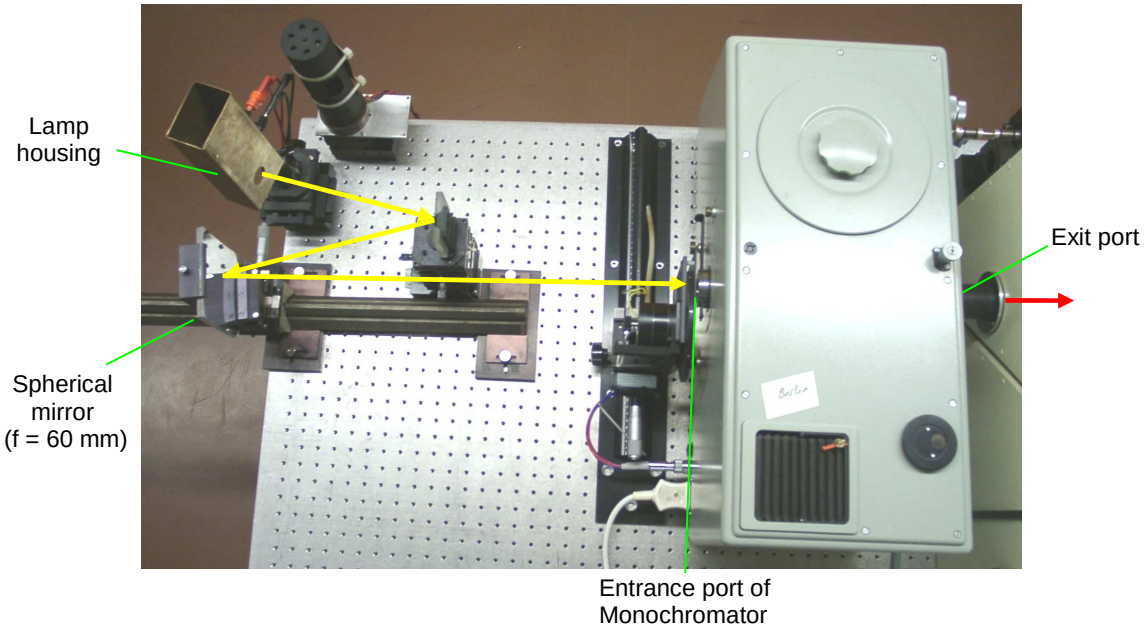

Figure 4.2 Photograph of the coupling of the halogen lamp using a mirror system. The lamp placed inside the lamp housing was driven by a power supply with the current of 10.6 A.

After the lamp coupling onto the entrance slit, the monochromator output radiation was focused onto a high accuracy photodiode to measure the spectral output power and also the stability of the lamp. The maximum spectral output power obtained from the halogen lamp at this set-up is 0.3 µW/nm around the wavelength of 600 nm as shown in **Fig**. 4.3.

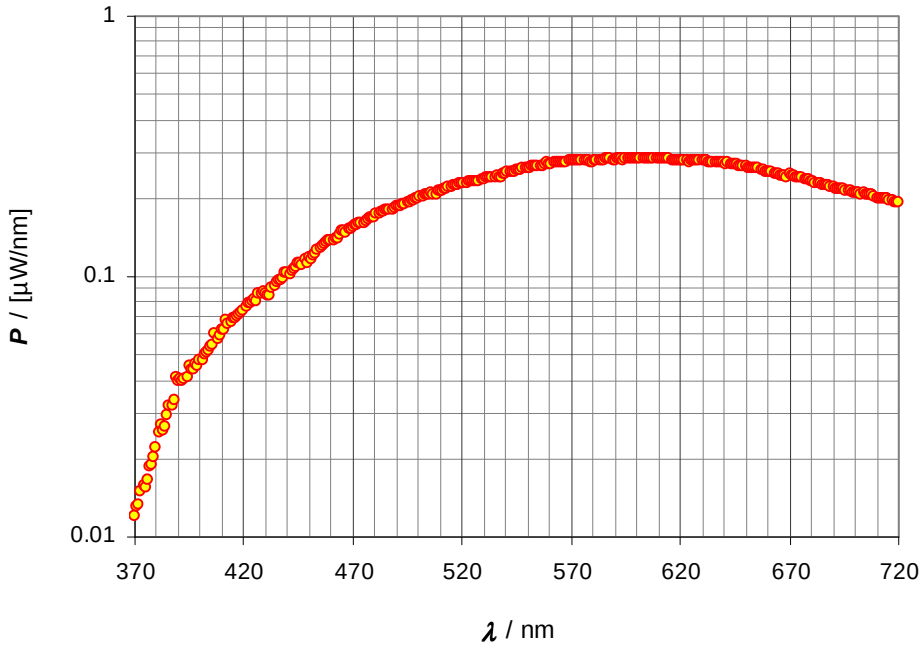

Figure 4.3 Output spectral power from the monochromator obtained by the halogen lamp with an entrance and exit slit width of 0.5 mm

The standard deviation of the output radiation over 30 minutes without cooling is better than 0.02 % as shown in **Fig.** 4.4.

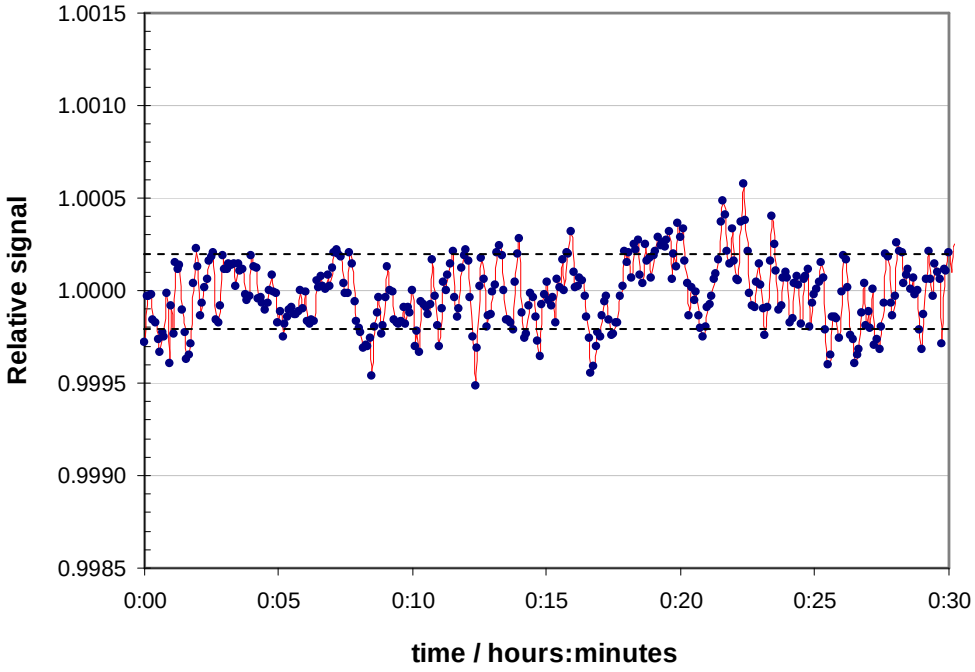

Figure 4.4 Stability of the output power from the halogen lamp at this set-up with the standard deviation of less than 0.02 %.

2) Xenon lamp and Xe-Hg lamp As the output power from the monochromator depends on the setting of the slit widths of the monochromator, such a discharge plasma lamp would yield more output power than the halogen lamp due to its small radiating area. As a result, a 75 W xenon lamp model XBO from OSRAM was tested at this set-up due to its small arc size (0.25 mm × 0.5 mm) and high radiance level compared to other xenon lamp models. Since the entrance slit width is set to 0.5 mm for the output radiation with the spectral bandwidth of 1 nm, the magnification of 2 should be optimal for this light source. However, due to the *f* number of the monochromator, the magnification of about 3 was obtained by using a lens system. The light radiating from the xenon lamp's housing with the *f* number of 3 was imaged at the entrance slit with the *f* number of 9 as illustrated in **Fig**. 4.5.

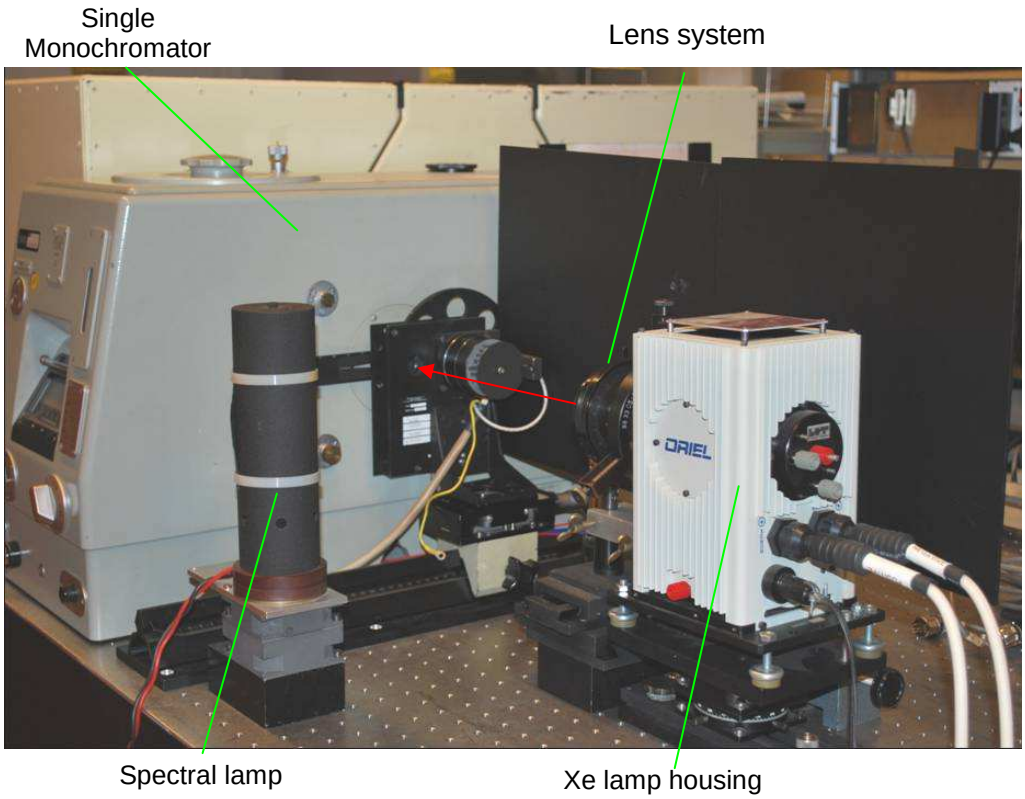

Figure 4.5 Photograph of the coupling of the xenon lamp with condensor unit.

In order to obtain the maximum output monitored by the photodiode, the lamp was moved to or away from the lens unit placed at the fixed position. Since the lamp housing provides a rear reflector to increase the total emitted radiation, the reflective radiation must be also focused at the entrance slit.

For a lamp driven current of 5.4 A, the spectral output power obtained at the exit slit was measured by the same Si-photodiode and found to be higher than 1 μW/nm in the wavelength range from 500 nm to 670 nm as shown in **Fig.** 4.6. The output power stability after 30 minutes is shown in **Fig.** 4.7 for an averaging time of 5 s.

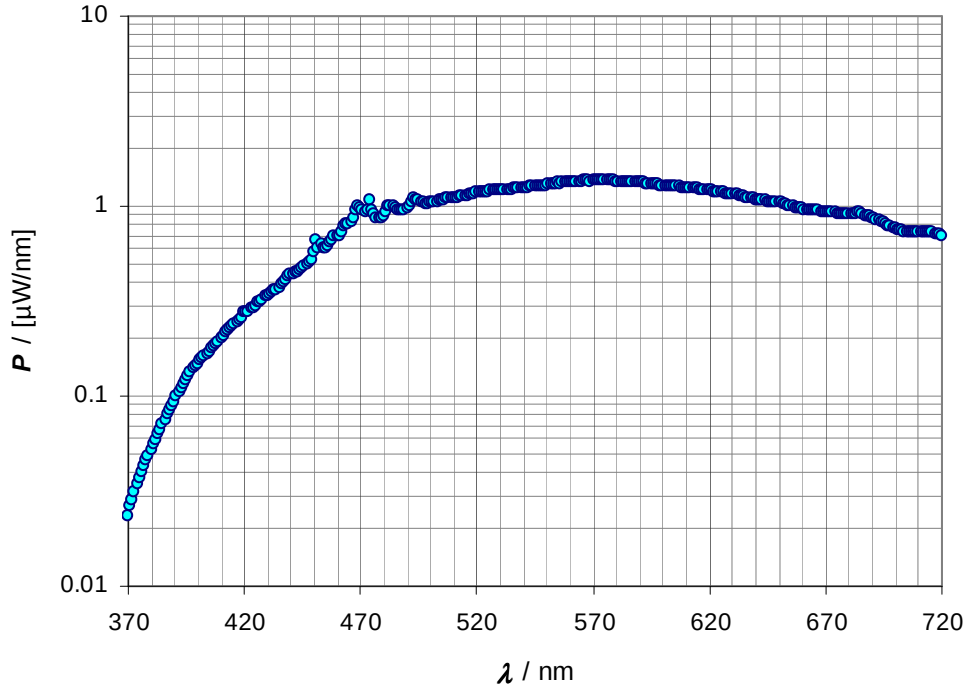

Figure 4.6 Output spectral power from the monochromator obtained by the xenon lamp

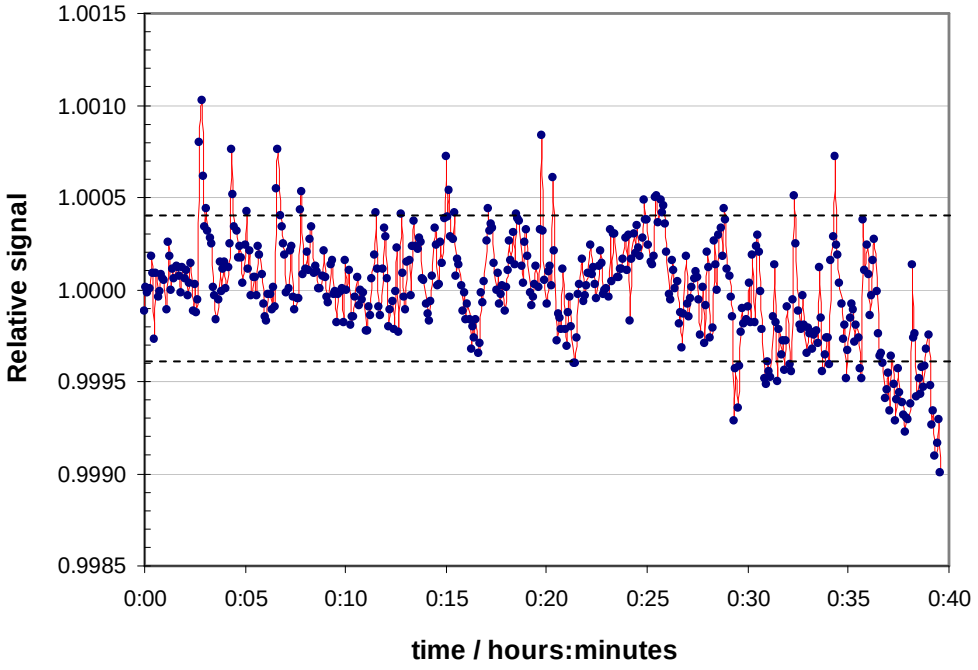

Figure 4.7 Stability of the output power for the xenon lamp,
standard deviation of less than 0.04 %.

As can be seen in **Fig.** 4.7, there are rapid fluctuations of the output radiation with the maximum amplitude of 0.1 %. This effect can be described by the positional stability of the arc, which rapidly changes. However, the long term stability of the xenon lamp is still acceptable mainly due to the convective cooling of the lamp housing.

Additionally, a high pressure Xe-Hg lamp was also investigated at this set-up. The resulting spectral output power was found to be higher than 1 μW/nm only around the peaks of the mercury lines as shown in **Fig.** 4.8, while its stability fluctuations were found to be larger than 0.1 % in 30 minutes because there was no cooling system.

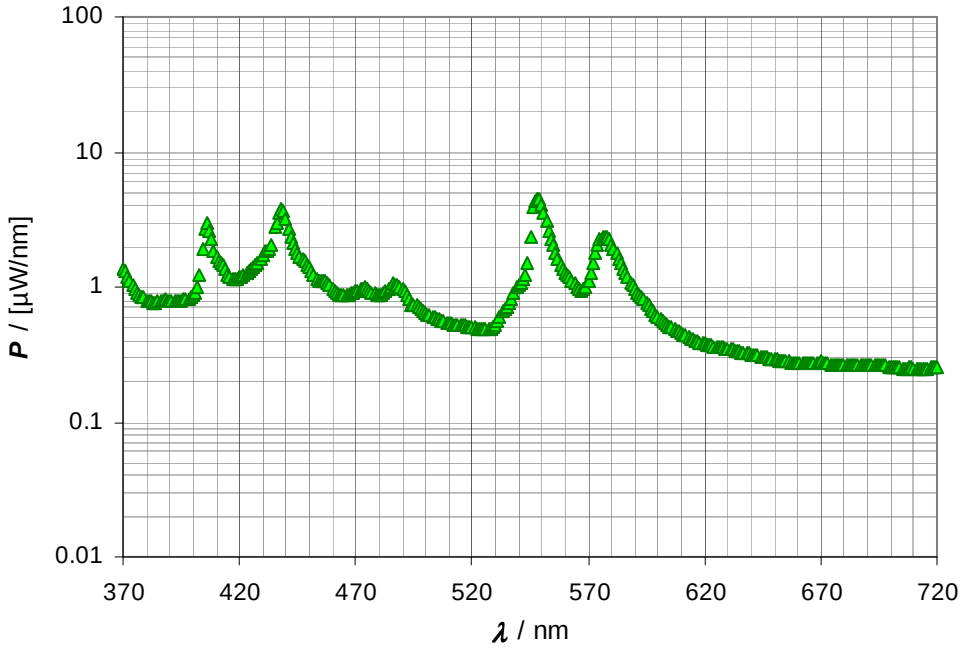

Figure 4.8 Output spectral power from the monochromator obtained by the Xe-Hg lamp

3) P-VIP lamp is a type of high pressure mercury light source, optimized for high luminance and manufactured by OSRAM. From the manufacturer data, this lamp type can yield a luminance above 200 kCd/cm^2, therefore it is reasonable to investigate this lamp at this set-up. In this work, a P-VIP model 230/1.0 E20.8 with an elliptical reflector was used. A photograph and the dimensions of this light source are given in **Fig**. 4.9.

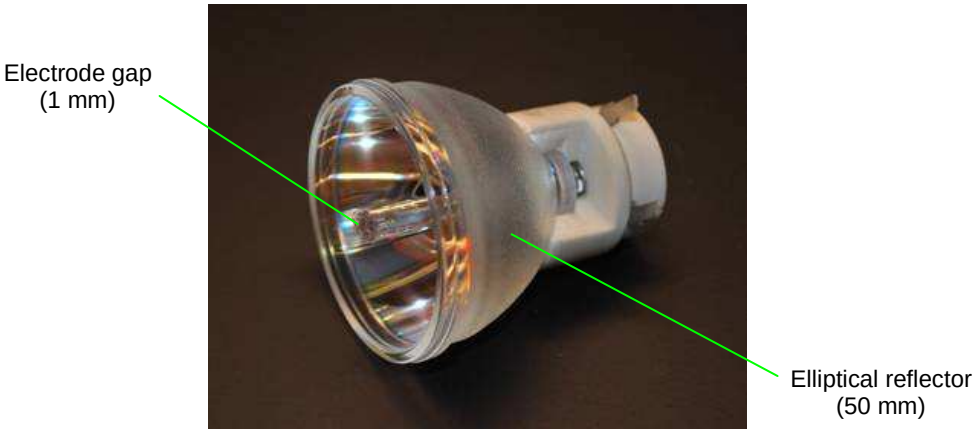

Figure 4.9 The photograph and the dimensions of the P-VIP light source.

In the same way as the Xe lamp and Xe-Hg lamp, a lens unit was used to collect the radiation at the focal point of the lamp (~30 mm). At this stage, the *f* number of 2 was found to be optimal for the P-VIP lamp with the same lens unit. Then the spectral output power was measured.

For the measurement of the spectral output power, it seems the second order of the lamp is extremely significant to the output power, although an appropriate glass filter was already used. Thus an additional bandpass filter with an active water cooling was applied to avoid the second order radiation for achieving the actual spectral power from the lamp. With the appropriate glass filters, the spectral output power was found to be higher than 1 μW/nm up to 10 μW/nm around the peaks of mercury lines as shown in **Fig.** 4.10.

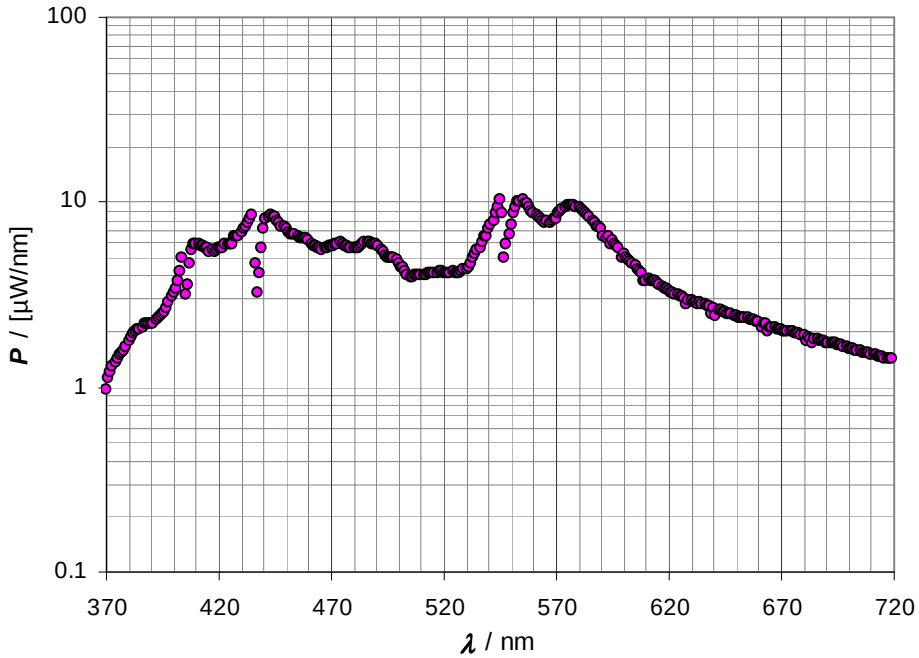

Figure 4.10 Output spectral power from the monochromator obtained by the P-VIP lamp

Although this light source yields maximum radiant power in the UV and VIS region, it also produces a maximum of thermal radiation. Therefore an active air cooling is required for this lamp to control the temperature of all lamp assemblies. However it is obviously that the stability fluctuations of the output power obtained from this lamp are larger than 1 % over a period of 30 minutes as can be seen in **Fig**. 4.11.

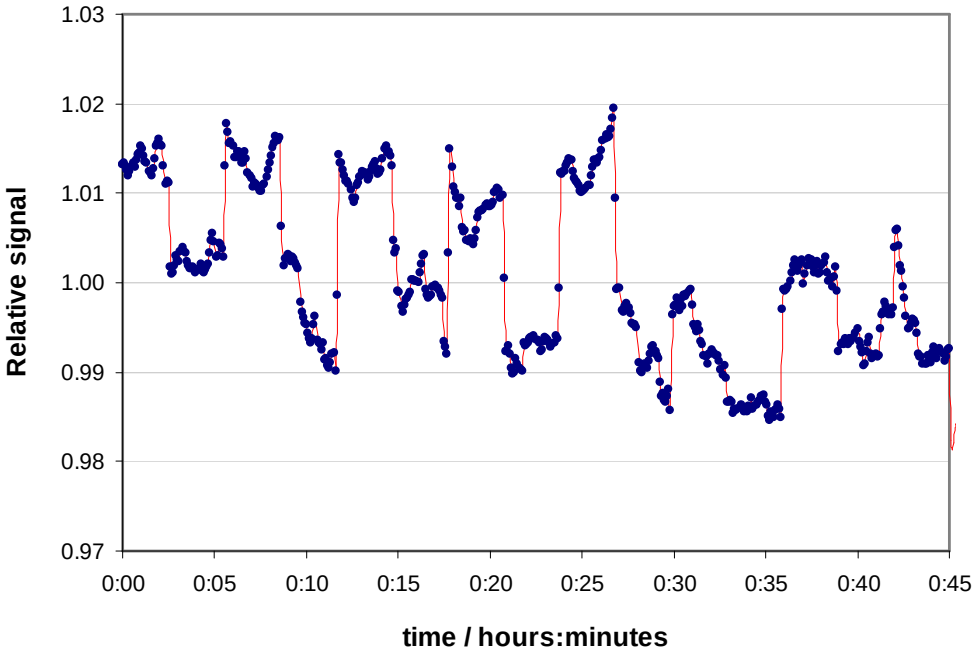

Figure 4.11 Output power stability from the P-VIP lamp controlled by an automatic polarity change function of the power supply.

For every 3 minutes, rapidly changes of signal were observed by the photodiode due to the automatic polarity change of the lamp electrodes, controlled by the lamp power supply. Although this function of the power supply can be switched off, the output power stability fluctuations for this lamp are still larger than 0.5 % in 3 minutes. More efficient thermal management of the light source is required if it will be further used.

4) Laser Driven Light Source, LDLS™ Finally an advanced discharge light source driven by laser, LDLS model EQ 1500 was tested for a short term period. This novel light source is developed to enable extreme high brightness over a broad spectral range from UV to near IR with relatively smooth spectrum. Not using electrodes within the lamp increases its lifetime, compared to traditional arc lamps [57]. With the arc size of about 0.2 mm, a magnification of 2.5 can be in principle used to illuminate the entrance slit of the monochromator, however the *f* number of the monochromator still limits the magnification of the image. For optimized coupling, the plasma arc of the light source was collected with the *f* number of 2 and imaged onto the entrance slit with the *f* number of 10 and the spot size of only 1 mm. A photograph of this lamp with the lens unit is shown in **Fig.** 4.12.

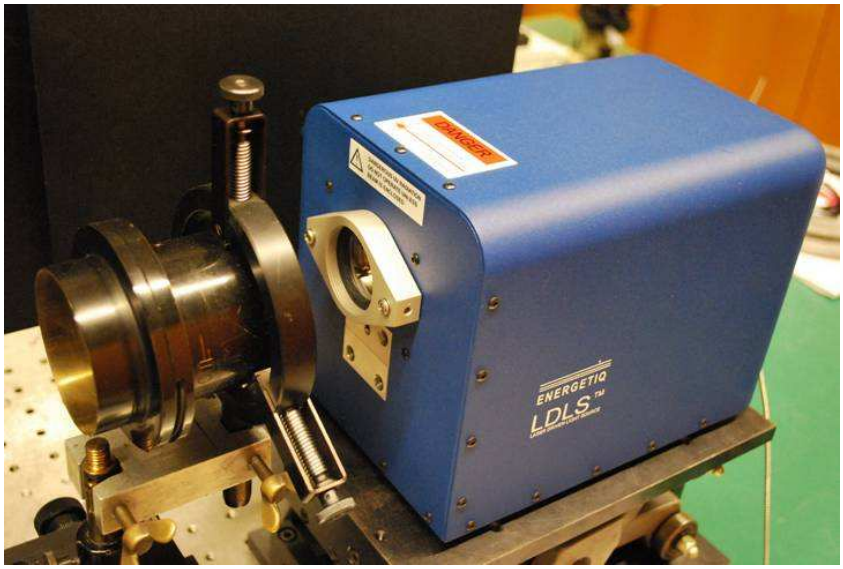

Figure 4.12 Photograph of the LDLS model EQ1500 with the lens unit.

The spectral output power obtained from this source and its output power stability after 30 minutes are illustrated in **Fig.** 4.13 and **Fig.** 4.14, respectively.

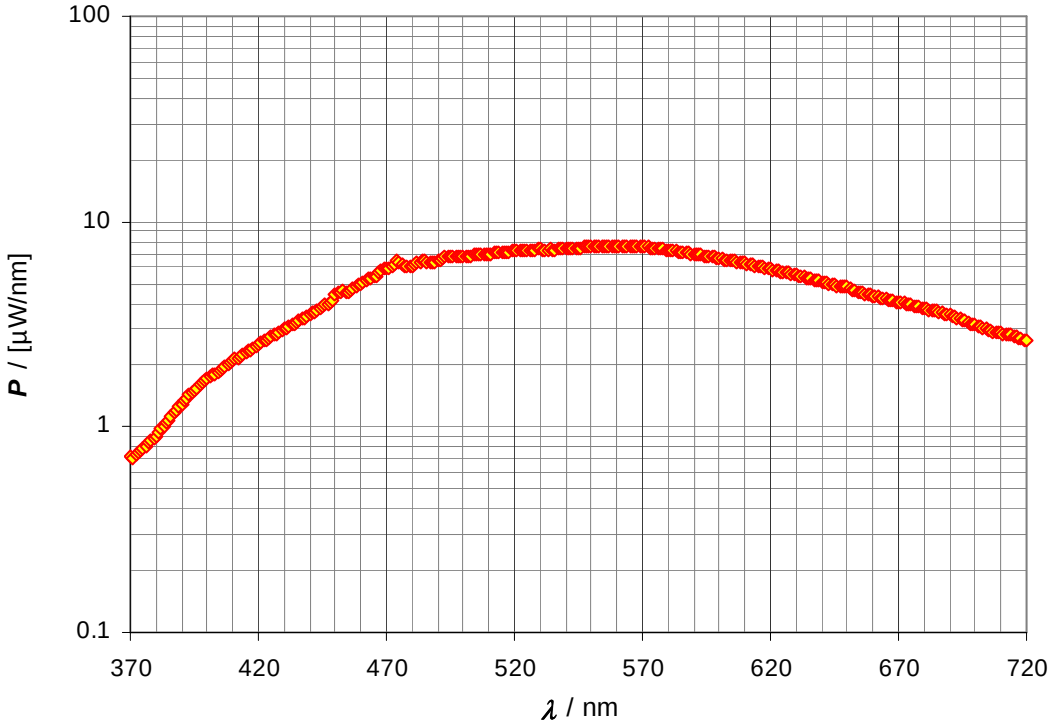

Figure 4.13 Output spectral power from the monochromator obtained by the LDLS model EQ 1500.

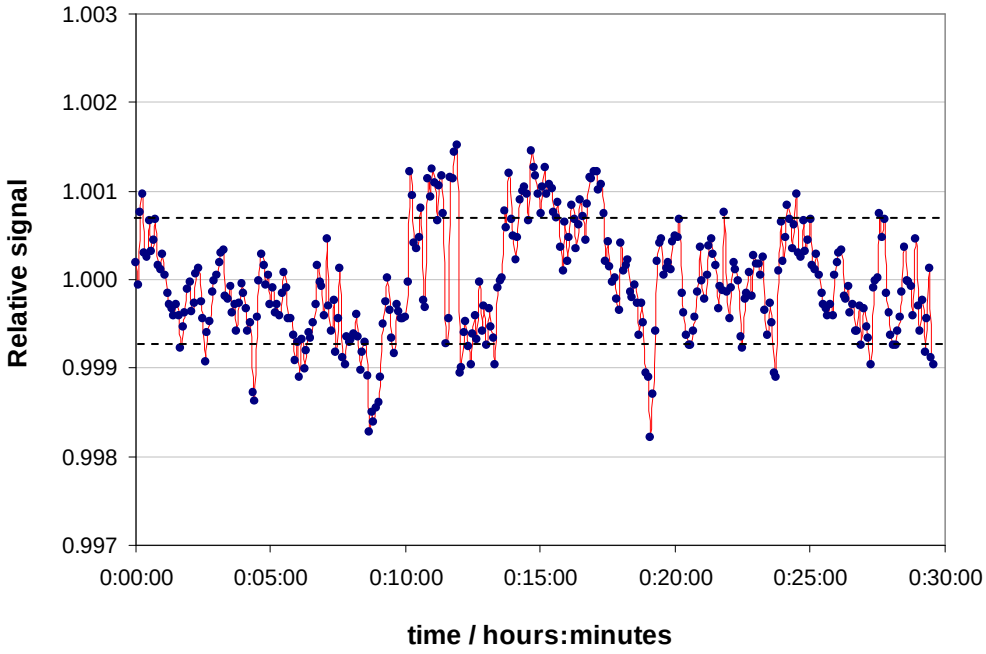

Figure 4.14 Stability of the output power from the LDLS model EQ1500 with the standard deviation of less than 0.07 %.

In the same way as other high brightness lamps, this LDLS requires an active water cooling to control its output power stability. Due to a short term test of this source, an excellent cooling was not applied, thus the excellent output stability was not achieved at this stage. Optimized cooling might additionally improve the output stability.

To compare the performance of all lamps, the obtained output spectral power from the monochromator illuminated by these different lamps is summarized in **Fig**. 4.15.

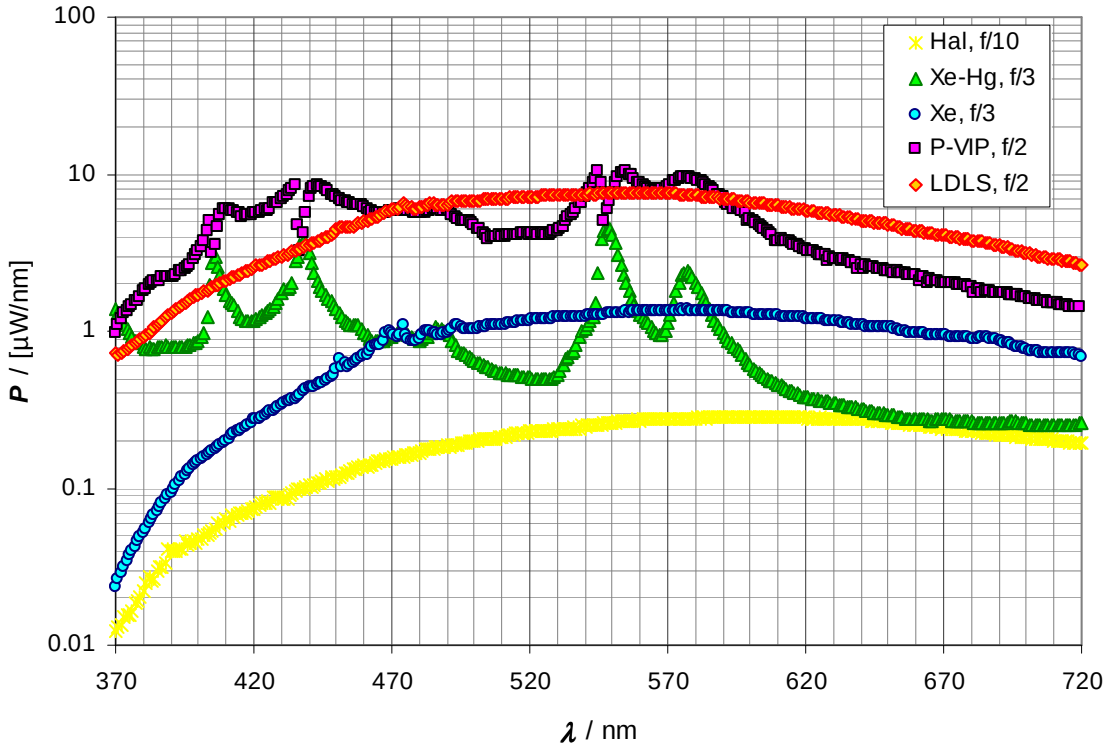

Figure 4.15 Output spectral power obtained by various lamps from the monochromator with an entrance and exit slit width of 0.5 mm

Although the output power is mostly the highest in the visible range for the P-VIP lamp, its stability is relatively poor, being larger than 1 % and its spectrum is not smooth compared to the other lamps. For the desired wavelengths (around 650 nm), the test laser driven light source yields the maximum output power. Additionally, it seems that the arc spot is well suitable for the monochromator, because the arc size is relatively small and the arc position does not change during the operation. As a result, it produces at least a 5 times higher spectral power than the Xe lamp and its stability is well within 0.1 %.

However, further investigation of this light source is needed to gain more experience for optimizing its application at this monochromator. Due to the late availability of this light source within the present work, these studies may be the topic of a subsequent work at PTB. For the present work the Xe lamp is found to be the optimum regarding the output power and the stability, thus it was further used in this set-up.

For the absolute calibration in radiance mode, an integrating sphere must be used to produce the lambertian radiation. Using an integrating sphere with one inch in radius and two 6 mm diameter ports, the spectral radiance level ranks from (1 to 8) mW/(m^2·nm·sr) in the wavelength range from 380 nm to 720 nm.

4.4 Characterization of the integrating sphere

The integrating sphere used for this set-up has an inner diameter of about 50 mm and two perpendicular openings with diameters of 6 mm, without a baffle between them. Although an imaging system with a magnification of about 3 has been obtained by the use of a mirror system, the spectral radiation from the monochromator can be completely focused into the input port as can be seen in **Fig**. 4.16.

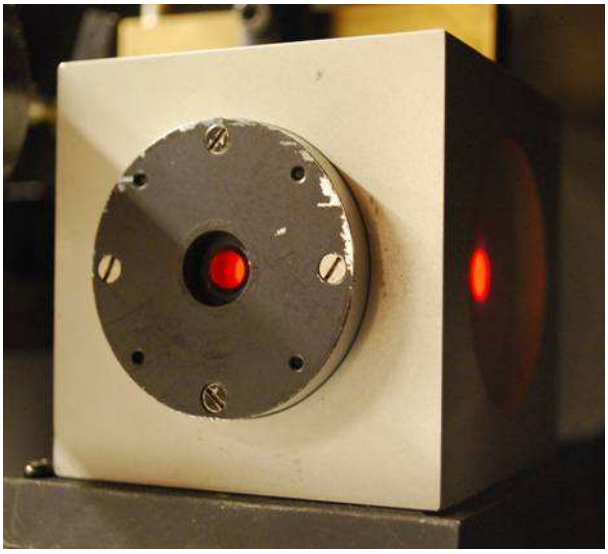

Figure 4.16 Photograph of the integrating sphere illuminated with the output radiation from the monochromator at 650 nm with a spectral bandwidth of 9 nm.

In this case, any liquid light guide or optical fibre to improve the uniformity of the sphere [46] is not useful because the incoming radiation through the fibre can reach the output opening, affecting to the uniformity of the output radiation. However, the emitting radiation from the output port must be investigated in order to characterize the integrating sphere as follows:

1) $\mathbf{Cos^4\theta}$ dependence for lambertian source

Before applying the integrating sphere for absolute calibrations, a characterization of the integrating sphere has to be performed to prove, whether the sphere is indeed a lambertian source or not. Any ideal lambertian source has an out-of-plane dependence for the irradiance of

$$E(r) = E_0(d)\cos^4\theta\,, \tag{4.2}$$

where $E(r)$ is the out of plane irradiance at a distance r
$E_0(d)$ is the in plane irradiance at a distance d
θ is the angle of the out of plane position.

Therefore, a measurement was performed by moving an irradiance detector in the horizontal plane at the certain distance *d* in front of the test integrating sphere as shown in **Fig.** 4.17.

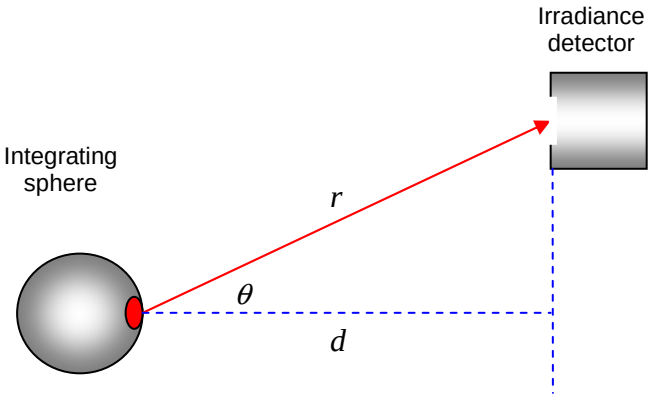

Figure 4.17 Schematic diagram for $\mathrm{Cos}^4\theta$ dependence measurement

The experimental result for the test integrating sphere in terms of relative irradiance compared to the theoretically expected values is plotted in **Fig.** 4.18.

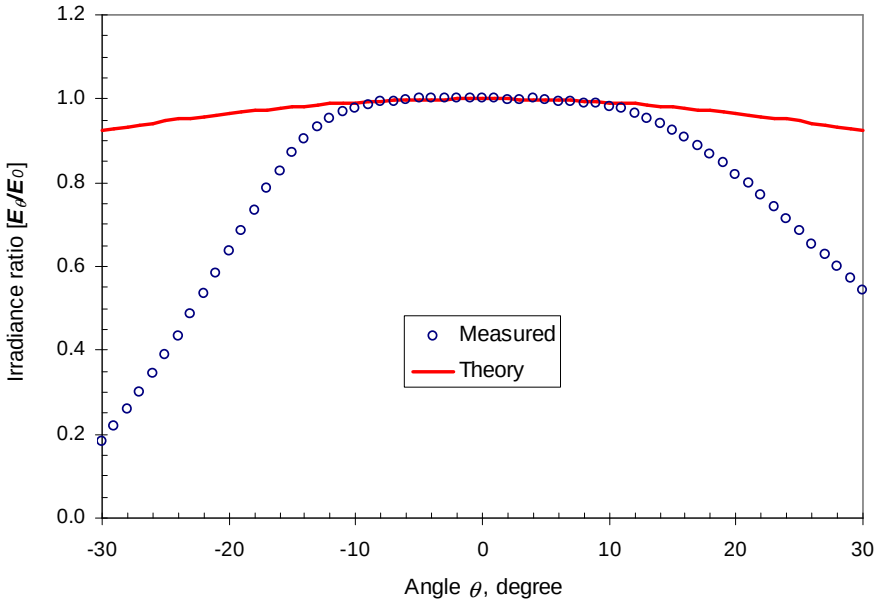

Figure 4.18 Cosine dependence for the used integrating sphere

It was obviously found that the output radiation obtained by this integrating sphere is lambertian only over a measured angle of ±9 degree and the relative differences from the theory in Eq. 4.2 are found to be within ±0.1 % in this range. However, the obtained half angle is large enough in comparison to a typical half angle of the field of views of a radiation thermometer, which usually does not exceed 3 degree.

2) Sphere radiance uniformity

Since this set-up will be applied to compare a radiance detector to an irradiance reference detector, the sphere uniformity contributes significantly to the uncertainty due to the different field of views (FOV) of the two detector types. Therefore, the spatial uniformity of the radiance across the integrating sphere opening was measured using a radiance detector with a spot diameter of approximately 1 mm. The result of this measurement is shown in **Fig.** 4.19.

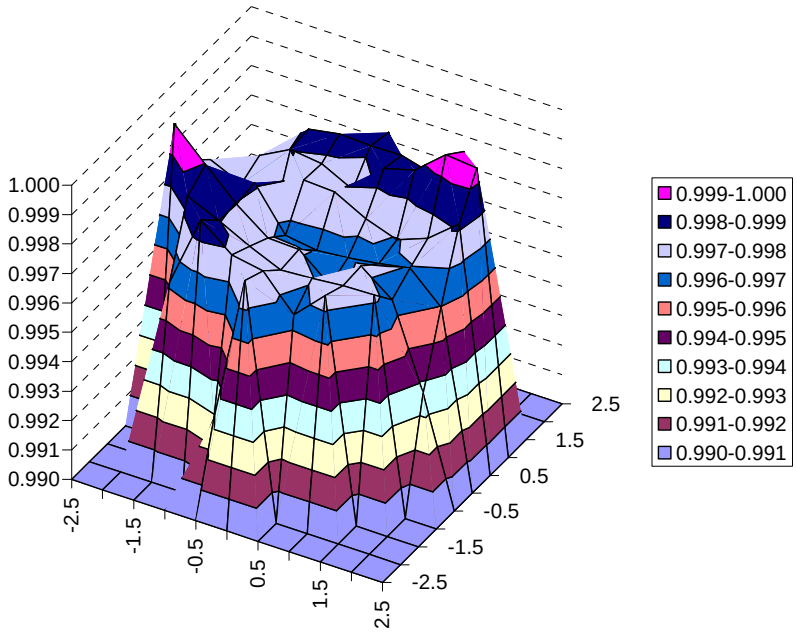

Figure 4.19 Spatial uniformity of the radiance across the radiating opening of the integrating sphere at 650 nm with a spectral bandwidth of 9 nm and a measuring spot diameter of 1 mm

As can be seen, the radiance uniformity across the 5 mm opening for the integrating sphere in this set-up is better than $\pm$ 0.2 %. However it seems that the uniformity depends on the quality of the supplied beam and also its incident position. In this measurement, the optical set-up behind the monochromator is arranged in the way to focus the spectral beam into the position as near as possible to the output port in order to avoid the first reflectance pass through the output port, affecting the sphere uniformity [46].

In addition, the spatial uniformity was also investigated by the use of a luminance camera LMK model 98-4 [58] in order to eliminate the short term signal drift during the scan using the radiance detector. Due to the low signal obtained by this camera, the noise level seems to be more than 1 % over the sphere opening. Therefore, applying this method, a spatial uniformity of the sphere better than 1 % cannot be detected by the camera.

However, an advantage of this camera is its high resolution, as it can detect small blinding spots on the inner surface of the integrating sphere, which can not be detected by the “one spot” radiance detector. A typical luminance image with two scans in vertical and horizontal across the sphere opening and their plots of relative signals are illustrated in **Fig**. 4.20. At least 3 blind spots can be observed in the vertical scan.

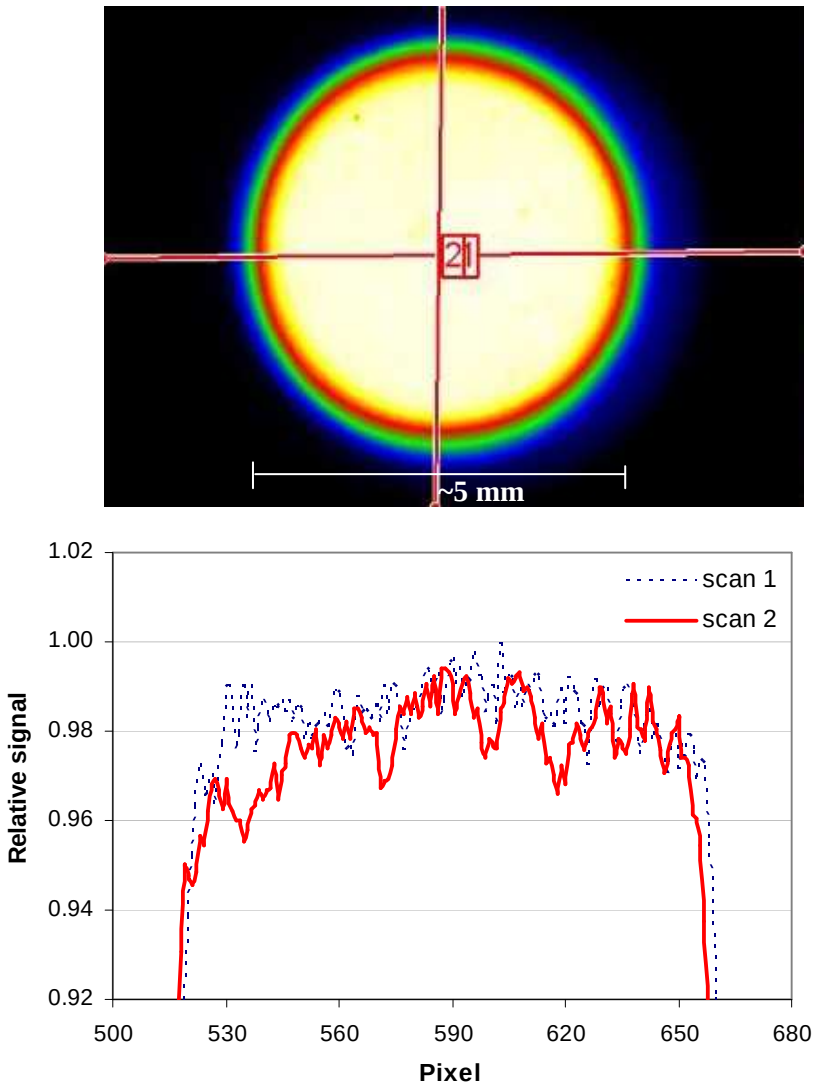

Figure 4.20 Illustration of the luminance image for the radiating opening of the integrating sphere using a LMK camera model 98-4.

The results above suggest that this investigation should be performed at the time receiving the integrating sphere to evaluate the quality of coating on the inner surface, which probably affects the sphere uniformity. Due to the late availability of this camera, its application will be further performed for new integrating spheres in the future work at PTB.

4.5 Characterization of the trap detector

In order to perform the calibration of a radiation thermometer, a reference detector is required to measure the input quantity of the radiation thermometer absolutely, i.e. the integrated radiance over the narrow spectral band of the filter. For highest accuracy measurements in the VIS and near IR wavelength region, a Si-trap detector, whose spectral power responsivity is traceable to the watt realised at the primary cryogenic radiometer of PTB, has been used as a reference detector in this set-up [38-41]. The spectral power responsivity of the trap detector used, calibrated at the spectral comparator facility [4] against a trap detector transfer standard is plotted in **Fig.** 4.21 along with the relative measurement uncertainty.

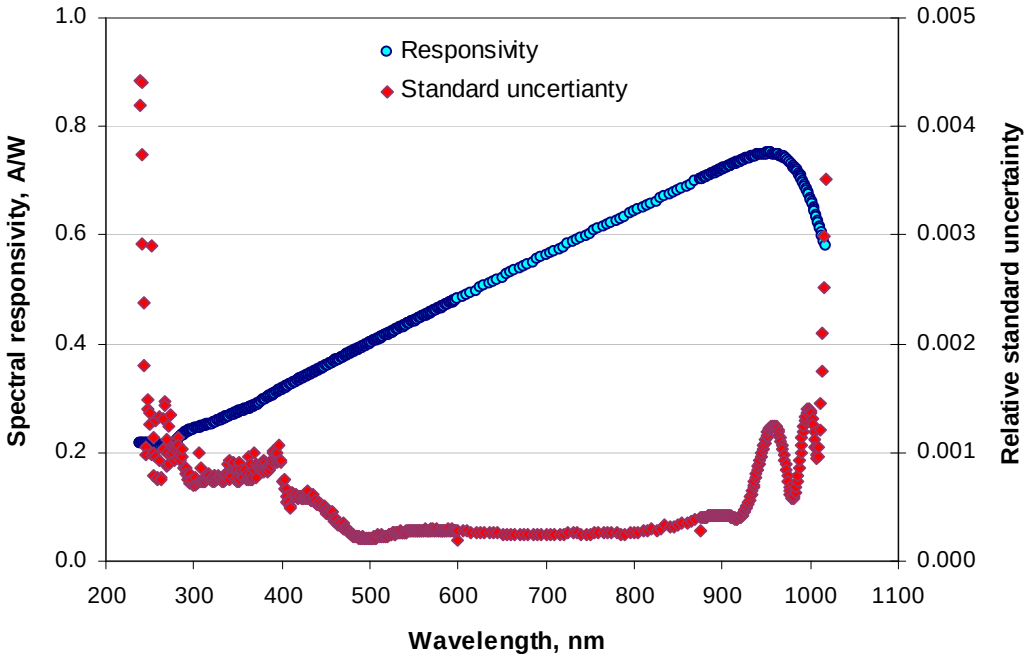

Figure 4.21 The spectral responsivity of the Si trap detector TS09 used as a transfer-standard calibrated at the spectral comparator facility, traceable to the cryogenic radiometer of PTB.

For the purpose of this work, the trap detector was used to measure the spectral radiance across the sphere opening by means of the two apertures method as mentioned in Section 2.4.5. Using the trap detector with a precision aperture, the spectral irradiance at a certain distance can be measured. With a second precision aperture at the sphere opening, the radiance of the sphere opening can be calculated from the measured irradiance. The optical set-up for the sphere radiance measurement using the trap detector is shown in **Fig**. 4.22.

It should be noted that each aperture was mounted on an individual adaptor, of which a front side circular plate was coated with a low reflectance paint to reduce the inter-reflections between the apertures. Additionally to further minimize the inter-reflections, a

blackened variable aperture was used as a baffle placed at the middle position between the two apertures [59].

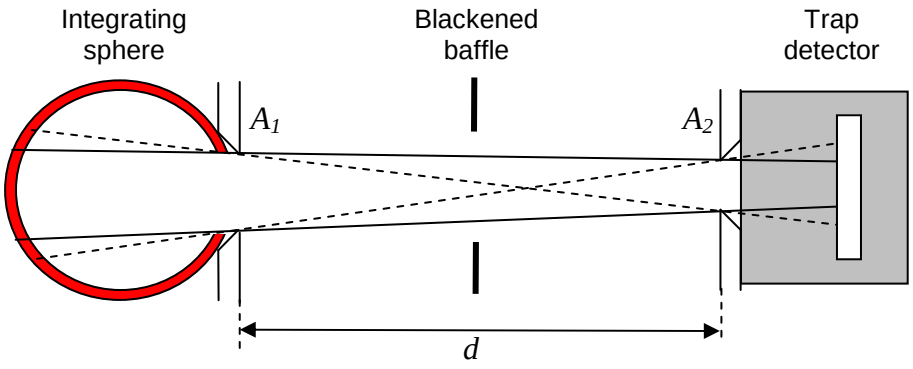

Figure 4.22 Optical set-up for the radiance measurement using the trap detector in combination with two precision apertures

For calculation of the radiance via the irradiance measurement, the geometric factor G must be calculated according to Eq. 2.20 in Section 2.4.5 as follows

$$G(d) = \frac{2\pi r_1^2}{r_1^2 + r_2^2 + d^2 + \sqrt{(r_1^2 + r_2^2 + d^2)^2 - 4r_1^2 r_2^2}}, \tag{4.3}$$

where r_1 and r_2 are the radii of the apertures in front of the radiation source and the detector, and d is the distance between these apertures. Therefore, absolute areas of both apertures and the distance between them must be accurately known.

The diameter of the two apertures can be accurately measured via an absolute calibration using a non-contact laser method described in [60]. The nominal value of both apertures is 5 mm in diameter with an absolute uncertainty of 0.4 µm.

For the distance measurement, a combination of a relative measurement using an interferometer and an absolute zero is required. Because of the limitation of the radiant power obtained from the monochromator, the trap detector has to be placed at a distance shorter than 200 mm in front of the sphere aperture to obtain sufficient power (S/N ratio > 10^3). Therefore, an interferometer-based measurement of the distance with an uncertainty of 1 µm has to be performed to yield a sufficiently low relative distance measurement uncertainty. For an interferometer-based relative distance measurement, an absolute zero must be known in order to known an absolute distance between two apertures. In this set-up, a linear stage is used in combination with a length gauge with a display (resolution of 5 µm). At first the trap detector and the sphere must be aligned to the same optical axis. Then the absolute position can be found by moving the trap detector to the integrating sphere until defined positions at their housings are in the same plane. Finally, using two

precisely determined distances between their defined positions at their housings and the limiting aperture surfaces, the absolute aperture distance can be calculated within an uncertainty smaller than 50 μm.

In order to use the trap detector for absolute radiance measurements, some effects have to be evaluated both in experiment and theory as follows.

1) Distance dependence of irradiance-radiance transfer

The used trap detector is constructed using three Si-photodiodes whereas the length of the optical path from the opening to the last reflection of the photodiodes is 80 mm and the photodiode size is 12.7 in diameter. A necessary criteria to measure the optical power using a trap detector is that the incoming radiation must under-fill all of the photodiodes. Using the geometry of the measurements performed here, the shortest distance by this trap is limited to 104 mm, where the 12.6 mm diameter photodiode is still completely under filled by the incoming beam. However, since the trap detector was calibrated at a spectral comparator using a collimated spectral radiation of 6 mm in diameter, the distance dependence on radiance measurement due to possible stray light and reflection effects must be investigated by measuring the irradiance at any distance from the sphere and converted to the radiance by using the geometric factor in Eq. 4.3. The resulting ratio between the measured radiance at any distance and the maximum radiance is considered as the distance effect on irradiance-radiance transfer as shown in **Fig.** 4.23.

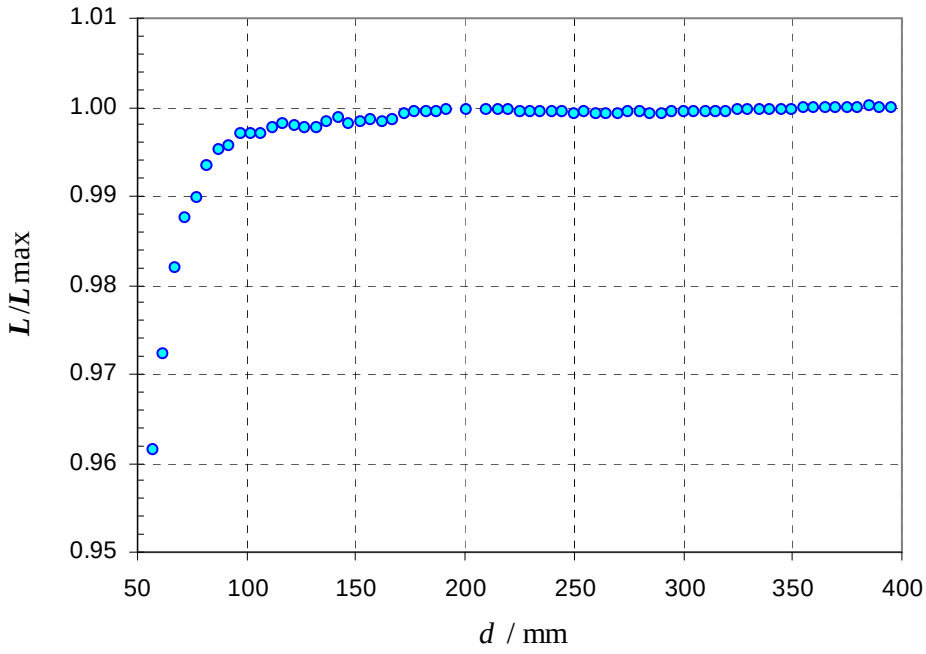

Figure 4.23 Distance effect on irradiance-radiance transfer by the trap detector

It was found that the distance effect on the radiance is not significant for distances longer than 180 mm. Although this effect can not be observed at a distance longer than 400 mm due to limit of the optical power, looking at **Fig**. 4.23, it can be assumed that the distance effect can be also neglected at longer distances.

2) Diffraction error

Since the sphere emits radiation through the two small apertures until reaching the first photodiode in the trap detector, diffraction effects occur at these apertures. The diffraction might affect the measured radiation flux. Therefore, a correction due to this diffraction effect has to be considered for this set-up. In general for small diffraction corrections, the correction can be applied by calculating the diffraction effect ε occurring at every aperture separately and correct the measured radiation flux ϕ is with respect to the non-diffracted flux ϕ_0 by the following equation:

$$\phi = (1+\varepsilon)\phi_0 . \tag{4.4}$$

In this case the diffraction effect at both apertures is independently considered and can be linearly combined for the complete correction.

According to the diffraction theory in [61, 62], the diffraction correction at any aperture can be approximately calculated using the measurement geometry and desired wavelengths. For an application to calibrate the 650 nm narrow band radiation thermometer, the diffraction corrections are simply calculated only at 650 nm and shown in **Fig**. 4.24.

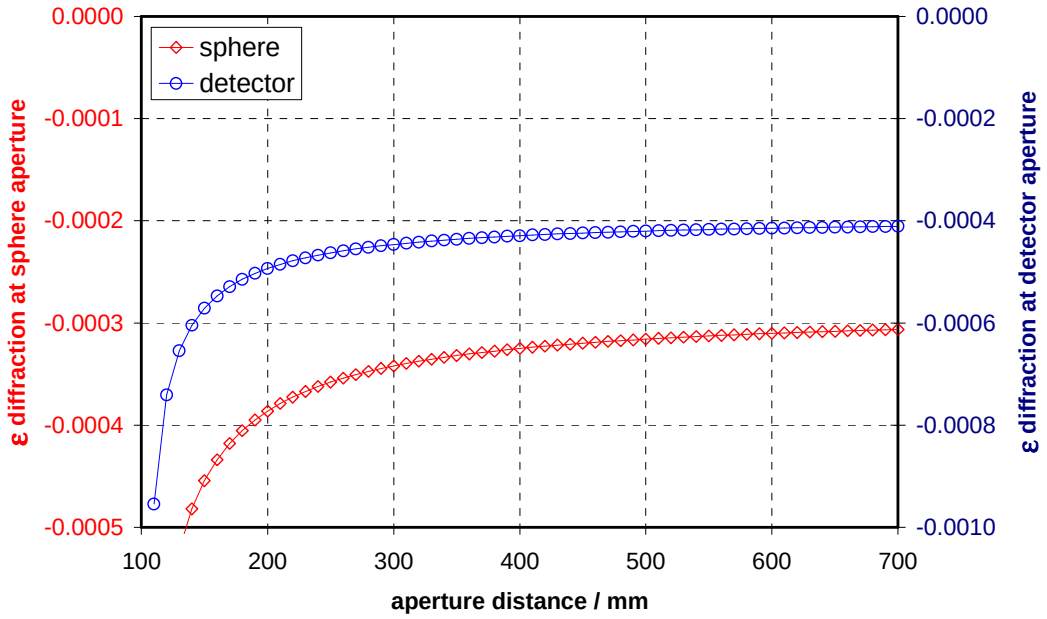

Figure 4.24 Approximate diffraction errors at 2 apertures at 650 nm for various distances

From the calculations, it was found that the total correction is 0.09 % at a distance of 200 mm up to 0.07 % at a distance of 700 mm, corresponding to the measuring distance of a radiation thermometer. These approximate corrections will be used as a component of uncertainty in the next chapter.

4.6 Discussion

After the full investigation and optimization of this set-up, the spectral power obtained from the monochromator is currently higher than 1 μW/nm covering the wavelength range from 500 nm to 700 nm using the Xe lamp. The P-VIP lamp could be a better radiation source for this set-up in case its stability is significantly improved. The laser driven light source is probably the source of choice for this set-up, however the coupling of the lamp into the monochromator must be optimized and a good thermal management is required for this source. Another solution to increase the signal level of the set-up could be the possible application of a supercontinuum lasers as input source for the monochromator. The continuous spectrum laser sources are currently available with a spectral power of up to 5 mW/nm and a beam diameter of approximately 1 mm in the visible region and 2 mm in the near infrared region. As the same grating with the linear dispersion of 2 nm/mm is still used, an output spectral power from the monochromator of at least 1 mW/nm would be achieved. However, their instabilities of the supercontinuum source due to noise are wavelength dependent by varying from 0.4 % to 2 % for the averaging time of 30 second [63].

In case the power problem is solved, an integrating sphere with larger diameter should be applied to improve its radiance uniformity across the opening to be well within 0.1%. In addition, if the new sphere has a baffle between its opening ports, the sphere uniformity may be further improved by the use of a visible liquid light guide, due to its large radiating solid angle [46]. With the core diameter of 3 mm to 8 mm, the spectral radiation from the monochromator exit port could be completely coupled into the light guide [64].

In the next chapter, the absolute calibration of radiation thermometers in radiance mode with the developed set-up will be described in detail.

5 Absolute spectral responsivity calibration of radiation thermometers

In this work, for its absolute radiometric calibration, a radiation thermometer has been calibrated in terms of its spectral radiance responsivity by comparison to an absolutely calibrated Si trap detector, traceable to the primary cryogenic radiometer of PTB in terms of electrical current per radiant power at several wavelengths [65]. Therefore, the spectral radiance responsivity of a test radiation thermometer can be defined by

$$s_{\mathrm{RT}}^{L}(\lambda) = \frac{I_{\mathrm{ph,RT}}}{L_{\mathrm{Sphere}}(\lambda)}, \tag{5.1}$$

where $I_{ph,\mathrm{RT}}$ are the output photocurrents obtained from the test radiation thermometer and $L_{\mathrm{Sphere}}(\lambda)$ is the input measured quantity of test radiation thermometer e.g. absolute spectral radiance radiating from an integrating sphere.

The trap detector is employed to determine the absolute spectral radiance by measuring the spectral irradiance $E_{\mathrm{Trap}}(\lambda)$ in combination with two precision apertures as defined by

$$E_{\mathrm{Trap}}(\lambda) = L_{\mathrm{Sphere}}(\lambda) \cdot G(r_1, r_2, d). \tag{5.2}$$

With known effective areas of the apertures associated to r_1, r_2 and the distance between these two apertures d, the geometric factor G of the radiance measurement can be calculated as shown in Eq. 4.3.

From the definition of the spectral power responsivity in Eq. 2.23, the absolute spectral irradiance responsivity of the trap detector can be also written as [65]

$$s_{\mathrm{Trap}}^{E}(\lambda) = \frac{I_{\mathrm{ph,Trap}}}{E_{\mathrm{Trap}}(\lambda)}, \tag{5.3}$$

where $I_{\mathrm{ph,Trap}}$ are the output photocurrents obtained from the trap detector during the measurement and $E_{\mathrm{Trap}}(\lambda)$ the spectral irradiance at the opening of the trap detector. .

Finally, the calculated spectral radiance is then compared to the photocurrent generated by the radiation thermometer to determine its absolute spectral radiance responsivity of the radiation thermometer via

$$s_{\mathrm{RT}}^{L}(\lambda) = G(r_1, r_2, d) \cdot \frac{I_{\mathrm{ph,RT}}}{I_{\mathrm{Trap}}} \cdot s_{\mathrm{Trap}}^{E}(\lambda), \tag{5.4}$$

5.1 LP3 radiation thermometer

In this study, a LP3-type radiation thermometer manufactured by KE Technologie GmbH (Germany) has been selected to be absolutely calibrated due to its high accuracy and low size of source effect. The LP3 consists of a selected single silicon photodiode, a set of interference and neutral density filters and an optical system. A schematic of the LP3 is given in **Fig**. 5.1.

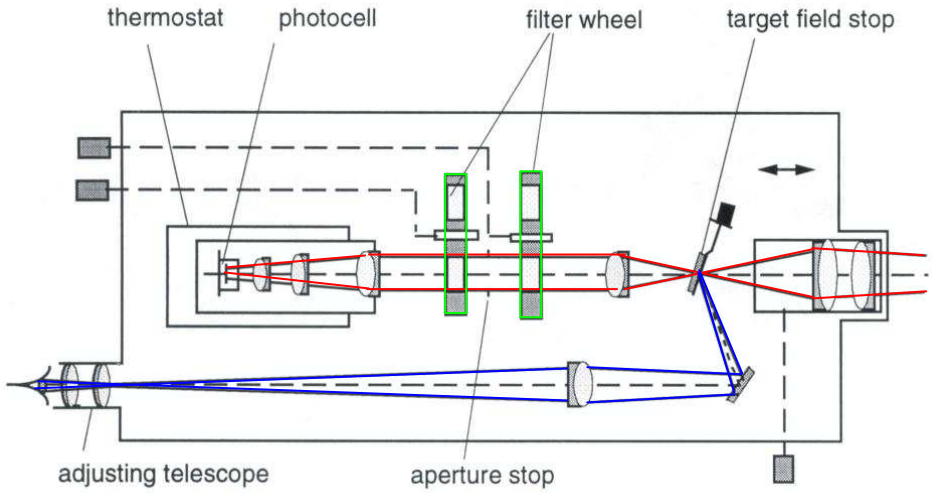

Figure 5.1 Schematic diagram of the LP3 radiation thermometer

With the optical systems, the measuring spot is approximately 0.8 mm in diameter at a measurement distance of 700 mm. Using an optimized amplification system, the measurable photocurrent ranks from 50 pA to 800 nA, corresponding to the radiance temperature range from 800 °C to 3000 °C. The interference filters used in the LP3 have center wavelengths around 650 nm and 950 nm, with a FWHM of about 10 nm. For application at high temperature measurements, the LP3 was absolutely calibrated only with the 650 nm interference filter. For convenient operation, the Si photodiode is kept to a temperature of 29.5 °C in a stabilized temperature housing, yielding a noise photocurrent of 2.5 fA, equivalent to a few mK in temperature.

In this work, two LP3 radiation thermometers were absolutely calibrated at both, the monochromator-based facility and the Tuneable Lasers in Photometry (TULIP) set-up of PTB in the wavelength range from 400 nm to 1100 nm. Calibration results obtained by the two set-ups for the same radiation thermometer are compared and checked by measuring the temperatures of high temperature fixed-points.

5.2 Monochromator-based absolute calibration

As mentioned in the last chapter, the absolute calibration was performed at the developed monochromator-based set-up using the Xe lamp as a light source.

5.2.1 Monochromator-based calibration

For the calibration of the LP3 radiation thermometer with the 650 nm interference filter, a spectral bandwidth of at most 1 nm in its bandwidth region is required at the monochromator-based set-up to accurately follow the spectral bandpass of around 30 nm. Therefore the slit width of the monochromator described in the last chapter is set to 0.5 mm. The trap detector and the radiation thermometer LP3 under test were placed at the same optical axis perpendicular to the sphere aperture plane at the distance of about 200 mm and 700 mm, respectively. The optical alignment was done by applying an alignment laser. Before every measurement, a scan using the trap detector across the sphere opening has to be done to find out the center position by fitting the obtained curve with a polynomial equation.

In the measurement process, the direct substitute comparison was basically performed at each selected wavelength by using a translation stage to move the trap detector relatively to the fitted center position at the certain distances in front of the radiation thermometer in a light tight box. In a first step the photocurrent of the trap detector, $I_{\mathrm{ph,Trap}}$, the dark current of the LP3, $I_{\mathrm{d,LP3}}$, and also the photocurrent of the monitor diode, I_{Mon} were measured at the same time. In a second step the trap detector was moved away to a position behind the baffle and then the dark current of the trap detector, $I_{\mathrm{d,Trap}}$, the photocurrent of the LP3, $I_{\mathrm{ph,LP3}}$ and also the photocurrent of the monitor diode were measured again. Finally the spectral responsivity of the LP3 at this wavelength was calculated by

$$s_{\mathrm{LP3}}^{L}(\lambda) = G \cdot \frac{I_{\mathrm{ph,LP3}} - I_{\mathrm{d,LP3}}}{I_{\mathrm{ph,Trap}} - I_{\mathrm{d,Trap}}} \cdot \frac{I_{\mathrm{Mon}}^{\mathrm{Trap}}}{I_{\mathrm{Mon}}^{\mathrm{LP3}}} \cdot s_{\mathrm{Trap}}^{E}(\lambda)\,. \tag{5.5}$$

The measurement was performed 5 times to evaluate the repeatability and was repeated for every wavelength to cover the range from 635 nm to 665 nm. All processes in the measurement were controlled and monitored by a computer.

For relative spectral responsivity measurements, the integrating sphere is replaced by a mirror and an adjustable aperture to feed the spectral radiation with matching *f*-number in-filled to the optics of the LP3, unlike the previous measurement in [50] to delete an effect from the wavelength dependence of objective lens transmittance. This method was found to be better than the method without an objective lens as confirmed in Ref. 66. The measurement process is the same as for the absolute method, but performed in the wavelength range from 400 nm to 1000 nm with the spectral bandwidth of 1 nm and 5 nm in the bandpass and in the blocking region of the LP3. The obtained relative spectral responsivity $R_{\mathrm{LP3}}(\lambda)$ will be used to calculate the absolute out-of-band responsivity by

$$s_{\mathrm{LP3}}(\lambda_{\mathrm{Block}}) = R_{\mathrm{LP3}}(\lambda_{\mathrm{Block}}) \cdot \frac{\int_{\mathrm{Bandpass}} s_{\mathrm{LP3}}(\lambda)d\lambda}{\int_{\mathrm{Bandpass}} R_{\mathrm{LP3}}(\lambda)d\lambda}\,. \tag{5.6}$$

5.2.2 Calibration results

At first, a series of relative measurements without the integrating sphere were performed to investigate the performance of the single monochromator and to characterize the fine structure of the test LP3 with different bandwidths. In the wavelength range from 400 nm to 1000 nm, measurements were conducted with bandwidths of 1 nm and 5 nm to measure the stray light of the monochromator. It was found that the stray-light level for this single-monochromator is sufficiently suppressed to be less than 10^{-5} even for a monochromator bandwidth of 1 nm. As a result, the out-of-band responsivity of the LP3 measured on this set-up will be limited by this level.

Within the bandpass region of the LP3's interference filter, relative measurements were performed with the spectral bandwidths of 0.2 nm and 0.1 nm, respectively, to find the optimum spectral bandwidth for calibration of the LP3. An oscillation pattern in spectral responsivity was not observed even for a bandwidth of 0.1 nm, which is in contrast to previous results obtained from another LP3 (Ser. No. 8013) [51] as shown in **Fig** 5.2. However, since the relative difference between the integral responsivity for 0.2 nm and 0.1 nm is less than 5×10^{-4}, a spectral bandwidth of 0.2 nm should be used in favor of a time effective measurement due to higher signal to noise ratios.

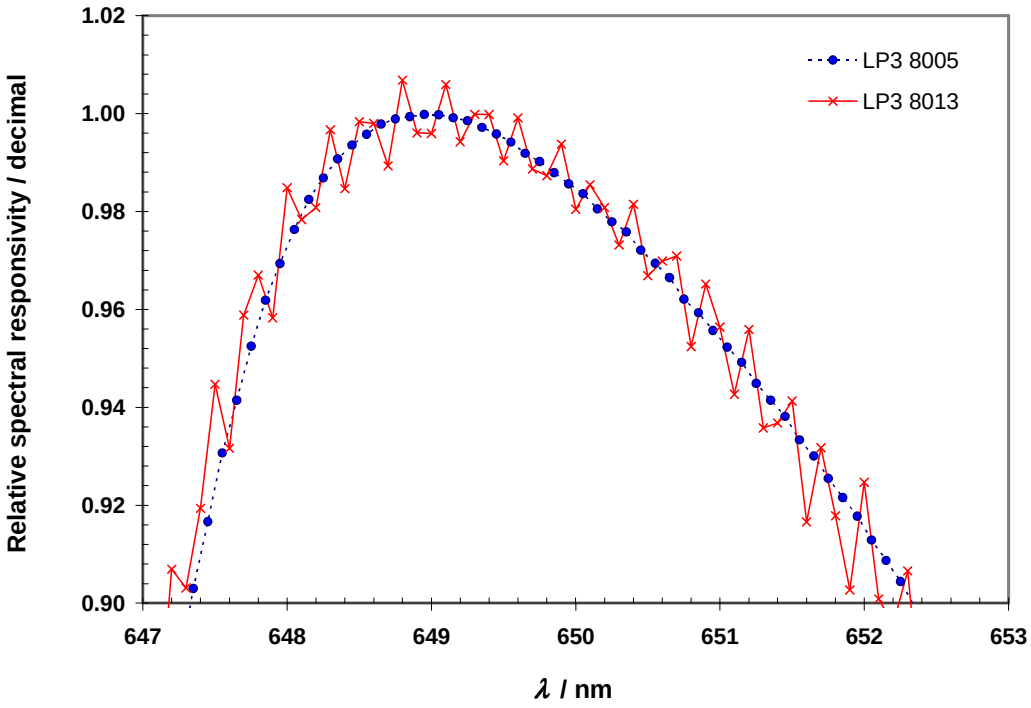

Figure 5.2 Relative spectral radiance responsivity of the LP3 8005 and LP3 8013 with a spectral bandwidth of 0.1 nm measured at the monochromator-based set-up [51].

By applying an integrating sphere for absolute calibration, the dynamic range of the monochromator set-up was far lower than for the relative measurement, where most of the total radiation was directly introduced into the LP3's field of view. With an effective bandwidth of 1 nm, the signal-to-noise ratio of the LP3 at the peak wavelength was approximately 10^3 when using an integrating sphere with 2 inches in diameter. With the expected bandwidth of 0.2 nm, the LP3's signal-to-noise ratios were lower than the required level ($\geq 10^3$), hence a spectral bandwidth of 1 nm is still used to measure in the bandpass region (650 nm $\pm$ 15 nm) for the absolute measurement. During the calibration, five runs were taken to evaluate the repeatability of the measurements, resulting in a relative repeatability of the integral responsivity of 5.3×10^{-4}, while the repeatability of the effective wavelength for each run is better than 25 pm. In the blocking region, the results of the relative measurements were used by adjusting them with an absolute result at the peak wavelength to determine the absolute out-of-band responsivity of the LP3. The absolute spectral radiance responsivity of the LP3 is shown in **Fig**. 5.5, comparing to the measurement results obtained with the laser-based facility.

5.3 Laser-based absolute calibration

In order to evaluate the performance of the new monochromator set-up, the absolute calibration of the same LP3 was also performed at the PTB tuneable laser-based facility.

5.3.1 Laser-based facility

Fig. 5.3 is a schematic diagram of the TULIP laser-based facility at PTB. A series of continuous wave tuneable laser sources are used as radiation sources in different wavelength regions. By using an intensity stabilizer, the laser output power is controlled within 0.02 % and the laser wavelength, measured by a wavemeter, is stable within 0.001 nm. To calibrate filter radiometers both in radiance or irradiance mode, the laser radiation above 450 nm is introduced into a 2 inches integrating sphere by using a liquid light guide and a vibration motor to reduce the interference due to the coherence of the laser radiation, which otherwise introduces a speckle pattern. The direct substitution comparison was also performed by using translation stages to move the trap detector and the test radiation thermometer to the measurement position. Due to the high laser power, the spectral radiance measured by the trap detector can be performed at the same distance as the radiation thermometer (700 mm). A monitor diode is also applied to correct for any drifts of the laser power between the trap and the radiation thermometer signals.

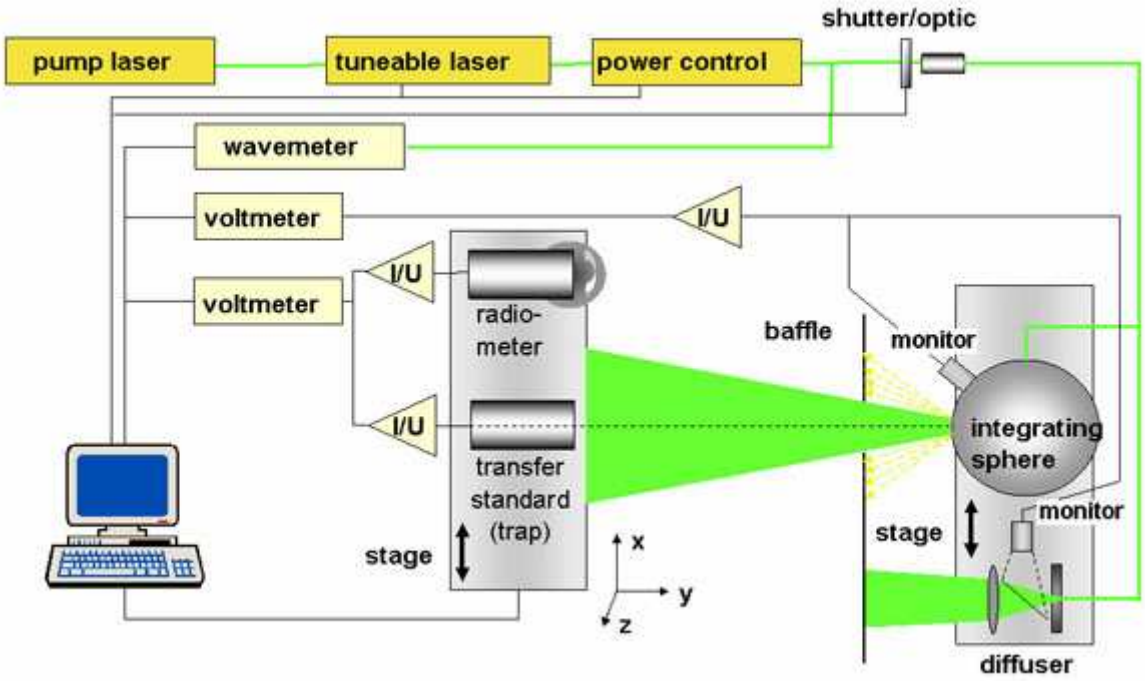

Figure 5.3 Schematic diagram of the laser-based calibration facility [53].

It should be noted that the absolute calibration on both facilities was performed using unpolarized light from the integrating sphere, which is very useful for an application of the LP3 at the blackbody radiator, which is an unpolarized source.

5.3.2 Laser-based calibration result

Due to the relative calibration results presented as shown in **Fig.** 5.2, it was assumed that the interference effect in spectral responsivity during calibration with laser sources will be lower for the LP3 8005 than for the LP3 8013, for which an amplitude of about 5 % was found around the peak wavelength as shown in **Fig**. 5.4. For this reason, the measurement for the LP3 8013 was incompletely performed at TULIP but completely performed for the LP3 8005.

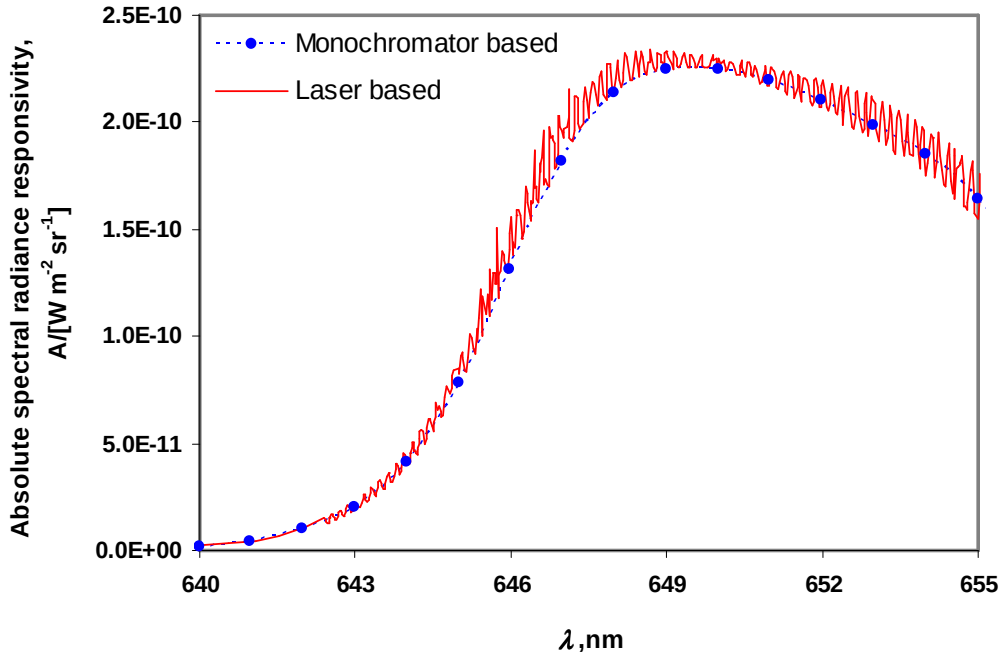

Figure 5.4 Spectral radiance responsivity of the LP3 8013 measured on both facilities without additional efforts to avoid or correct for the interference effect.

At the TULIP facility, the measurement was performed around the bandpass of the LP3. Therefore a DCM dye laser, whose output wavelengths can be controlled in the range from 605 nm to 685 nm, was used for these measurements. The wavelength step was 0.01 nm from 620 nm to 680 nm to accurately follow the oscillation pattern in the spectral responsivity due to the interference fringes. To evaluate the out-of band responsivity of the LP3 under test, a titanium: sapphire laser and a quasi-cw laser system was used. Due to the high spectral resolution of the laser wavelengths, the period of the oscillation pattern was determined with sufficient sampling to eliminate the interference fringes in the measured responsivity.

The absolute spectral radiance responsivity of the LP3 8005 obtained with the two facilities are plotted over the measured wavelength range on a logarithmic scale in **Fig.** 5.5 (a) and close to the center wavelength showing the fine structure on a linear scale in **Fig.** 5.5 (b) with the band width of 1 nm for the monochromator-based facility. It can be clearly seen that out-of-band responsivity values of the LP3 by the monochromator-based measurement are of least one order of magnitude larger than that from the laser-based measurement. Even with such a level, total relative integral in the blocking region does not contribute significantly to thermodynamic temperature measurements by using this radiation thermometer, especially in the high temperature range. However this effect appears to be significant by 0.02 %, contributing to 18 mK for temperature measurements at 1100 °C, and will be considered as a source of uncertainty for the absolute calibration.

a)

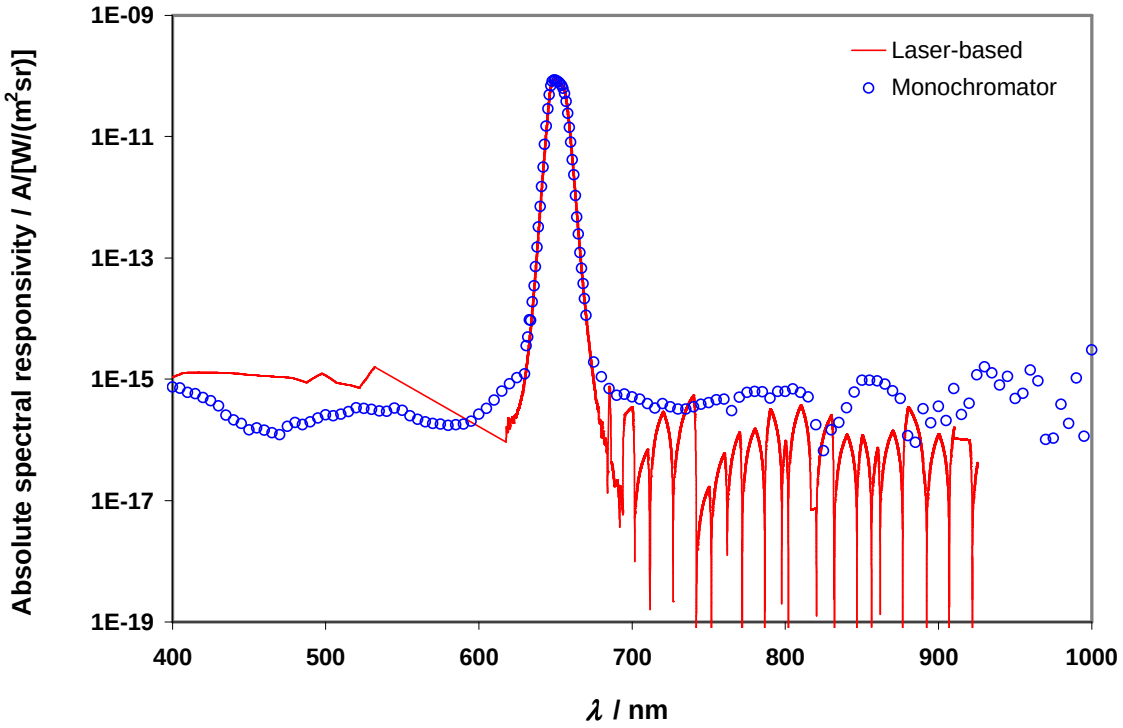

(b)

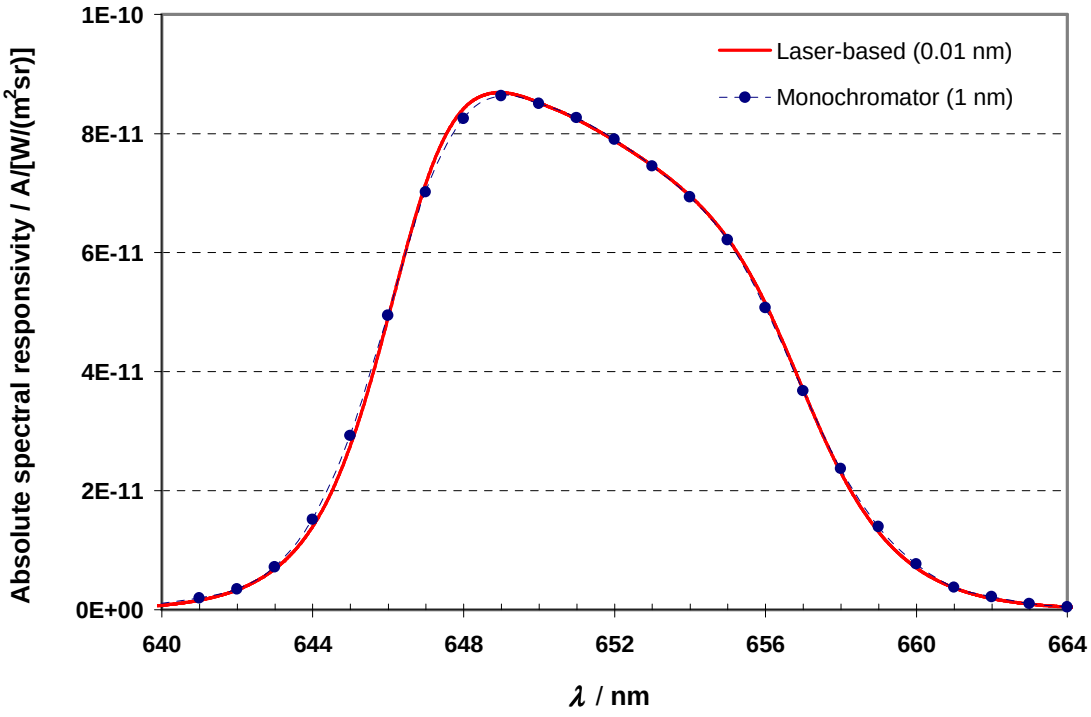

Figure 5.5 Absolute spectral radiance responsivity of the LP3 8005 measured on both facilities: a) logarithmic scale, b) bandpass close-up on a linear scale

As can be seen in **Fig.** 5.5 b), differences in spectral responsivity on both facilities were found at some wavelength ranges. It should be noted that both results were obtained with different bandwidths, and therefore can not be compared directly. An averaging of the calibration results on the laser-based facility for the same spectral bandwidth on the monochromator-based facility should be performed to compare both results directly. Differences between the results at the monochromator-based facility and the average results at the laser-based facility are shown in **Fig**. 5.6.

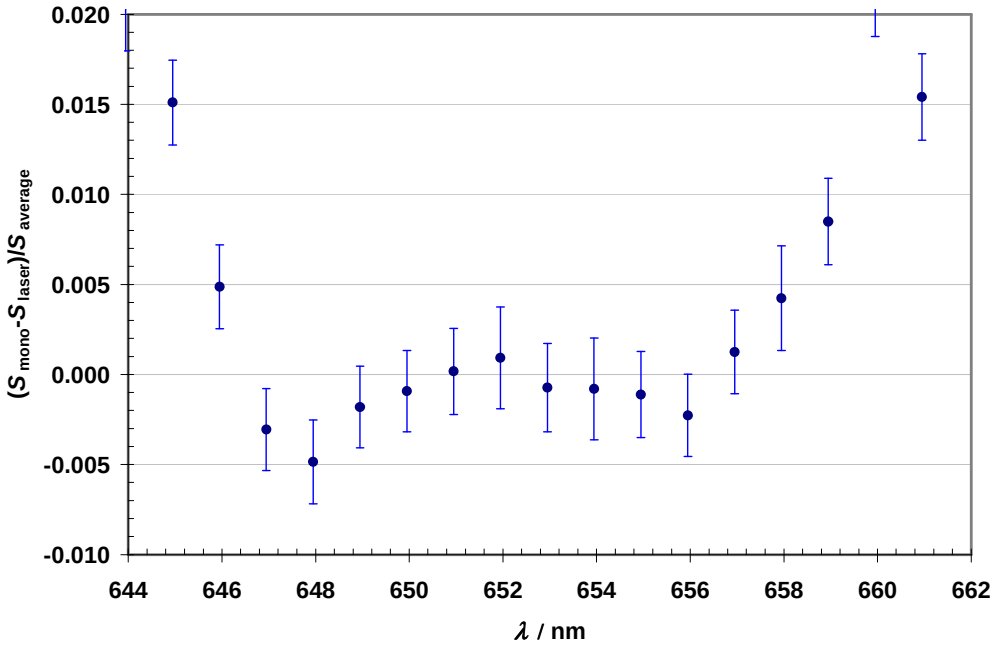

Figure 5.6 Differences in spectral responsivity between the results at the monochromator-based facility and the averaging results at the laser-based facility with the spectral bandwidth of 1 nm.

It was found that the differences are within their combined uncertainties only in the wavelength range from 649 nm to 657 nm. At other wavelengths between the bandpass and blocking region, the differences increase rapidly, due to the bandwidth effect of 1 nm and the high level of stray light at the monochromator set-up (10^{-5}), compared to that of the laser-based facility (10^{-7}).

In order to evaluate the agreement between the two calibration methods, two parameters obtained from the measurement results were compared. In case of the effective wavelength, a systematic wavelength difference of less than 13 pm was observed.

Finally the integral responsivity over the calibration range from 630 nm to 670 nm was calculated for both facilities and compared with each other. It was found that a relative difference of the measured integral responsivity for both facilities is 0.29 %, which is within their combined uncertainty (k = 2), which will be described in Section 5.4.

5.4 Uncertainty estimation

Relevant uncertainty components associated with the absolute spectral radiance calibration at the monochromator-based set-up and laser based facilities are summarized in **Table** 5.1. All components are given as standard uncertainties at a coverage factor of k = 1.

One of the main contributions to the uncertainty is the uncertainty due to spatial uniformity of the spectral radiance across the integrating sphere opening u_1, which is expected to decrease for increasing sphere diameter [67]. However, a larger integrating sphere is not a straightforward solution to solve this problem, because for a fixed opening area, the output radiance quadratically decreases with an increasing sphere radius. Presently, the best radiance uniformity across the 5 mm aperture for the 50 mm integrating spheres at both facilities is within $\pm$0.2 %. Although a correction of the non-uniformity can be in principle applied for any measurement, it increases the overall uncertainty due to the uncertainty of the uniformity measurement. In this work, the estimated uncertainty due to the sphere uniformity is 0.115 %, without any correction.

By applying the monitor diodes, the temporal instabilities of the radiation sources are almost negligible for the laser-based facility. Although a correction due to the temporal instability of the radiation sources was applied by using the monitor diode, the uncertainty due to the temporal instability u_2 is still 0.067 % for the monochromator set-up due to the rapidly fluctuation of the output radiation emitting by the xenon lamp. This effect is seemed to be significant for the monochromator set-up because the input power at the entrance slit is sensitive to the exact position and shape of the arc.

Since an uncertainty contribution due to signal to noise ratio decreases with increasing radiant power, the repeatability of the integral responsivity u_3 is currently limited to 0.053 %, calculated from the standard deviation of five runs for the monochromator-based method. The repeatability at the laser-based set-up mainly depends on the amplitude of the interference patterns. Since the interference effect was corrected, an uncertainty due to a correction of the interference effect was considered into the uncertainty budget for the laser-based calibration.

The calibration uncertainty of the spectral responsivity of the trap detector is already shown in **Fig**. 4.16. Since the LP3 mainly responses in the wavelength from 630 nm to 670 nm, the calibration uncertainty of the trap detector is considered only in this wavelength range. As the calibration uncertainty of the trap detector is nearly constant over the entire wavelength range, the uncertainty contribution due to the trap detector u_4 is estimated by averaging the uncertainty in the wavelength range.

According to the absolute calibration using a non-contact laser method described in [60], the nominal value of the used apertures is 5 mm in diameter with an absolute uncertainty of 0.4 μm. As a result, the uncertainty contribution due to aperture area u_5 is summarized from the two apertures and found to be 0.023 %. From the measurement of distance between the two apertures as mentioned in section 4.5, the measurement uncertainty of 50 μm can be achieved. The uncertainty contribution regarding to the distance measurement u_6 is estimated to be 0.05 % for the setting distance of about 200 mm. From the calculation of diffraction error at the two apertures, it was found that the total error is 0.09 % at the measuring distance. This approximate error is not used to correct the measuring signal but considered as the uncertainty contribution due to the diffraction u_7.

The uncertainty in wavelength is less than 1 pm for the tuneable laser and less then 30 pm for the monochromator based set-up in a temperature-controlled room. However a careful wavelength check using a mercury spectral lamp is required prior to each measurement at the monochromator set-up. From Eq. 2.12, the uncertainty due to the wavelength error u_8 is found to be 0.046 % for the application at the gold point.

Due to the bandwidth of 1 nm at the monochromator, the bandwidth error is considered as one of the uncertainty component, which can be estimated by an experiment or the calculation described in Ref. 68. In the experiment, this component of uncertainty for the monochromator and the LP3 can be evaluated by measuring the responsivity of the LP3 for different monochromator bandwidths. It was found that the uncertainty due to the bandwidth effect u_9 for the LP3 is less than 0.04 %, comparable to the prediction according to the method in Ref. 68. From the calculation, this component can be reduced to be less than 0.01 % by using the spectral bandwidth of smaller than 0.5 nm.

As discussed in section 5.3.2, the stray light level in the single monochromator-based system is limited at 10^{-5} level and must be considered as an uncertainty component for the absolute calibration. In this work, relative difference in the out-of-band integral responsivity between the monochromator-based and the laser-based facility is considered to be the uncertainty due to the stray light effect u_{10}, resulting relative uncertainty is estimated to lower than 0.01%.

Finally, the overall uncertainty ($k = 1$) is within 0.17 % for the monochromator-based method and 0.14 % for the laser-based method. At this stage, a correction due to non-linearity of the radiation thermometer under test was not considered, even though both of the absolute calibrations are performed at different signal levels, because recent results showed no significant non-linearity of the used radiation thermometer [69].

Table 5.1 Summary of the relative uncertainty contributions of the absolute spectral responsivity of the LP3 8005

Quantity	Contributions of uncertainty	Monochromator-based (%) (k = 1)
u_1	Spatial homogeneity	0.115
u_2	Source instability	0.067
u_3	Repeatability	0.053
u_4	Spectral responsivity of trap	0.025
u_5	Aperture area	0.023
u_6	Distance	0.050
u_7	Diffraction at 2 apertures	0.045
u_8	Effective wavelength	0.046
u_9	Bandwidth effect	0.040
u_{10}	Stray light effect	0.010
u (k=1)	Squared sum	0.174

5.5 Conclusions and discussions

For the radiation thermometer of type LP3, the optimal bandwidth of the monochromator should be larger than 0.2 nm to avoid the interference effect in the spectral responsivity even with the incoherent source from the lamp-monochromator-based set-up. With a 0.2 nm spectral bandwidth, the fine structure in spectral responsivity is completely averaged over the actual bandwidth, as a result, the interference can not be observed anymore. As this is the situation in the later application it may be supposed that such a measurement avoiding the interference effects could yield the lowest uncertainty. However, due to the limited output power from the monochromator, the absolute calibration was performed with the spectral bandwidth of 1 nm, yielding the measurement uncertainty of below 0.2 % (k = 1).

The main advantages of the tuneable laser are its much higher signal-to-noise ratio and spectral resolution compared with the monochromator system. However, according to extremely small bandwidths of the tuneable laser at the laser-based method, an oscillation pattern in the spectral responsivity can be observed. As the interference effect is not existent during any applications at blackbodies, a systematic deviation may be found for laser-based calibrations, if the oscillation pattern is not measured accurately. Therefore, in order to achieve the highest accuracy, the interference effect must be reduced as much as possible by suppressing the amplitude or eliminating the inter-reflection or should be measured with an extremely high wavelength resolution. However, in this work, the

measurement result in integral responsivity at the laser-based facility is in agreement with that at the monochromator-based set-up, within the combined uncertainty ($k = 2$).

From the result for the two LP3, it appears that modulation in the spectral responsivity due to the interference effect depends on the optical properties of the LP3. Since the interference effect is generated by inter-reflections between the planar optical surfaces within the interference filter of the LP3 and the amplitude of the oscillation depends on the reflectance of the surface, an improvement of the radiation thermometer's optics could reduce the amplitude of the interference effect, for example by using anti-reflection coatings at any lens's surface or adequate tilting of the relevant surfaces.

Based on a basic theory of the interference effect between air and medium in two layers, the interference can be described by [70]

$$m\lambda = 2nd\cos\theta\,, \tag{5.7}$$

where m is the order of interference, n is refractive index of the medium in the second layer, d is the thickness of the second layer and θ is the refractive angle in the second layer. That is a period of the oscillations in spectral responsivity depends on the wedged angle and the thickness of the interference filter. Therefore an improvement of the radiation thermometer design could probably reduce the period of the oscillation for example by using wedged interference filters. An investigation on this assumption must be performed in tight cooperation with the manufacture to find out the optimum design of next generation of radiation thermometers.

To check the accuracy of the absolute calibrations, the LP3 8005 was used to measure the PTB primary fixed-point blackbody as will be described in the next chapter.

6 Thermodynamic temperature determinations of the gold and copper freezing points

6.1 Introduction

Above 961.78 °C temperature can be realized using Planck's law and a silver, gold, or copper fixed-point and its assigned "thermodynamic" temperatures as reference radiation sources following the International Temperature Scale of 1990 (ITS-90). As the assigned values have been applied for the scale realization for more than 20 years now, it is currently time to check and carefully review these values. During the 24th meeting of the CCT in 2008, the working group 4 reported that the best estimated T-T_{90} values averaged from all previous determinations at the gold and copper points are 39.9 mK and 52.1 mK, respectively [71], with an uncertainty of 20 mK (k = 1). However, the thermodynamic temperatures of these fixed-points used for the averaging, directly measured by absolute radiation thermometry at NPL [72] and BIPM [73] using filter radiometers and at NIST using absolute radiation thermometer [74], deviate significantly from each others, excluding the recently indirect determinations at INRIM in Ref. 75 and 76 by extrapolation method using fixed-point blackbodies with lower temperature and their update T-T_{90} values in Ref. 70.

In detail, for the gold fixed-point, $T - T_{90}$ values by NPL and NIST are -0.029 K $\pm$ 0.049 K and 0.014 K $\pm$ 0.065 K respectively, while the $T - T_{90}$ value determined by INRIM is 0.065 K $\pm$ 0.023 K. For the copper point, a $T - T_{90}$ value of 0.148 K $\pm$ 0.090 K is given by BIPM in Ref. 73, which deviates significantly from the expected value, while a corresponding value determined by INRIM in Ref. 76 is 0.070 K $\pm$ 0.047 K. However, up to now, only some of the thermodynamic temperature determinations at the gold and copper fixed points were performed using absolutely calibrated radiometers. Therefore, more direct measurements of the thermodynamic radiance temperature by means of absolute radiometry are required especially at the copper point.

At the PTB, a series of filter radiometers (FRs) have been used to measure T-T_{90} values in combination with a large aperture blackbody (LABB) and standard platinum resistance thermometers (SPRTs) [78]. However, for fixed-point blackbodies with a radiating area of around 3 mm in diameter, measurements using the FRs become difficult due to diffraction errors, occurring at the precision apertures. Radiation thermometers can cope with smaller blackbody apertures due to target areas of about e.g. 1 mm in diameter at a distance of 700 mm for a LP3-type radiation thermometer. Therefore, using an absolutely calibrated radiation thermometer, thermodynamic temperatures of small aperture fixed-point blackbodies could be determined with lowest uncertainties. Moreover, in typical furnaces, small aperture fixed-point blackbodies will take advantage of the limited temperature uniformity inside the furnace.

In this chapter, the thermodynamic temperature of the gold and copper freezing points was determined using the LP3 radiation thermometer calibrated absolutely at the monochromator-based set-up and also at the laser-based facility described in chapter 5. A comparison of the determined T-T_{90} values with the best estimated values given in Ref. 71 will be used to validate the calibration procedure. In case the estimated thermodynamic temperatures are consistent with the assigned values of the ITS-90 and the other determinations, the absolutely calibrated LP3 will then be further applied to determine the thermodynamic temperatures of high temperature fixed-points in the next chapter.

6.2 Thermodynamic temperature determination of a blackbody

Based on the results of the absolute calibration given in the last chapter, the calculated photocurrents at any thermodynamic temperature of an ideal blackbody can be directly determined from the integration of the absolutely calibrated radiance responsivity multiplied by Planck's function according

$$I_{\mathrm{ph}}(T) = \int s_L(\lambda) L_{\lambda,s}(\lambda, T) d\lambda \,, \tag{6.1}$$

where I_{ph} is the calculated photocurrent, $s_L(\lambda)$ is the absolute spectral radiance responsivity of the radiation thermometer, and $L_{\lambda,s}(\lambda,T)$ is the spectral radiance given by Planck's law at any temperature. Since a finite solution for the thermodynamic temperature T of the above equation is complicated and time consuming, a curve of the photocurrents to blackbody temperature in the desired range is calculated and then fitted with Planck's version of the Jung-Verch equation [79] or Sakuma-Hattori equation [80] to directly calculate thermodynamic temperatures of the blackbody by

$$I_{\mathrm{ph}}(T) = C \frac{1}{\exp(\dfrac{c_2}{AT + B}) - 1} \,, \tag{6.2}$$

where A, B, C are fitting coefficients obtained by numerical methods with the software DATAFIT. Although the temperature dependent coefficients are used, the estimated thermodynamic temperatures from the Eq. 6.2 are still the thermodynamic temperatures since they are derived from Planck's law. Moreover, the interpolation errors obtained by the above equation are less than 10 mK, which are no significant contributions to the overall uncertainty [81].

All fitting coefficients obtained from the monochromator-based and laser-based method are shown in Table 6.1.

Table 6.1 Summary of the fitting coefficients for the LP3 8005

Fitting coefficient	Monochromator-based method	Laser-based method
A	6.51081×10^{-7}	6.51072×10^{-7}
B	4.45744×10^{-7}	3.67035×10^{-7}
C	9.56769×10^{-4}	9.55884×10^{-4}

However, in order to achieve results with the best accuracy, the size of source effect and the non-linearity of the radiation thermometer have to be evaluated to correct the measured photocurrents at the fixed-point temperatures.

6.2.1 Non-linearity

Since the absolute spectral calibrations are performed at a lower photocurrent level than that at the fixed-point measurements, a correction due to the non-linearity of the LP3 is required for thermodynamic temperature determinations, especially in the high temperature range. The non-linearity measurement of the LP3 was separately performed by using the radiance doubling technique in combination with 2 high power LEDs, emitting in the wavelength range from 600 nm to 660 nm as illustrated in **Fig.** 6.1 [82].

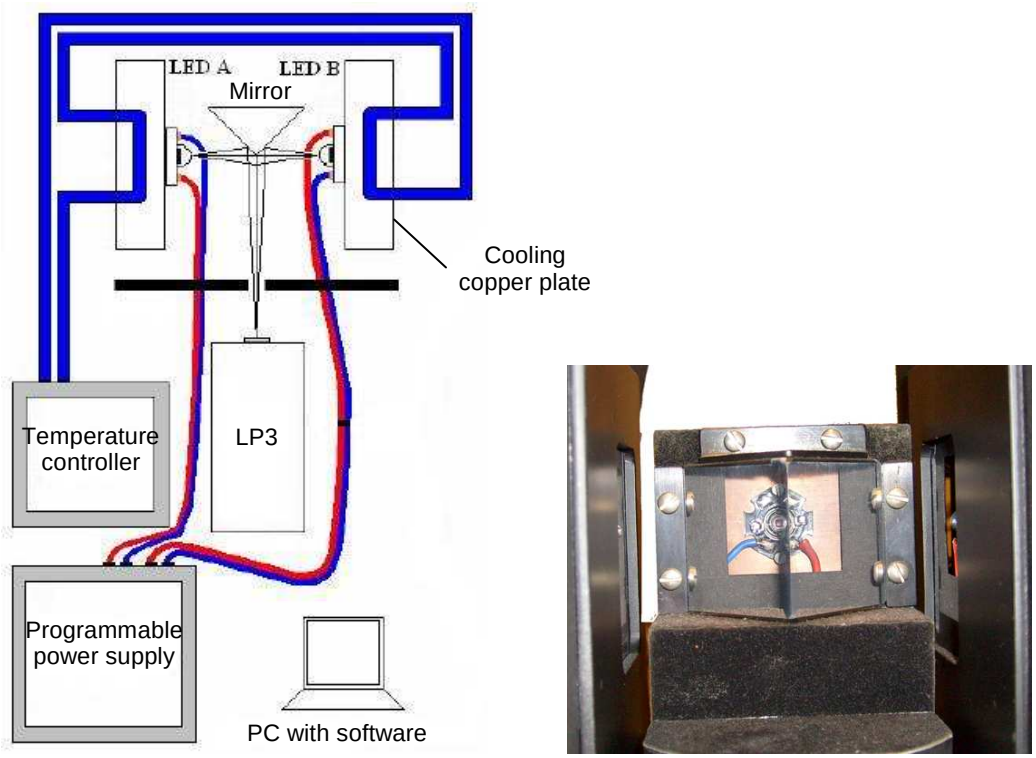

Figure 6.1 Measurement set-up for non-linearity of the LP3.

The measurement principle is based on an assumption that the LP3's photocurrent should be doubled in case the LED's radiance is doubled. In this measurement, the doubling of radiance can be done using two identical LEDs and a prismatic mirror to reflect the half view of radiation from the two LEDs direct to the LP3. The non-linearity of the LP3 can be arithmetically calculated by the following equation

$$\eta(I_{A+B}) = 1 - \frac{(I_A - I_d) + (I_B - I_d)}{(I_{A+B} - I_d)}, \tag{6.3}$$

where I_A and I_B are the photocurrents obtained from the LP3 when the diode A or B is switched on, I_{A+B} is the photocurrent when both diodes A and B are switched on, while I_d is the dark photocurrent, i.e. when both diodes are switched off.

A recent result of this measurement, covering the measuring range for an LP3 (No. 8013), is shown in **Fig.** 6.2, in comparison to the previous results in Ref. 69. At photocurrents above 2 x 10^{-11}A, the non-linearity was nearly zero with a relative uncertainty of less than 10^{-4}, while a significant non-linearity was found at low level photocurrents from 1 x 10^{-13} A to 1 x 10^{-11} A with an increasing uncertainty due to noise at lower photocurrent levels. Therefore, a correction of the spectral responsivity of the LP3 may be required, because the LP3 photocurrent at the monochromator-based facility was less than 2 x 10^{-12} A while the photocurrent at the measured fixed points is above 2 x 10^{-11}A. However the same correction was not required for the absolute results on the laser-based facility since the photocurrents during the calibration was in the linear region (1 x 10^{-11} A to 1 x 10^{-8} A) i.e. a non-linearity <10^{-4}.

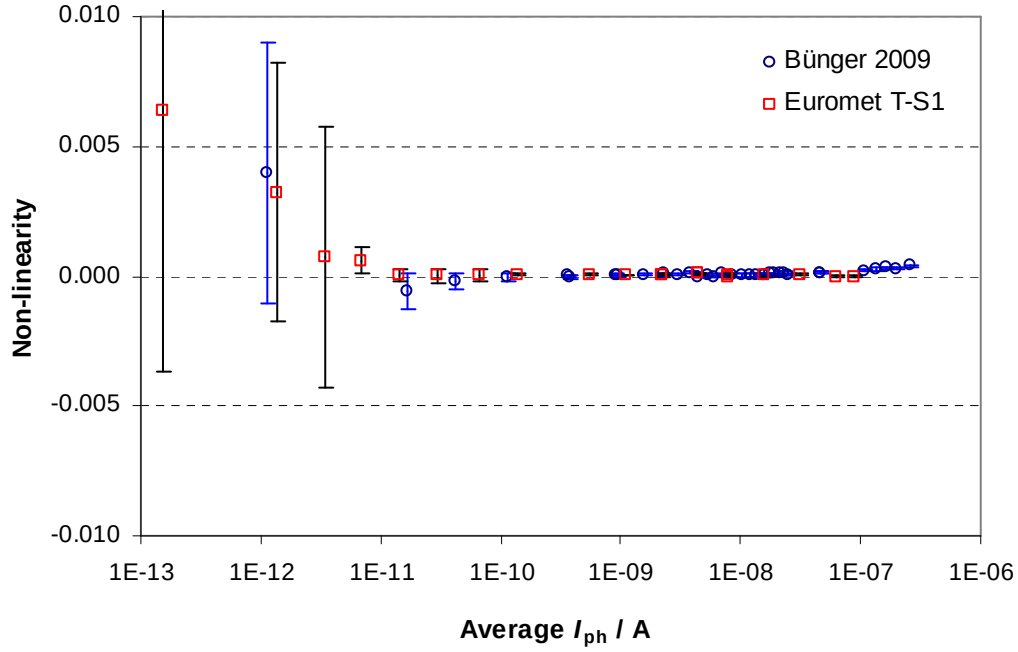

Figure 6.2 Non-linearity of the radiation thermometer LP3 obtained by the method in Ref. 82.

Applying the theory outlined in Ref. 83, the following correction has to be applied to the responsivity when the LP3 will be in use:

$$S(I_{\text{use}}) = S(I_{\text{cal}}) / \prod_{k=1}^{n} [\eta\,(I_{\text{cal}}\,2^{k})], \tag{6.4}$$

where n is a doubling number approximated by using $I_{\text{use}} = I_{\text{cal}}\,2^{n}$ and k is an index. The uncertainty due to the correction is defined by the multiple between the non-linearity uncertainty and the square root of the doubling number.

Since the measurement uncertainties at the photocurrent below 3 x 10^{-12} A were too large, any correction using Eq. 6.4 may contribute large errors to the estimated thermodynamic temperature at fixed-points. Hence the correction due to non-linearity of the LP3 radiation thermometer was not applied for the photocurrents at fixed-points. However, the correction can be accurately estimated with the photocurrents down to 6 x 10^{-11}A and the relative uncertainty of 0.04 % will be taken to be account for an uncertainty at gold and copper fixed-point measurements using the absolutely calibrated LP3 (No. 8005).

6.2.2 Size of source effect (SSE)

Since the radiating sources used during the absolute calibration and the temperature measurement are different both, in size and spatial uniformity, the SSE of the radiation thermometer LP3 is required to correct the measured photocurrents at the fixed-point. In this study the SSE was characterized using an indirect method by measuring the scattered radiation obtained from an uniform diffuse, source such as an integrating sphere, while the field of view of the radiation thermometer (a circle of ~0.9 mm in diameter at a distance of 700 mm) is blocked by a 3 mm black spot, and measuring the direct radiation without the black spot at different sized apertures. A photograph of the integrating sphere used in this work is given in **Fig**. 6.3.

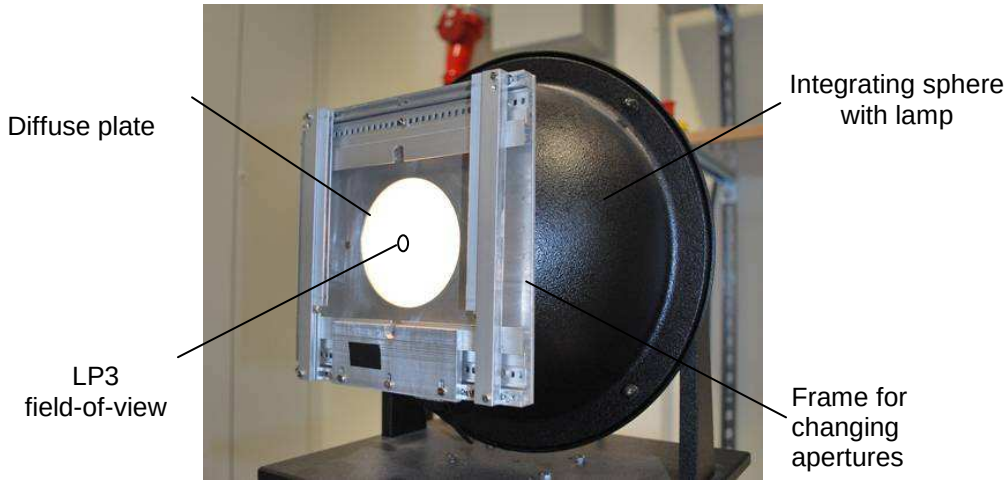

Figure 6.3 Photograph of the integrating sphere applied for the size of source effect measurement.

The SSE for a given aperture diameter can be basically determined from the ratio of the measured signals using

$$SSE(d,d_0) = \frac{I(L,d) - I(L,d_0)}{I(L)}, \tag{6.5}$$

where d is the diameter of the source, d_0 is the black spot diameter, $I(L,d)$ is the measured photocurrent with the black spot at the diameter of d, $I(L,d_0)$ is the measured photocurrent with the black spot at the diameter of d_0, and $I(L)$ is the measured photocurrent with the black spot removed. In both cases the dark current has to be subtracted. A measurement result for the test LP3 is presented in **Fig.** 6.4.

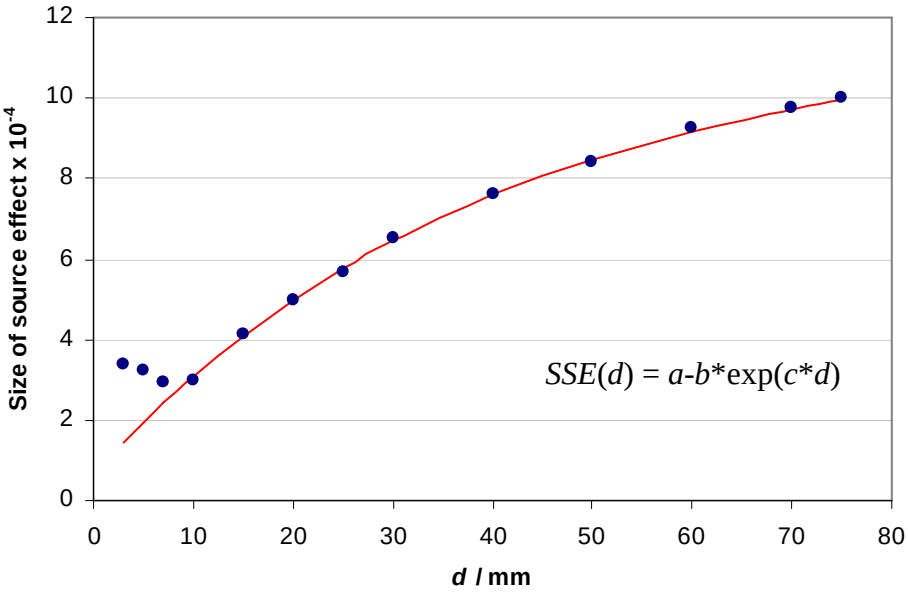

Figure 6.4 Size of source effect of the LP3 8005 expressed using Eq. 6.5

It can be seen that the SSE of the LP3 8005 is minimized with the aperture diameter of 7 mm and slightly increased with smaller diameters. This is probably due to the diffraction caused by the black spot. The correction in sphere intensity due to the change in aperture radius is accounted for by normalizing the measured signal to the maximum signal without the black spot at the relevant diameter or using a monitor diode. Since a correction for the diffraction is quite complicate, a curve fitting algorithm is applied to calculate the SSE for the aperture size smaller than 10 mm.

The SSE correction can be determined using the radiance distribution of the source such as the blackbody furnaces or fixed-points. Due to the relative small target size of the LP3, scans of the fixed-point opening can be done at a constant temperature or during the freezing plateau. If the spatial radiance distribution of the source is assumed to be radially symmetric then the detected signal will be corrected by the following equation

$$I(d) = \left[1 + \sum_i \frac{L(r_i) + L(r_{i-1})}{2L_0} \cdot \left(SSE(r_i, r_0) - SSE(r_{i-1}, r_0)\right)\right] I(d_0)\ , \tag{6.6}$$

where $L(r_i) = L(r_i)/L_0$ is the measured relative radiance distribution at radius, r. Since the diameter of the radiating area in the absolute calibration is approximately 5 mm, a simple correction for SSE should be applied toward a reference diameter; 3 mm (or neglected if a difference of SSE at two diameters is less than 10^{-5}) before any measurements. In addition, it will be more convenient if the effective radiating area in the temperature measurement at the fixed point is the same with that in the calibration.

6.3 Measurement at the Au and Cu fixed points

In this measurement, the primary gold fixed-point blackbody of PTB was used to test the developed calibration scheme. All performances and details of this blackbody on differences in plateau shape and repeatability can be found in Ref. 84. The uncertainty in the temperature realization using this fixed-point blackbody is regarded to be 10 mK. The emissivity of the cavity has been calculated to be 0.999988 [85], assuming an emissivity of 0.81 for the crucible graphite. A schematic diagram of the fixed-point crucible used in this measurement is given in **Fig**. 6.5.

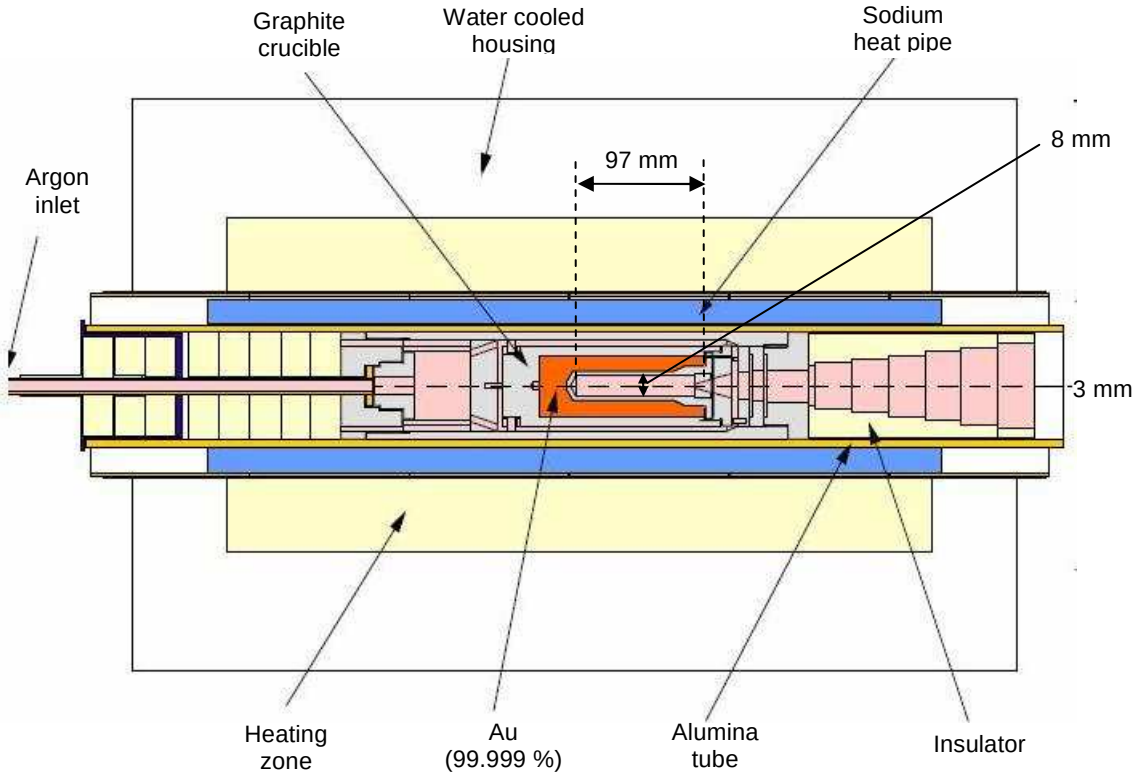

Figure 6.5 Schematic diagram of the PTB gold blackbody

For Cu point measurements, a small fixed-point cell manufactured by PTB was employed by operating it inside a Chino IR-R80 furnace. It is worth mentioning that the Cu point cell was not prepared for the purpose of this study but for comparison of small and large cell designs. More details of this blackbody on differences in plateau shape and repeatability can be found in Ref. 34. A design of the copper fixed-point crucible in this measurement is given in **Fig**. 6.6. The emissivity of the cell is calculated to be 0.9997 ($\pm$0.0003) using a Monte Carlo technique based on the geometry of the crucible cavity. The calculated emissivity for both cells was considered to correct the measured signals.

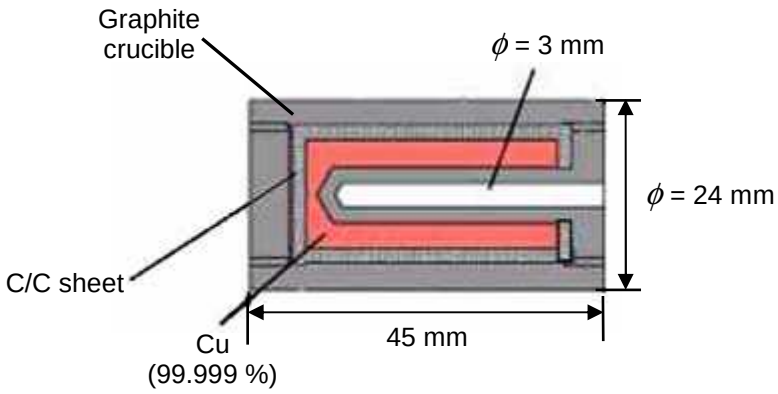

Figure 6.6 Design of the small copper fixed-point cell [34]

An illustration of the fixed-point operation inside the furnace to yield the melt and freeze is given in **Fig.** 6.7. To perform the melt, the furnace temperature is heated from below the melting temperature with an appropriate rate to above the melting temperature, then the metal inside the crucible starts to melt as the cell temperature remains stable for a short time period. In the similar way to perform the freeze, the furnace temperature is cooled down from above thee freezing temperature to below the freezing temperature. Since the performance of the melt is influenced by the prior freezing history, the melts are not considered as fixed-points for most metal fixed-point.

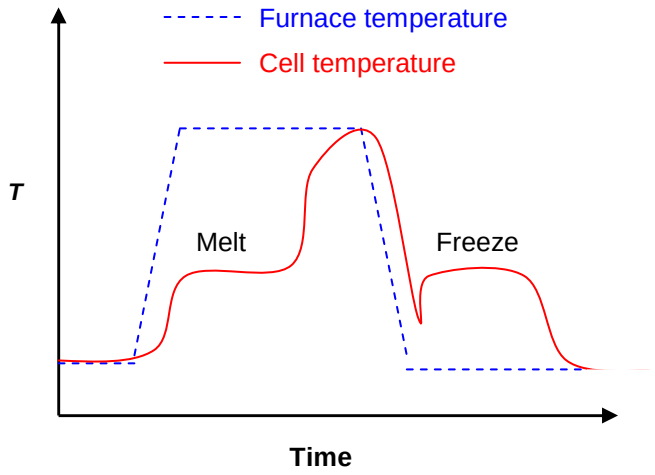

Figure 6.7 Illustration of the fixed-point operation inside the furnace.

To observe the photocurrents at the fixed-points, the calibrated LP3 was aligned collinear to the center of the cavity opening of the fixed-point cells and focused on the opening at a distance of 700 mm, which has its measurement spot size of 1.0 mm in diameter at the bottom of the cavity. To achieve the best quality of the plateaus, melts and freezes were performed by varying the furnace temperature in steps of $\pm$6 K for the Au fixed-point and $\pm$20 K for the Cu point, with respect to the corresponding temperatures defined by ITS-90.

During the freeze of the fixed-points, the plateau was stable within the relative standard deviation of 1.2×10^{-4} over a period of more than one hour for the gold blackbody and 6 minutes for the copper blackbody as shown in **Fig**. 6.8 and **Fig**. 6.9, respectively.

a)

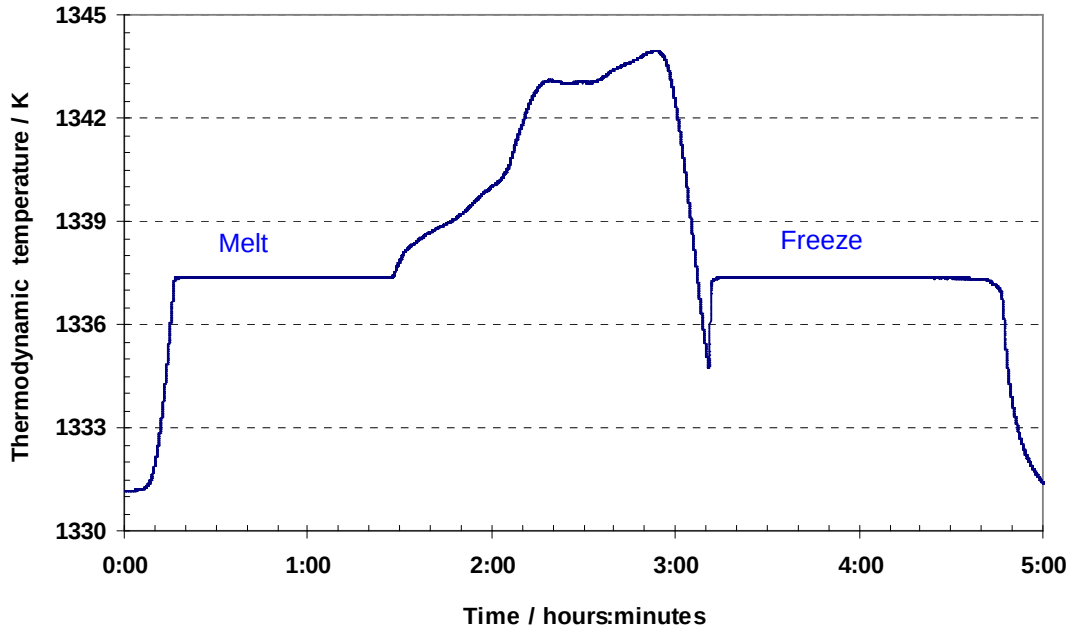

b)

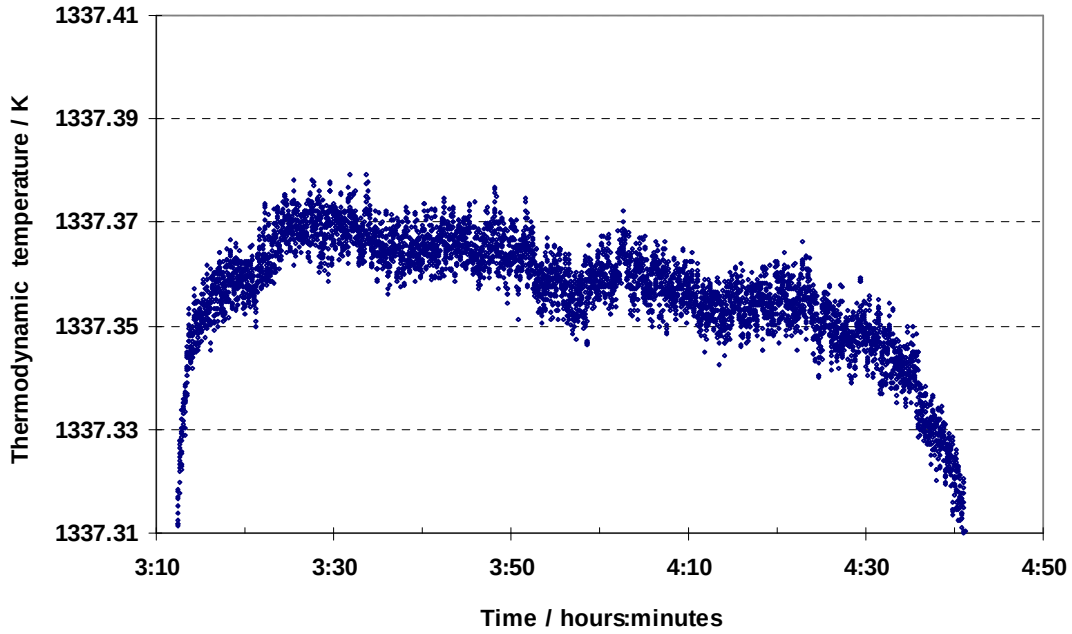

Figure 6.8 Plateau of the gold fixed-point blackbody measured by the absolutely calibrated LP3 a) Full curve and b) Zoom in freezing curve

a)

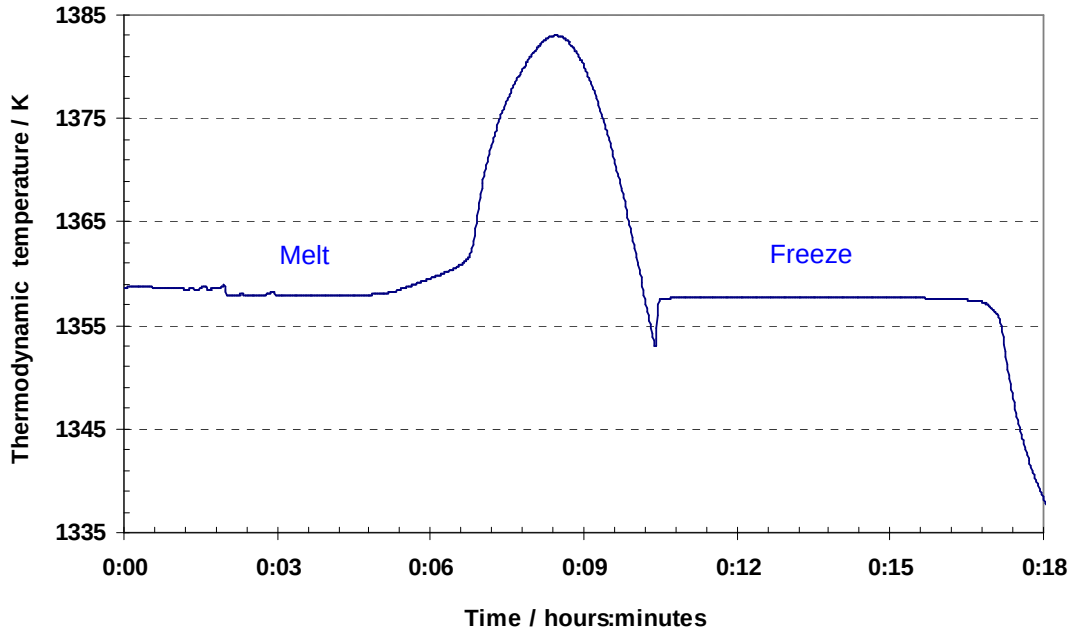

b)

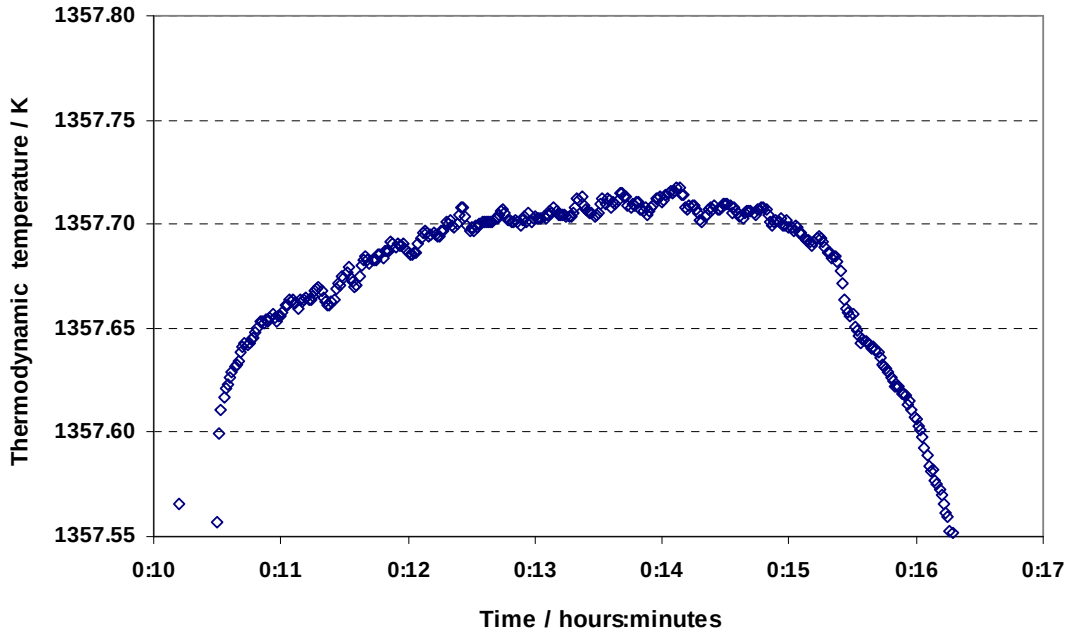

Figure 6.9 Plateau of the copper fixed-point blackbody measured by the absolutely calibrated LP3 a) Full curve and b) Zoom in freezing curve

As mentioned before, the freezing temperatures of the Au and Cu points will be used as fixed-point temperatures in the following. The photocurrents at the freezing temperatures can be estimated as the average between 25 % and 75 % solid fraction of the freeze plateau. For both cells, a difference between this average value and the maximum of the freezing curve was less than 1.6×10^{-4}, which is equivalent to 11 mK in terms of temperature.

Additionally, radiance profiles both in horizontal axis and vertical axis were taken as shown in **Fig**. 6.10 to approximate the radial profile for assessing the SSE correction as discussed in the Eq. 6.6. Since the plateau duration of the Cu blackbody was relative short, the radial profile for correction was obtained from the Chino furnace at the temperature around 1100 °C. All correction coefficients are shown in Table 6.2.

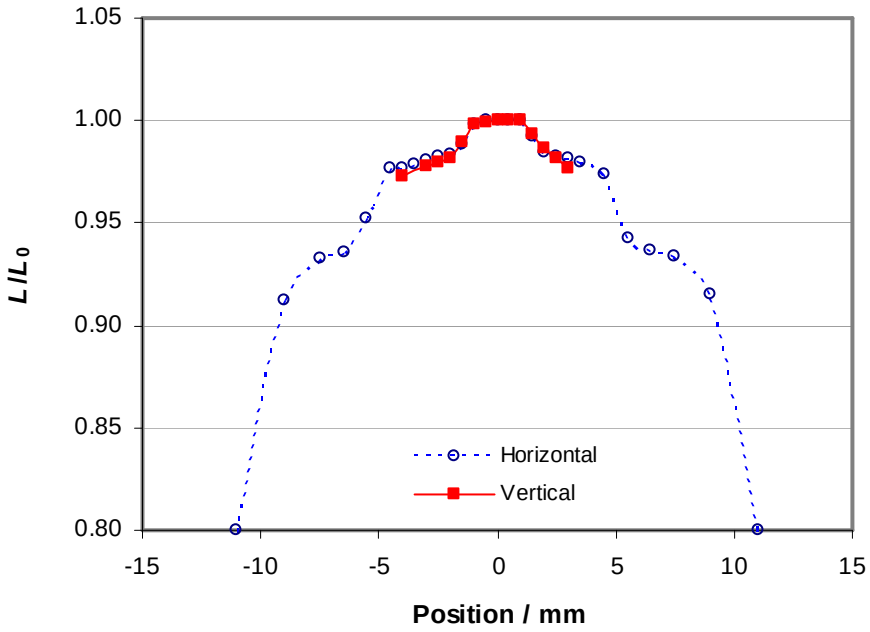

Figure 6.10 Radial profiles in horizontal axis and vertical axis for the gold blackbody

Table 6.2 Summary of the correction coefficients for the measurements at the two fixed-points using the LP3 8005.

Correction	Au (%)	Cu (%)
Emissivity	0.012	0.030
Size of source effect	0.026	0.020

6.4 Uncertainties of the fixed-point temperature determinations

With respect to the absolute calibration of the LP3, the uncertainty of thermodynamic temperature can be calculated from the radiance uncertainties associated to the radiation thermometer by using the derivative of Wien's approximation to Planck's radiation law resulting in the following equation

$$\Delta T = \frac{\lambda T^2}{c_2} \cdot \frac{\Delta L}{L} \ . \tag{6.7}$$

All corresponding uncertainties for thermodynamic temperature associated to the radiation thermometer are listed and converted to temperature uncertainty in Table 6.3.

In addition to the uncertainties of the radiation thermometer as described in previous sections, uncertainties associated to the fixed-point blackbody have to be combined in total uncertainty. The freezing temperature can be estimated as the average between 25 % and 75 % solid fraction of the freeze plateau and the difference between this average value and the maximum of the freezing curve is treated as the uncertainty due to plateau width. Additionally the uncertainty due to reproducibility of the freezing temperature for this fixed-point, evaluated by the standard deviation of four freezes, was better than 10 mK.

In order to evaluate the long term drift of the test LP3, the measurement at the gold fixed-point was repeated after 1 year. The long term drift was found to be 0.093 % per year and the corresponding uncertainty is also taken into account for determining the uncertainty. The total uncertainty within $k = 1$ of the thermodynamic temperature determination is 0.156 K and 0.165 K for the Au and Cu point, respectively.

Table 6.3 Summary of the relative uncertainty contributions of the thermodynamic temperature determination of the Au and Cu points

Contributions of uncertainty	Relative uncertainty (%)	
	Au	Cu
Spectral responsivity	0.17	0.17
Size of source effect	0.02	0.03
Non-linearity	0.04	0.04
LP3 short term stability	0.05	0.05
Plateau width	0.02	0.04
Reproducibility	0.02	0.04
Emissivity	0.03	0.03
LP3 long term stability	0.05	0.05
Total uncertainty, $k = 1$	0.19	0.20
Temperature uncertainty (K)	0.156	0.165

As can be seen in the Table 6.3, the main contribution to the uncertainty is contributed with the absolute calibration of the LP3. In contrast, the uncertainty due to the realization of the fixed-points is only 0.04 % and 0.06 %, equivalent to 30 mK and 50 mK at the gold point and the copper point, respectively. Therefore, the validation of the absolute calibration with these fixed-points is reasonable and the measurement results in terms of thermodynamic temperature are comparable to other determination as will be discussed in the next section.

6.5 Results and discussions

Summaries of the corrected photocurrents at the Au and Cu freezing temperatures measured by the LP3 under test are shown in Table 6.4, along with the calculated photocurrents. The obtained thermodynamic temperatures according to the spectral responsivity from the absolute calibration at the monochromator-based set-up are also shown in Table 6.5. Keep in mind that the corresponding results from the laser-based facility were given using the interpolation from the calibration results in the wavelength range between 535 nm to 618 nm.

Table 6.4 Summary of the measured and calculated photocurrents of the LP3 8005 at the fixed-point temperatures using the calibrated absolute spectral responsivity

Fixed point	Measured Photocurrent (A)	Calculated Photocurrent (A)		Relative Difference (%)	
		Monochromator	Laser-based	Monochromator	Laser-based
Au	6.430×10^{-11}	6.427×10^{-11}	6.410×10^{-11}	-0.05	-0.31
Cu	8.234×10^{-11}	8.240×10^{-11}	8.219×10^{-11}	0.07	-0.19

Table 6.5 Summary of the resulting thermodynamic temperatures along with the temperature uncertainty at the fixed-point temperatures using the fitting coefficients in Table 6.1

Fixed point	T_{90} (K)	Resulting T (K)	
		Monochromator	Laser-based
Au	1337.33	1337.365 ± 0.156	1337.580 ± 0.135
Cu	1357.77	1357.710 ± 0.165	1357.927 ± 0.145

Using these experimentally determined thermodynamic temperatures, the T-T_{90} value at the Au point is 35 mK and at the Cu point is -60 mK, which is well within the combined uncertainties ($k = 1$) of the values given in Ref. 71 for the results at the monochromator-based set-up. The T values obtained by the absolute calibration at the laser-based facility

differ slightly from the assigned values in the ITS-90, i.e. 250 mK and 157 mK at the Au point and the Cu point respectively but are still well within the expanded uncertainties (k = 2). To verify the observations for the fixed-points, the estimated T-T_{90} values are also compared to previous worldwide determinations as given in Table 6.6.

Table 6.6 Comparison of T-T_{90} value for the Au-and Cu point to previous determinations

Fixed point	T-T_{90} (K)				
	NPL [72]	BIPM [73]	NIST [74]	INRIM [75, 76]	This work
Au	−0.029 ± 0.049	-	0.014 ± 0.064	0.065 ± 0.023	0.035 ± 0.156
Cu	-	0.148 ± 0.090	-	0.070 ± 0.047	-0.060 ± 0.166

In comparison to the previous absolute radiometric measurements at NPL [72] using filter radiometers, the thermodynamic temperature of the Au point differs by 64 mK. However its T-T_{90} value appears to be in good agreement with the result of NIST [74] using an absolute pyrometer and the presently indirect measurement at INRIM in Ref. 75. With regard to the Cu point, the T-T_{90} value seems to be lower than the best estimated value and also the results by BIPM [73] and INRIM in Ref. 76, but still within the measurement uncertainty of the presented method.

All summarize of the T-T_{90} values from the Zn point to the Cu point is also graphically shown in **Fig.** 6.11, along with the recalculated values in Ref. 84.

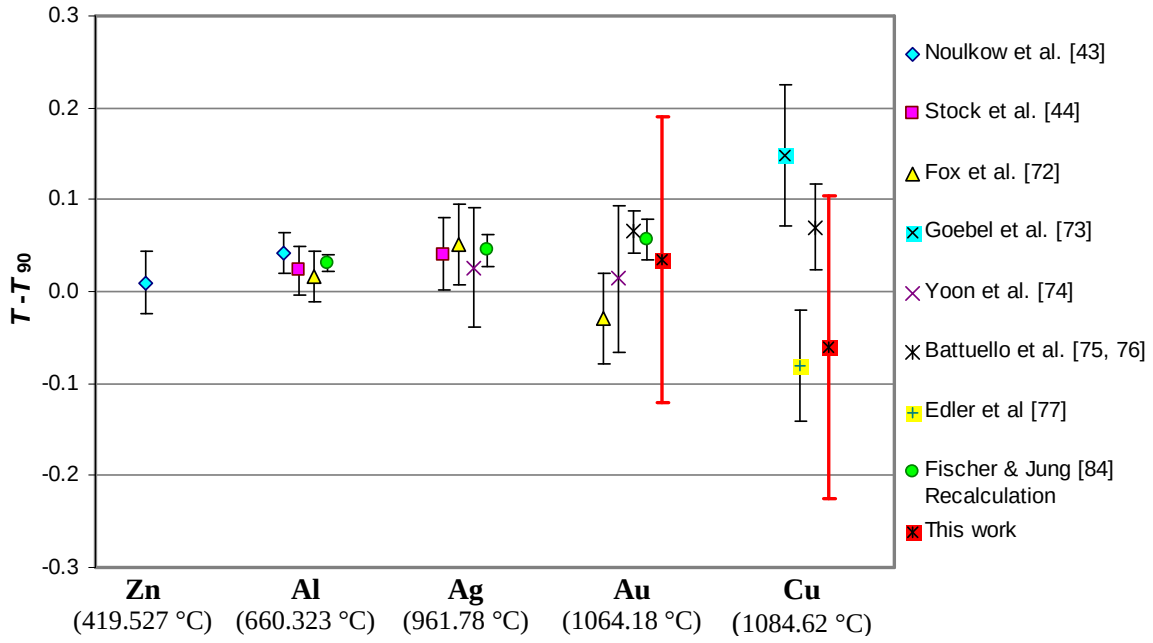

Figure 6.11 Comparison of the determined T-T_{90} values to previous worldwide determinations by means of radiometry from the Zn point to the Cu point.

One reason for the poor result at the Cu point is probably attributed to the impurity of the fixed-point material in the blackbody crucible due to its small cell design, whose original intention was to investigate plateau lengths and not thermodynamic temperature measurements. Therefore, a new Cu cell blackbody will be fabricated and applied in future to determine the thermodynamic temperature of the Cu point with higher accuracy.

However, from these validation results, it is now confirmed that the absolutely calibrated LP3 radiation thermometer has the potential to measure the thermodynamic phase-transition temperature of the small-aperture fixed-point blackbodies by using the calibration results at the monochromator-based facility. Therefore, the same LP3 was further applied to measure at high-temperature fixed-point blackbodies as can be seen in next chapter.

7 Thermodynamic temperature determinations of high-temperature fixed points

7.1 Introduction

The temperature accuracy at high temperatures can be improved by measuring the thermodynamic temperature of a blackbody directly with radiometrically calibrated radiation thermometers or filter radiometers. However, this primary method requires a full calibration facility as mentioned in Chapter 4. A more practical alternative is to establish high temperature fixed-points as routine metrological tools to calibrate radiation thermometers by interpolation similar to the low temperature range where the interpolation is done by contact thermometers, rather than by extrapolation as currently defined by the ITS-90. For this reason, metal carbon eutectic fixed-points have been developed for the application in the high temperature range up to 2500 °C and above [3, 86, 87]. Many types of metal carbon and metal carbon-carbide alloys have been used as fixed-point materials in graphite crucibles and their performance has been studied in terms of repeatability, reproducibility and also robustness [88, 89, 90, 91, 34]. Only M-C eutectic fixed-points with high performance may be used as reference sources for improving the ITS-90 at high temperatures (above 1000 °C). However, before implementing these fixed-points for this purpose, their thermodynamic phase-transition temperatures must be accurately ascribed by the Consultative Committee for Thermometry, Working Group 5 (CCT-WG5) from worldwide measurement results.

As part of the work package 4 (WP4) of the High-temperature fixed-point plan (HTFP) of the CCT-WG5, the thermodynamic temperatures of the melting points of cobalt-carbon (Co-C), platinum-carbon (Pt-C) and rhenium-carbon (Re-C) eutectic small fixed-point cells were recently determined at PTB using filter radiometers combined with a high-temperature blackbody and a radiation thermometer according to the comparison method described in [5]. It should be noted that an assessment of fixed-point quality in terms of long-term stability and robustness is only partly the purpose of this work.

During the process of radiance comparison according the method described in [5], the photocurrent at the melting point for each fixed-point was measured directly by the absolutely calibrated radiation thermometer LP3. With the calibrated spectral radiance responsivity of the radiation thermometer and Planck's radiation law, the thermodynamic temperature for each fixed-point can be determined directly from the measured radiance via the Jung-Verch or Sakuma-Hattori equation [79, 80]. One advantage of this direct method is to eliminate an influence from different field of views between the filter radiometers and the radiation thermometer due to the uniformity of the high-temperature blackbody [34].

Measurement results will be presented in terms of thermodynamic temperature for each material and compared with previous measurements on another set of fixed-point blackbodies. Finally measurement results will be compared to those from the indirect method using FRs on a same set of these fixed-points to evaluate the accuracy of this approach using the absolutely calibrated LP3.

7.2 Measurement procedure

In this study, a set of four cells from each of the material Co-C (~1324 °C), Pt-C (~1738 °C) and three cells from Re-C (~2474 °C) were measured using the absolutely calibrated LP3, therefore yielding the respective thermodynamic temperatures. These cells were carefully constructed using ultra high purity powder of graphite (99.9999 %) and metals (99.999 %) and also high purify graphite crucible and fully investigated in plateau shape by other NMIs, within the WP1 of the HTFP (NIM, NIST, CNAM) to ensure the performance of these cells. The design of these fixed-point crucibles is very similar to the design of the copper point cell presented in chapter 6, i.e. approximately 25 mm in diameter and 45 mm in length. These cells have a cavity with an aperture of 3 mm in diameter and a length of 33 mm. The effective emissivity of these fixed-point cells is 0.9997 ($\pm$0.0003), which is used to correct the measured photocurrent signals.

For the measurement set-up, the same Chino IR-80 furnace as used in the last section was applied in similar operation to heat up the fixed-point cells. To prevent contamination of the fixed point cells in the high-temperature range, the furnace was baked at 2000 °C under vacuum for at least three hours and, for Re-C, additionally above 2500 °C under Ar purge, before installing the fixed-point cells. Then the fixed-point cell wrapped in layers of carbon felt was installed inside the furnace as shown in **Fig.** 7.1.

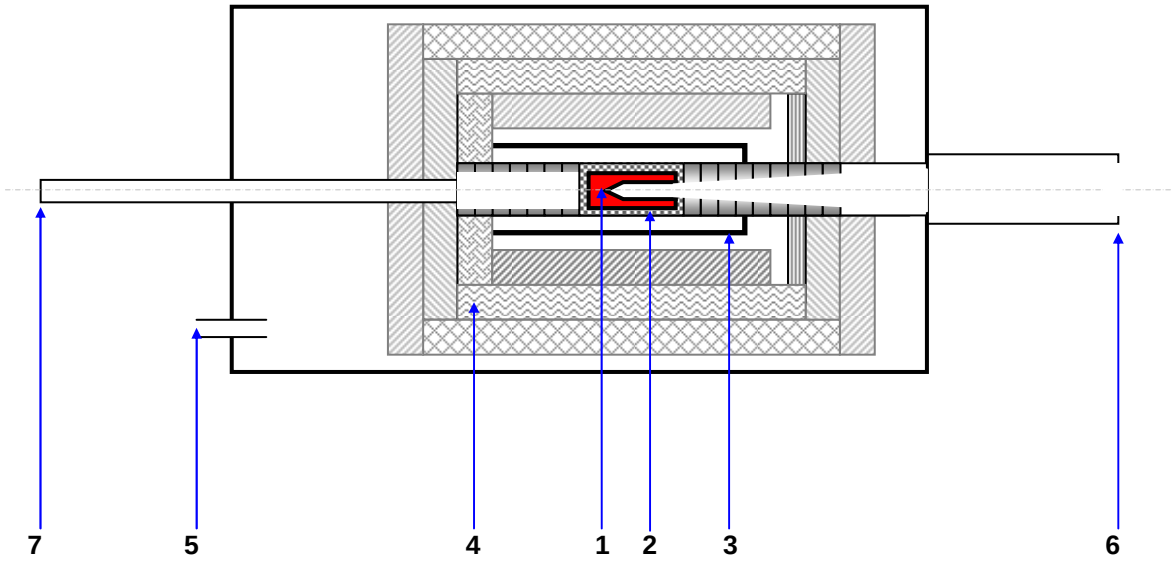

Figure 7.1 Schematic diagram of the Nagano furnace type M for eutectic fixed-points:
1) fixed-point cell, 2) C/C working tube, 3) C/C heating element, 4) graphite insulator,
5) purge gas inlet, 6) front opening for measuring,
7) rear quartz window for controlling.

To achieve the best plateau shape for each fixed-point, the LP3 was carefully aligned to the center of the cavity opening of the fixed-point cells at a distance of 700 mm. By use of a precision linear stage, horizontal scans across the opening can be done during the melts. For each cell, the measurements were repeated to check the effect of removing and installing cells on the observed melting temperature.

The measurements were carried out from lowest temperature to highest temperature to reduce possible thermal drifts during the measurements. For the Co-C and the Pt-C cells, melts and freezes were performed by varying the furnace temperature with temperature steps of $\pm$10 K and $\pm$20 K with respect to the nominal temperature, while larger temperature steps were performed ($\pm$20 K and $\pm$30 K) for the Re-C fixed-points to ensure that the crucible undergoes the phase-transition.

7.3 Measurement results

Firstly, typical plateau curves are given to show the melting range for each material and the estimation of inflection point from the melting curve will be described. Finally, the estimated photocurrents at the melting point are used to calculate the thermodynamic temperatures with the measurement uncertainties for each material.

7.3.1 Plateau observation

Typical plateaus of individual melt/ freeze profile for each material are given in **Fig.** 7.2, along with an approximation of their melting ranges.

a) Co-C at the approximate thermodynamic temperature of 1597 K

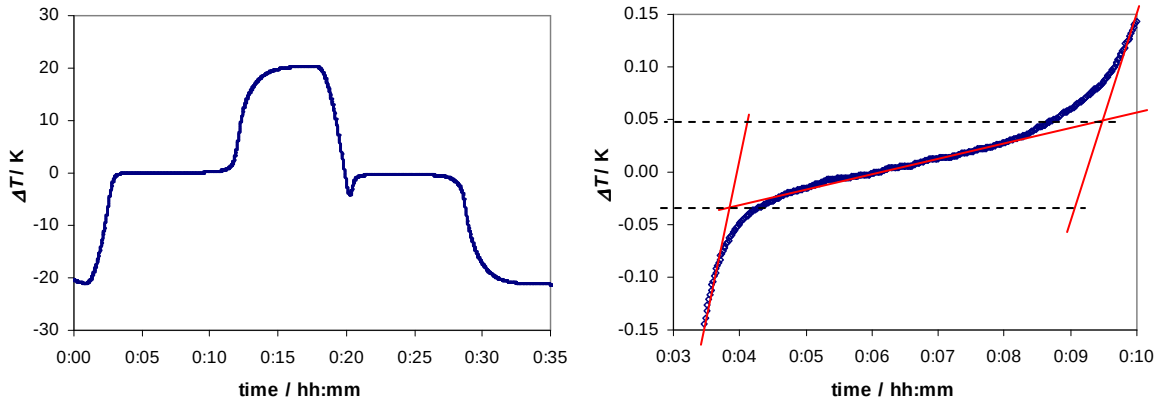

b) Pt-C at the approximate thermodynamic temperature of 2012 K

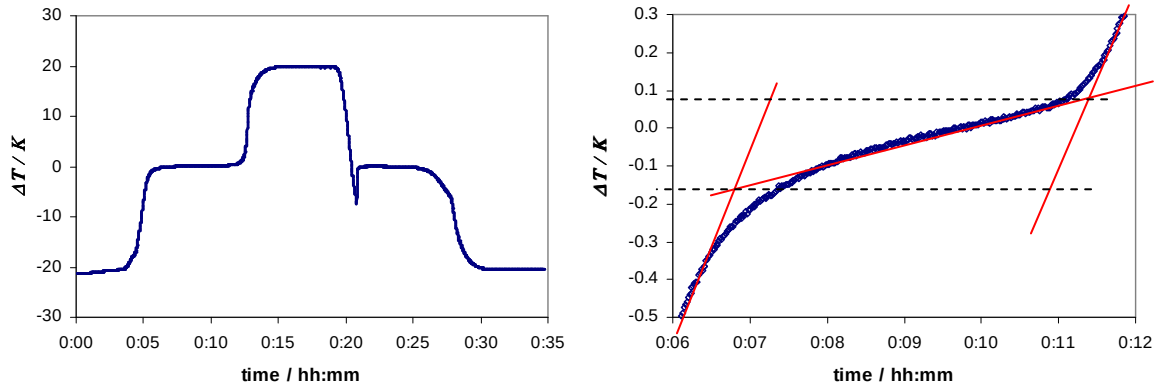

c) Re-C at the approximate thermodynamic temperature of 2748 K

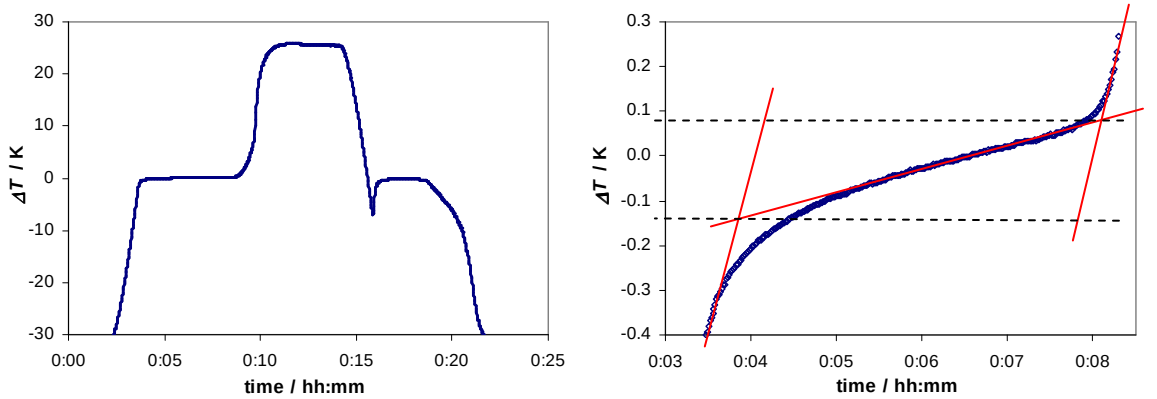

Figure 7.2 Typical melting and freezing plateaus for one of the Co-C, Pt-C and Re-C fixed-point cells, along with their melting ranges.

It can be seen that for Co-C a melting range of 0.10 °C, and a melting range of 0.25 °C was observed for the Pt-C and the Re-C. In addition, the melt durations are longer than 7 minutes, 6 minutes and 5 minutes for Co-C, Re-C and Re-C, respectively. Note is that comparisons between the same fixed-point material cells are not discussed in this work.

7.3.2 Estimation of thermodynamic phase-transition temperatures

It is well known and reconfirmed by this experimental result that the melt obtained from the eutectic fixed-points provides better reproducibility than the respective freeze. Thus the thermodynamic phase-transition temperature of these fixed points will be determined in preference by using the melting curves. Since the melt for the eutectics has never been as flat as that of the pure metal fixed-points, the melting point is defined as the inflection point, i.e. the minimum point of the first derivative of temperature with respect to time or the zero point of the second derivative of temperature with respect to time. In practice, the melt signal was averaged over an optimized duration to further calculate the second derivative so that achieving a smoothed result as shows in **Fig.** 7.3.

Varying this procedure was helpful for determining a source of uncertainty due to an identification of the inflection point. The photocurrent obtained by the LP3 at the inflection point in **Fig.** 7.3 has been further applied to calculate the thermodynamic temperature with the calibration coefficients obtained in chapter 6.

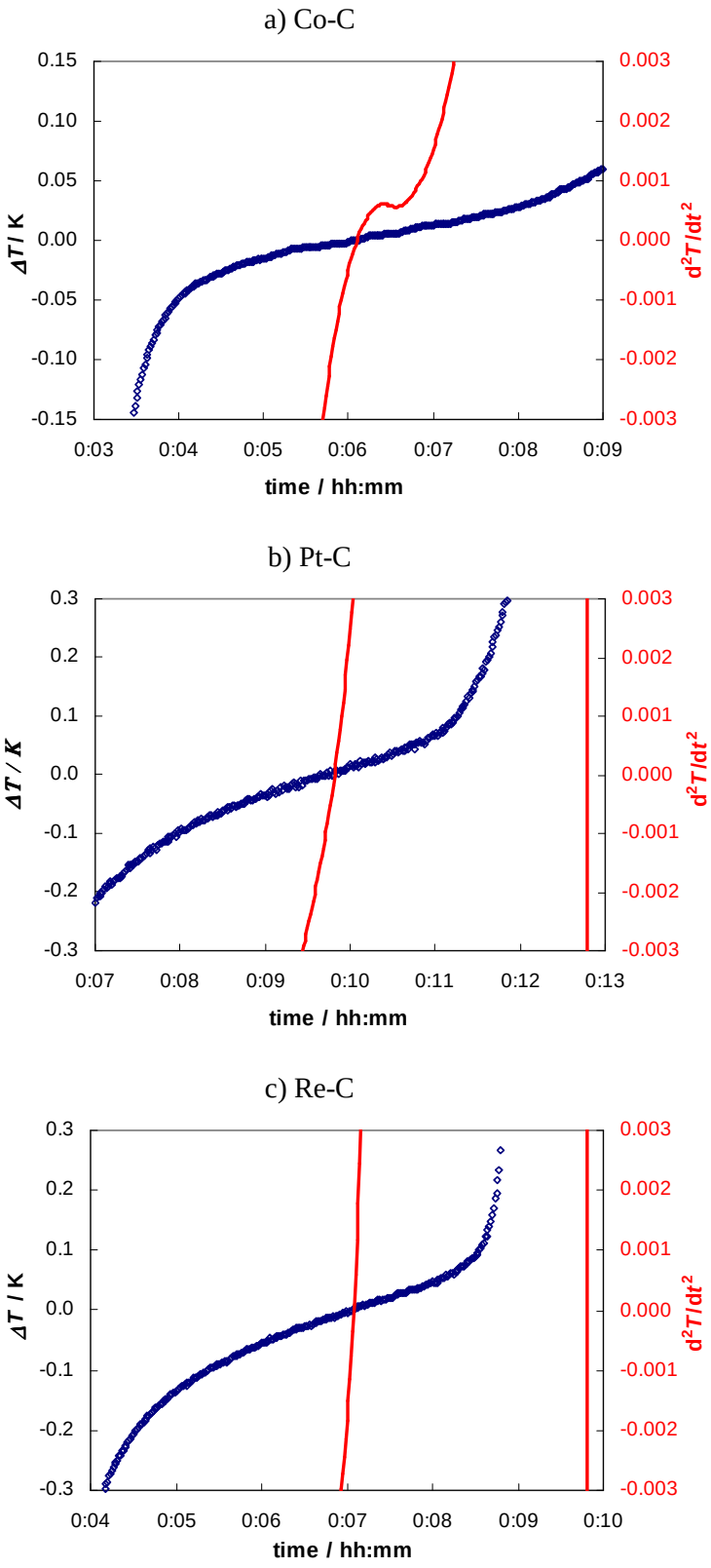

Figure 7.3 Typical inflection points on the melting plateaus for Co-C, Pt-C and Re-C

Similarly to the measurements at the gold and copper fixed-points, the corrections due to the blackbody emissivity and the size of source effect present for each cell were applied before calculating the thermodynamic temperature. It is worth noting that the furnace contribution to the spectral emissivity of the cavity is assumed to be eliminated for high temperature fixed-points with an aperture diameter of 3.0 mm as can be found in Ref. 92. The difference in the resulting temperature between two typical temperature profiles along this type of furnace is only 1.5 mK for a small opening Re-C cell. For the corrections of the size of source effect, typical horizontal profiles at the fixed-point temperatures are shown in comparison to the integrating sphere in **Fig.** 7.4

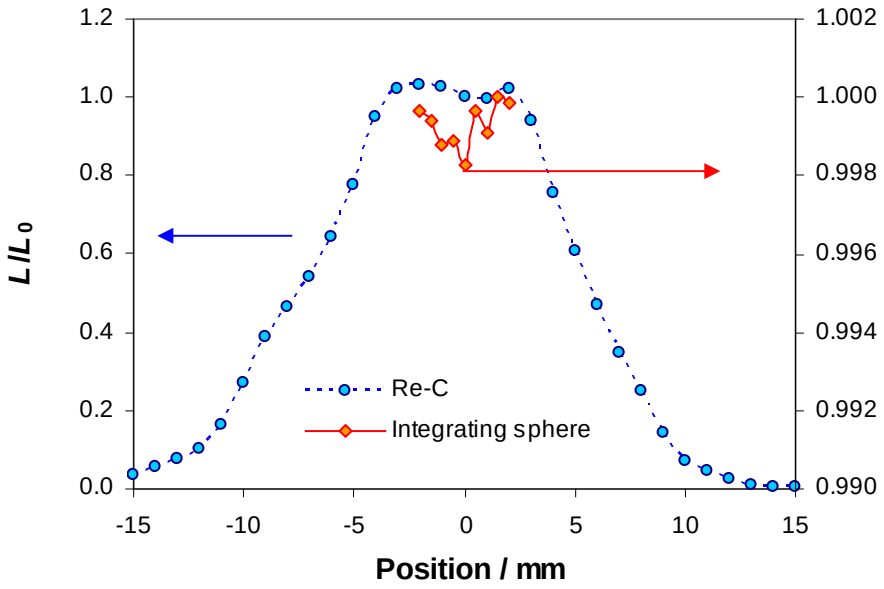

Figure 7.4 Radiance horizontal profiles across the Chino furnace opening at the Re-C temperature

In addition, an effect from the temperature drop at the cavity bottom due to radiative transfer was also considered for high temperature fixed-point cells by neglecting the radiant exchange between the furnace and the cavity [84] as follows

$$\Delta T = \cos\theta \cdot \varepsilon \cdot \sigma \cdot T^4 \cdot \frac{d}{k} \cdot \left(\frac{r}{l}\right)^2 . \qquad (7.1)$$

Where θ is the angle of the tilted bottom, ε is the graphite emissivity, σ is the Stefan-Boltzmann constant, d is the cavity thickness, k is the thermal conductivity of graphite, r is the aperture radius and l is the cavity length. All estimated corrections at each fixed-point temperature are given in Table 7.1

Table 7.1 Summary of the corrections for the measurements at the eutectic fixed-points using the LP3.

Correction	Co-C	Pt-C	Re-C
Emissivity, %	0.003	0.003	0.003
Size of source effect, %	0.013	0.016	0.018
Temperature drop, mK	0.018	0.046	0.159

By using the derivative of Wien's law, the estimated size of source effect contributes to only 15 mK, 26 mK and 51 mK for Co-C, Pt-C and Re-C, respectively. For sound measurement results, the effect is still considered as a component of uncertainty originating from the uncertainty of the size of source effect measurement and the horizontal scan.

It was found that the correction from Eq. 7.1 due to the temperature drop at Re-C point seems to be relatively significant to the measurement results. In comparison to simulation results considering also the radiant exchange between the furnace and the cavity in Ref. 93 and 94, smaller differences were found lying within 5 mK and 10 mK, respectively. However, for a better modeling of the real situation a more transient modeling, for instance in Ref. 94, including all components and also the furnace uniformity, should be performed to obtain the best estimation for corrections of the thermodynamic temperature, especially at the melting point.

7.3.3 Uncertainty budget

Likewise the determination of thermodynamic temperatures at the Au and Cu points, all contributions of uncertainty associated with the LP3 and the eutectic fixed-points were considered in the following.

- The uncertainty associated to the absolute spectral responsivity calibration of the LP3 with the standard uncertainty of 0.17 % (k = 1) (see Table 5.1).

- The uncertainty due to the size-of-source corrections for each cell, estimating from an approximation value of 0.03 %, including an uncertainty both in isothermal case and non-isothermal case.

- The uncertainty due to thermal stability of the LP3 at each fixed-point temperatures, estimated from the initial and final measurements.

- The uncertainty associated to the non-linearity of the LP3, as described in chapter 6 with the relative uncertainty of 0.02 %.

- The uncertainty in determining the point of inflection during the melt, obtained by varying the number of the measuring data for each melting curve, as described in 7.3.2.

- The repeatability of a single cell, defined by the standard deviation of three or four inflection point measurements in one day. For Co-C and Pt-C cells, standard deviations are within 30 mK, while better than 61 mK for Re-C cells.

- The uncertainty due to the calculation of emissivity of the eutectic cells by means of Monte Carlo method only for the case of an isothermal cavity.

- Finally the uncertainty associated to the long-term stability of the LP3. Since it is impossible to separate the long term drift of the LP3 from the reproducibility of the absolute calibration in Chapter 5, a difference in absolute responsivity before and after the measurements at eutectic fixed-points of 0.069 % was taken into account.

All contributions to the uncertainty were transformed to temperatures at the corresponding fixed-point temperatures and combined as shown in Table 7.2.

Table 7.2 Summary of the uncertainty contributions to the thermodynamic temperature determinations of the eutectic points

Contributions of uncertainty	Temperature uncertainty (K)		
	Co-C	Pt-C	Re-C
Spectral radiance responsivity	0.195	0.310	0.578
Size of source effect	0.035	0.055	0.102
Non-linearity	0.023	0.037	0.068
LP3 short term stability	0.053	0.053	0.105
Identification of inflection point	0.050	0.050	0.050
Repeatability	0.006	0.031	0.061
Emissivity	0.035	0.055	0.102
LP3 long term stability, u_r=0.069 %	0.079	0.126	0.234
Standard uncertainty, k = 1	0.229	0.354	0.657
Expanded uncertainty, k = 2	0.46	0.71	1.31

At this stage, the two main components limiting a higher accuracy of the measurements are the uncertainty of the absolute calibration at the monochromator-based set-up and the long term stability of the LP3. For the first one, even with the best measurement uncertainty of 0.14 % at the laser-based facility, the uncertainty component is still larger than 400 mK at Re-C temperature, a factor of two from the target value of 200 mK (k = 1). For the last component, although the thermal stability of the LP3 has been already improved at high temperatures by optimizing an optical design of a glass filter and an interference filter

within the LP3 [95], the long term drift probably influences the measurement results. Indeed, the long term stability of the LP3 was found to be 0.098 % per year, obtained by a repeat of the measurement at the Au point in Chapter 6.

7.3.4 Thermodynamic temperature

Average thermodynamic temperatures at the inflection point measured by the absolutely calibrated LP3 for each eutectic alloy are given in Table 7.3 along with reproducibility between cells from the different sources and their absolute uncertainty in thermodynamic temperature. It should be noted that these values were not corrected by the temperature drop described in section 7.3.2. until more accurate transient models for the temperature drop are available.

Table 7.3 Summary of average thermodynamic temperature of the melting points for each eutectic.

Eutectic	Co-C	Pt-C	Re-C
Average temperature, K	1597.465	2011.648	2748.224
Reproducibility, K	0.064	0.105	0.149
u (k = 1), K	0.229	0.354	0.657

Although the reproducibility of these eutectic fixed-points has not yet reached the target of better than 50 mK for Co-C and Pt-C, and 100 mK for Re-C, recommended by the CCT-WG5, it is significantly less than the standard uncertainty of the measurements. The results on the estimated thermodynamic temperatures are further discussed in the following.

7.4 Comparison to other determinations

7.4.1 Comparison to previous determinations on different cells

The average thermodynamic phase-transition temperatures in Table 7.3 were compared to previous determinations on a different set of fixed-point cells at PTB [5] and NIST [96], given in Table 7.4 along with the measurement uncertainty values (k = 2).

For Co-C, the average phase-transition temperature of fixed-point cells manufactured by different NMIs (NPL, NMIJ, LNE-INM/CNAM) was indirectly determined at PTB by filter radiometers and was found to be 1597.11 K $\pm$ 0.23 K, 1597.25 K $\pm$ 0.22 K and 1597.18 K $\pm$ 0.21 K respectively. In addition, the thermodynamic melting temperature of the same NPL cells measured at NIST using an absolute pyrometer 1 (AP1) and a Thermo Gauge furnace was found to be 1597.43 K $\pm$0.17 K. The recently determinate value by the extrapolation method at INRIM on its own Co-C cell was 1597.27 K $\pm$ 0.17 K [97]. It is clear that the average thermodynamic temperature for Co-C in this work is consistent with

the NIST and the INRIM results, but slightly deviates from that measured by PTB using filter radiometers, although being within the combined uncertainty.

For Pt-C, the measurement results at PTB were 2011.67 K ± 0.33 K, 2011.81 K ± 0.35 K and 2011.66 K ± 0.26 K for the NPL, NMIJ and LNE-INM/CNAM cell, while the measurement result at NIST for the NPL cell was 2011.21 K ± 0.27 K. In contrast to the result at the Co-C point, the average thermodynamic temperature for Pt-C in this work is in very good agreement with the PTB results but deviates from the NIST result within the measurement uncertainty.

With respect to Re-C, only the measurement result at NIST is now available for the small opening cells with the thermodynamic temperature of 2747.17 K ± 0.51 K, significantly lower than that in this work by more than 1 K, but within the expanded uncertainty with $k = 2$. The differences in thermodynamic temperature in this case were probably caused due to the different set of fixed-point cells.

Table 7.4 Summary of the previous thermodynamic temperature determinations of the eutectic points with the expanded uncertainty, $k = 2$.

High-temperature fixed-points	Thermodynamic temperature (K)			
	Machine et al. [96]	Anhalt et al. [5]	Battuello et al.[97]	This work
Co-C	1597.43 ± 0.17	1597.18 ± 0.23	1597.27 ± 0.17	1597.47 ± 0.46
Pt-C	2011.21 ± 0.27	2011.73 ± 0.33	-	2011.65 ± 0.71
Re-C	2747.17 ± 0.51	-	-	2748.22 ± 1.31

7.4.2 Comparison on the same cell

As mentioned before, this measurement was performed in parallel to the established measurement using filter radiometers, therefore the thermodynamic temperatures obtained from both methods can be directly compared. Moreover, two sets of cells for each material have been sent to other NMIs for the purpose of the WP4 of the HTFP. However, at this stage, the comparison has been performed only with the results using the PTB filter radiometers i.e. FR676 and FR800. Because of different values in measurement uncertainty, the comparison reference values for both measurements, were derived by weighting the individual values with the measurement uncertainties. At each fixed point temperature, deviations from these values for all measurements are shown in **Fig.** 7.5.

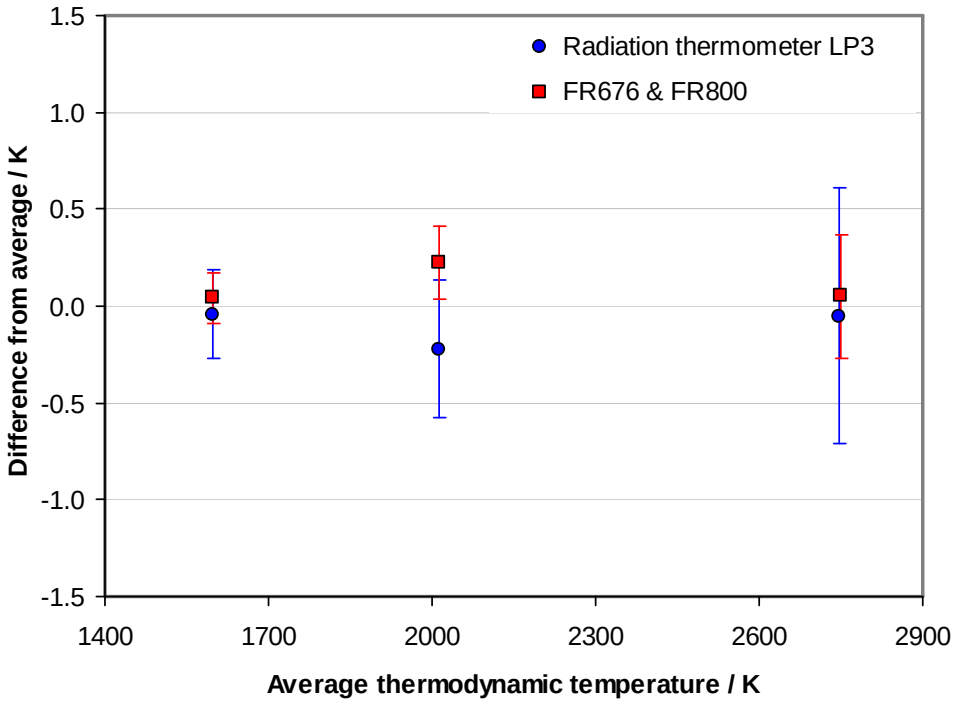

Figure 7.5 Comparison results of the thermodynamic melting temperatures along with the standard uncertainty (k = 1) for a set of the Co-C, Pt-C and Re-C fixed-point cells

It can be clearly seen from **Fig.** 7.5 that the measurement results in this work are in good agreement with the results using the PTB filter radiometers, especially for Co-C and Re-C. The agreement is within 90 mK at the Co-C point and 100 mK at the Re-C point, while it is more than 400 mK at the Pt-C point. For the large difference at the Pt-C fixed-point, more measurement results from the other NMIs and repeated measurements at PTB are needed to evaluate the accuracy of the measurements. However, more comparable results were found in comparison to the results from the different cells in 7.4.1 for Co-C and Re-C.

7.5 Conclusions

The absolutely calibrated radiation thermometer LP3 was used to measure the thermodynamic melting point temperatures of the Co-C, Pt-C and Re-C small fixed point cells manufactured by different NMIs. The measured photocurrents from the LP3 at the fixed-point temperatures were corrected by the blackbody emissivity and also the size of source effect before calculating the thermodynamic temperatures. The measurement uncertainties were also calculated for each cell, including the standard uncertainty of the LP3 absolute calibration. The average thermodynamic melting point temperatures and associated standard uncertainties (k = 1) for each material were 1597.47 K $\pm$ 0.23 K, 2011.65 K $\pm$ 0.35 K and 2748.22 K $\pm$ 0.66 K for Co-C, Pt-C and Re-C respectively. The reproducibility in temperature of these fixed-points from different manufactures was 64 mK, 105 mK and 149 mK for Co-C, Pt-C and Re-C respectively.

In comparison to the previous thermodynamic temperature determinations on the other cells, the average thermodynamic temperatures of each material were in agreement to the previous measurements by NIST using the AP1 for the Co-C and also consistent to the last measurements by PTB using the filter radiometers for the Pt-C. However the difference from the NIST result for Re-C was larger than the standard measurement uncertainty, but well within the expanded measurement uncertainty.

Furthermore, with the same set of fixed-point cells, the differences in thermodynamic temperature from the weighted mean obtained from this work and the results using filter radiometers were within 80 mK at the Co-C point and 100 mK at the Re-C point, while more than 400 mK were obtained at the Pt-C point. From the very good agreement at the Co-C and Re-C point, it is possible to revise the measurement uncertainty in this approach in case the difference at the Pt-C point is still within the combined uncertainty.

In conclusion, the new approach using the absolutely calibrated LP3 has high potential to determine the thermodynamic temperatures of small area eutectic fixed-point blackbodies. However, the uncertainty associated with the absolute responsivity calibration both, on the monochromator-based facility and the laser-based facility, has to be reduced before it can be comparable to that using the filter radiometer. Moreover, for accurate thermodynamic temperature determination of the eutectic fixed-points, the long-term stability of the LP3 could be a main component of uncertainty, therefore the absolute calibration should be performed just before and after the measurement at the high temperature fixed-points.

8 Summary

In this work, an absolute calibration set-up based on a monochromator and an integrating sphere has been developed for the first time in order to calibrate radiation thermometers with respect to absolute radiance responsivity. At this newly developed set-up, a high accuracy high-temperature radiation thermometer was absolutely calibrated against a Si trap detector, traceable to the PTB primary cryogenic radiometer. In the second step, the absolutely calibrated radiation thermometer was applied to determine the thermodynamic phase-transition temperatures of an already established Au and a Cu fixed-point blackbody and, finally, to novel high-temperature fixed-points.

The concept of the developed set-up was formulated by taking advantages from both lamp-monochromator-based systems and integrating sphere-based systems illuminated with monochromatic radiation. Firstly, the single-monochromator was used to select the spectral radiation with an optimized bandwidth for any types of radiation thermometers to avoid the interference fringes in spectral responsivity, obviously observed at the laser-based systems. Secondly, the integrating sphere was applied to produce the quasi-lambertian radiation for absolute calibration in terms of spectral radiance responsivity. Since the integrating sphere was employed, a variety of broadband light sources was tested to obtain the highest spectral output power from the monochromator in the desired wavelength range. The optical flux obtained from the monochromator-based set-up is now available from 0.1 μW/nm to 10 μW/nm in the wavelength range from 370 nm to 720 nm, depending on the light source used. At this stage, the 75 W Xe lamp was found to be optimum in terms of the output power and also the stability.

In order to measure the spectral irradiance from the sphere exit port at a reference plane, the Si trap detector, whose spectral power responsivity traceable to the SI units at the PTB primary cryogenic radiometer, was used as a transfer detector. With the two diamond-turned precision apertures of nominal 5 mm in diameter installed in front of the trap and the sphere opening, the spectral radiance can be calculated in case the aperture diameters and the distance between the two apertures are accurately known. In this work, a linear gauge and an interferometer were used in combination to measure the absolute distance, traceable to the metre. With respect to the accuracy of the set-up, all factors contributing to the measurement uncertainty were carefully investigated i.e. the radiance uniformity across the sphere opening, the distance effect and the diffraction error. However, unknown systematic errors may still be present in this set-up, therefore, further investigations must be performed in future work.

Before absolute calibrations at the developed set-up, two LP3 radiation thermometers were investigated for their relative spectral responsivity without the integrating sphere to find out the optimum spectral bandwidth of the LP3 radiation thermometers and also prove the performance of the single-monochromator. The best one of them was chosen to be

absolutely calibrated against the trap detector on the monochromator-based set-up and also on the tuneable laser-based facility (TULIP) of PTB for comparing the calibration results.

Because of the low optical flux in the monochromator-based set-up (<10 μW/nm), the measured out-of-band responsivity of the LP3 is limited to approximately 10^{-5} of the peak response, while it can be lower than 10^{-7} on the laser-based system, especially in the near infrared region. From an approximation, that difference contributes to only 20 mK temperature difference at the Au point. However, although the laser-based facility has a number of advantages, in particular the high-power and the low wavelength uncertainty, the extremely small bandwidth of the laser yields the interference fringes around the peak of the LP3 spectral responsivity with a maximum amplitude of larger than 1 %. In contrast, the interference fringes can be avoided on the monochromator-based set-up by the use of spectral bandwidth of larger than 0.2 nm.

With respect to the spectral responsivity of the test LP3, direct comparisons can be performed by averaging the results on TULIP over the finite wavelength, equivalent to the spectral bandwidth at the monochromator-based set-up. Relative differences in spectral responsivity were found to be within their combined uncertainty around the peak wavelength. In terms of integral responsivity, the relative difference obtained on both facilities is also within their combined uncertainty. In addition, with respect to the effective wavelength, the difference on both facilities is less than $\pm$13 pm, within the uncertainty of the wavelength calibration.

At this stage, the relative standard uncertainty (k = 1) obtained on the monochromator-based set-up is 0.17 %, slightly larger than the 0.14 % of the laser-based facility. We believe that the measurement attempting to avoid the interference effects could yield the lower uncertainty with more reasonable time-consumption. An increase of the output radiant power from the monochromator and an improvement of the radiance uniformity across the sphere opening can significantly reduce the uncertainty to reach the target of 0.12 % (k = 1), equivalent to the theoretically limited uncertainty of ITS-90. However, within this work, an independent thermodynamic temperature scale has been realized using the absolutely calibrated radiation thermometer.

In order to validate the absolute calibrations, the radiation thermometer LP3 was used to measure the PTB primary Au fixed-point (1337.33 K) and a small Cu fixed-point blackbody (1357.77 K). The influences of the different source areas and the signal levels between the absolute calibration and the measurement at the fixed-points, were considered and carefully corrected. Using the calibration result at the monochromator-based set-up, the determined thermodynamic temperatures with the standard uncertainties of 0.16 K (k = 1), are in agreement with the defined temperature values in the ITS-90. Furthermore, the temperature differences from the ITS-90 values (T-T_{90}), especially at the gold fixed-point are in very good agreement with the current value reported by the CCT WG4 of BIPM. Using the calibration result at the laser-based set-up, the temperature uncertainties of less than 0.14 K were obtained at the Au point and the Cu point, and the determined thermodynamic temperatures of the two fixed-points are in larger discrepancy to the ITS-

90 values than using the result at monochromator-based set-up but still within the expanded uncertainties ($k = 2$).

Finally, the absolutely calibrated LP3 was applied to determine thermodynamic phase-transition temperatures of a set of small aperture size eutectic fixed-points namely Co-C, Pt-C and Re-C with the obtained measurement uncertainty of 0.66 K ($k = 1$) for the temperature up to 2748 K. The observed repeatability of the melting point temperature for all Co-C and Pt-C cells was within 30 mK, while it was better than 61 mK for all Re-C cells. The reproducibility was better than 100 mK for Co-C, Pt-C and 200 mK for Re-C. This confirms that these fixed-points are indeed reliable candidates for an improved International Temperature Scale at high temperatures. In addition, the thermodynamic melting temperatures in this work are consistent with the measurements based on filter radiometers, but with about two times larger measurement uncertainties. The differences in thermodynamic temperature from the weighted mean obtained from the two methods were within the combined standard uncertainties ($k = 1$). Therefore, it has been now confirmed that no systematic differences in thermodynamic temperature between the direct method using imaging radiation thermometer and the indirect method using filter radiometers exists. This agreement will be a fundamental knowledge for the next step of the HTFP research plan of the CCT-WG5.

This present work has shown a possible path for small NMIs to establish an absolute radiance calibration facility using a monochromator and an integrating sphere – by using calibrated trap transfer detectors from another NMI or calibrating their own trap transfer detectors at another NMI – and resulting with measurement uncertainties comparable to laser-based facilities, yet at a more reasonable time-consumption. The absolutely calibrated radiation thermometer can then be directly used for a practical realization of the thermodynamic temperatures above 1357.77 K as an alternative to the current International Temperature Scale at high temperatures. In additions, this approach has potential to be used as a direct method of practical realization for the definition of the kelvin at high temperatures (*MeP*-K HT) without any high-temperature fixed-points.

Bibliography

1. T.J. Quin, C. Fröhlich, Accurate radiometers should measure the output of the Sun, *Nature* **401**, 481 (1999).
2. H. Preston-Thomas, The International Temperature Scale of 1990 (ITS-90), *Metrologia*, **27**, 3-10 (1990).
3. Y. Yamada, H. Sakate, F. Sakuma, A. Ono, Radiometric observation of melting and freezing plateaus for a series of metal-carbon eutectic points in the range 1330 C to 1950 C, *Metrologia* **36**, 207-209 (1999).
4. D.R. Taubert, R. Friedrich, J. Hartmann, J. Hollandt, Improved calibration of the spectral responsivity of interference filter radiometers in the visible and near infrared spectral range at PTB, *Metrologia* **40**,S35-S38 (2003).
5. K. Anhalt et al, Thermodynamic temperature determinations of Co–C, Pd–C, Pt–C and Ru–C eutectic fixed-point cells, *Metrologia* **43**, 78-83 (2006).
6. http://www.bipm.org/cc/CIPM/Allowed/94/CIPM-Recom2CI-2005-EN.pdf
7. J. Fischer, B. Fellmuth, Temperature metrology, *Rep. Prog. Phys.* **68**, 1043-1094 (2005).
8. O. Tamura, S. Takasa, T. Nakano, H. Sakurai: Int. J. Thermophys. **29**, 31–41 (2008).
9. R. E. Edsinger and J. F. Schooley, Differences between thermodynamic temperature and *t* (IPTS-68) in the range 230 ◦C to 660◦C, *Metrologia* **26** 95–106 (1989).
10. L. Pitre. M.R. Moldover, and Tew: *Metrologia* **43**, 142-162 (2006).
11. D. C. Ripple, G. F. Strouse, M. R. Moldover: Int. J. Thermophys. **28**, 1789–1799 (2007).
12. C. Gaiser, B. Fellmuth, N. Haft: Int. J. Thermophys. **29**, 18–30 (2008).
13. J. R. Labenski, W. L. Tew, S. P. Benz, S. W. Nam, P. D. Dresselhaus: Int. J. Thermophys. **29**, 1–17 (2008).
14. F. Edler, M. Kühne, and E.Tegeler, *Metrologia* **41**, 47-55 (2004).
15. T. J. Quinn and J. E. Martin, *Phil. Trans. R. Soc.* **316** 85–189 (1985).
16. J. E. Martin, T. J. Quinn, Chu: *Metrologia* **25**, 107-112 (1988).
17. H. W. Yoon, Gibson, Allen, Saunders, Litorja, Brown, Eppeldauer and Lykke, *in Proceeding of Tempmeko 2004*, 59-70.
18. J. Hartmann, K. Anhalt, P. Sperfeld, J. Hollandt, M. Sakharov, B. Khlevnoy, Yu. Pikalev, S. Ogarev, V. Sapritsky, Thermodynamic measurements for melting curves of Re-C, TiC-C, and ZrC-C eutectics, *in Proc. of Tempmeko 2004*, 189-194.
19. http://www.bipm.org/utils/en/pdf/MeP_K.pdf
20. R. L. Rusby, R. P. Hudson, M. Durieux, K. Grohmann, H.J. Jung, P. P. M.Steur, and J. V. Nicholas, "The status of thermodynamic thermometry", *Metrologia*, **33**, 409-414 (1996).
21. O. Lummer, E. Pringsheim, Energieverteilung im Spectrum des schwarzen Körpers und des blanken Patins, Verhandl. D. deutschen Physik. Gesell. 1 (1899) 215-235.
22. M. Planck, Ueber eine Verbesserung der Wien'schen Spectralgleichung, *Verh. Deutsch. Phys. Ges.* **2** (1990) 202-204.
23. W. Wien, Über die Energieverteilung im Emissionspectrum eine schwarzen Körpers, Ann. Phy. Chem. 58 (1896) 662-669.
24. L. Rayleigh, Philos. Mag. Ser. 5 49 (1900) 539-540.
25. L. Boltzmann, Ableitung des Stefanschen Gesetzes, betreffend die Abhängigkeit der Wärmestrahlung von der Temperatur aus der elektromagnetischen Lichttheorie. Ann. Phys. Ser. 2, 22Ann. (1884) 291-294.
26. J. Stefan, Über die Beziehung zwischen der Wärmestrahlung und der Temperatur. Sitzungsber. Akad. Wiss. Wien 79 Teil 2, (1879) 391-428.

27. G. Bauer, K. Bischoff, Evaluation of the emissivity of a cavity source by reflection measurements, *Appl. Opt*. 10 (1971) 2639-2643.
28. A.V. Prokhorov, Monte Carlo method in optical radiometry, *Metrologia* **35** (1998) 465.
29. J. Ishii, M. Kobayashi, F. Sakuma, Effective emissivities of blackbody cavities with grooved cylinders, *Metrologia* **35** (1998) 175-180.
30. R.E. Bedford, C.K. Ma, Emissivities of diffuse cavities: Isothermal and nonisothermal cones and cylinders, J. Opt. Soc. Amer. 64 (1974) 339-349.
31. J. Hartmann, D. Taubert, Assessing blackbody emissivity by Monte Carlo simulation, in Proceeding of Infrared Sensors and Systems (2002) 133-138.
32. R. Friedrich J. Fischer, New spectral radiance scale from 220 nm to 2500 nm, *Metrologia* **37** (2000) 539-542.
33. T.J. Quinn, *International report: News from the BIPM*, *Metrologia* **34**,pp. 187-194 (1997).
34. K. Anhalt, Y. Wang, Y. Yamada, J. Hartmann, Int. J Thermophys. **29**, 969-983 **(**2008).
35. Y. Yamada , B.B. Khlevnoy, Y. Wang, T. Wang, and K. Anhalt, Application of metal (carbide)–carbon eutectic fixed points in radiometry, *Metrologia* **43** S140–144 (2006).
36. R. Friedrich J. Fischer, and M. Stock, Accurate calibration of filter radiometers against a cryogenic radiometer using a trap detector. *Metrologia* **32** (1995/96) 509-513.
37. Fu. Lei, J. Fischer, Characterization of photodiodes in the UV and visible spectral region based on cryogenic radiometry, *Metrologia* **30** (1993) 297-303.
38. L. Werner, J. Fischer, U. Johannsen, J. Hartmann, *Metrologia*, **35**, 407-411 (1998).
39. N.P. Fox, Trap detectors and their properties, *Metrologia* **28** (1991) 197-202.
40. J. Hartmann, J. Fischer, U. Johannsen, L. Werner, Analytical model of the spectral responsivity of silicon, J. Opt. Sco.Am. B18 (2001) 942-947.
41. L. Werner, J. Fischer, U. Johannsen, J. Hartmann, Accurate determination of the spectral responsivity of silicon trap detectors between 238 nm and 1015 nm using a laser-based cryogenic radiometer, *Metrologia*, **37**, 279-284 (2000).
42. N.P. Fox, J.E. Martin, Comparison of two cryogenic radiometers by determining the spectral responsivity of silicon photodiodes with an uncertainty of 0.2 %, *Applied Optics*, **29**(31), 4686-4693 (1990).
43. N. Noulkhow, R.D. Taubert, P. Meindl, J. Hollandt, Int. J. Thermophys. **30**, 131 (2009).
44. M. Stock, J. Fischer, R. Friedrich, H.J. Jung, B. Wende, Metrologia **32**, 441 (1995/96).
45. G.Machin, P. Bloembergen, K. Anhalt, J. Hartmann, M. Sadli, P. Saunders, E.Woolliams, Y. Yamada, H. Yoon, Realization and Dissemination of Thermodynamic Temperature Above 1234.93 K. CCT/10-12rev1 (2010). http://www.bipm.org/cc/CCT/Allowed/25/D12r_MeP-HT_v8.pdf
46. S.W. Brown, G.P. Eppeldauer and K.R. Lykke, Facility for Spectral Irradiance and Radiance Responsivity Calibrations with Uniform Sources, *Applied Optics* **45**, 8218-8237 (2006).
47. R. Winkler, E R Woolliams, W S Hartree, S G R Salim, N P Fox, J R Mountford, Malcolm White, S R Montgomery, Calibration of an Absolute Radiation Thermometer for Accurate Determination of Fixed-Point Temperatures, Int J Thermophys **28,** 2087-2097 (2007).
48. Y Ichino, I Saito, Y. Yamada, J. Ishii, Spectral radiance responsivity calibration facility for thermodynamic temperature determination, *in Proceedings of Tempmeko 2007*, (Lake Louise, Canada, 2007).
49. C-W Park, D-H Lee, S-N Park, S Par Park, Laser-based radiance standard source for measuring the absolute responsivity of a radiation thermometer, *in Proceedings of Tempmeko 2007*, (Lake Louise, Canada, 2007).
50. K. Anhalt, A. Zelenjuk, D. R. Taubert, T. Keawprasert, J. Hartmann, New PTB Setup for the Absolute Calibration of the Spectral Responsivity of Radiation Thermometers, Int J Thermophys **30**, 192-202 (2009).

51. T. Keawprasert et al., Absolute Calibration of Spectral Responsivity for a Radiation Thermometer, in *Proceedings of the 10th International Conference on New Developments and Applications in Optical Radiometry (NEWRAD)*, ed. by Dong-Hoon Lee (KRISS, Daejong, Korea, 2008), p. 287.
52. V.E. Anderson, N.P. Fox, D.H. Nettleton, Highly stable, monochromatic and tuneable optical radiation source and its application to high accuracy spectrophotometry, *Appl. Opt.* **31**, 536 (1992).
53. A. Sperling, O. Larionov, U. Grusemann, S. Winter, in *Proceedings of the 9th International Conference on New Developments and Applications in Optical Radiometry (NEWRAD)*, ed. by J. Groebner (PMODWRC, Davos, Switzerland, 2005), p. 93.
54. V. Ahtee, S.W. Brown, T.C. Larson, K.R. Lykke, E. Ikonen, and M. Noorma, Comparison of absolute spectral irradiance responsivity measurement techniques using wavelength-tuneable lasers, *Applied Optics* **40**, 4228-4236 (2007).
55. H.W. Yoon et al., Thermodynamic-radiation thermometry for the next SI, Int J Thermophys **29**, 285-300 **(**2008).
56. O. Schiek and E. Winter, Two new mirror monochromators, *Applied Optics* **4**, 195-199 (1965)
57. http://www.energetiq.com/DataSheets/EQ1500_1510_Data_Sheet_.pdf
58. http://www.technoteam.de/products/lmk_luminance_measuring_camera/lmk_98_4_color/index_eng.html
59. S. Briaudeau, B. Rougie, M. Sadli, A. Richard and J.M. Coutin, Optical diffraction corrections in radiometric thermodynamic temperature determination, Int J Thermophys **30**:155-166 (2009).
60. J. Hartmann, J. Fischer and J. Seidel, A non-contact technique providing improved accuracy in area measurements of radiometric apertures, *Metrologia* **37**, 637-640 (2000).
61. W.H. Steel, M. De, J.A. Bell, Diffraction corrections in Radiometry, *J. Opt. Soc. Am.* **62**, 1099 (1972).
62. L.P. Belvin, Diffraction corrections in the radiometry of extended sources, *Applied Optics* **15**, 1204-1209 (1976).
63. J.T. Woodward, A.W. Smith, C.A. Jenkins, C. Lin, S.W. Brown and K.R Lykke, Supercontinuum sources for metrology, *Metrologia* **46**, 277–282 (2009).
64. http://www.newport.com/CatalogPDF/e5548.pdf
65. J. Hartmann, High-temperature measurement techniques for the application in photometry, radiation thermometry and thermometry, Physics Reports 469 205-269 (2009).
66. M. S. Lima, R. N. Teixeira, A. P. Cunha, I. B. Couceiro, Spectral responsivity calibration of the linear pyrometer at Immetro, , in *Proceedings of XVIII IMEKO* (Rio de Janeiro, 2006).
67. *A Guide to Integrating Sphere Theory and Applications*, Labsphere.
68. H. Louis-Philippe Bolvin, .Study on bandwidth effects in monochromator-based spectral responsivity measurements, *Applied Optics* **41**, 1929-1935 (2002).
69. H.C. McEvoy, EUROMET.T-S1 Final Report, NPL Report ENG 2 (2007).
70. F.A. Jenkins and H.E. White, Fundamentals of Optics, 4E, McGraw-Hill, 1976.
71. www.bipm.org/cc/CCT/Allowed/24/D13_rev_WG4_report_CCT_25_June_2008.
72. N. P. Fox, J. E. Martin, and D. H. Nettleton, Absolute spectral radiometric determination of the thermodynamic temperatures of the melting freezing points of gold, silver and aluminium, *Metrologia* **28**, 357–374 (1991).
73. R. Goebel, Y Yamada and M. Stock, in *Proceedings of Tempmeko 2004*, ed. by D. Zvizdic, L.G. Bermanec, T. Veliki, T. Stasic (FSB/LPM, Zagreb,2004), pp. 91-99.
74. H.W. Yoon et al., Thermodynamic-temperature determinations of the Ag and Au freezing temperatures using a detector-based radiation thermometer, *Applied Optics* **46**, 2870-2880 (2007).

75. M. Battuello, M. Florio and F. Girare, Int. J Thermophys, DOI 10.1007/s10765-010-0784-y
76. M. Battuello, M. Florio and F. Girare, *Metrologia* **47**, 231-238 (2010).
77. F. Edler, M. Kühner, E. Tegeler, Noise Thermometry above 960 °C, in *Proceedings of Tempmeko 1999*, ed. by Dubbeldam J. F., de Groot, M. J., (Delft,1999) pp. 394-399.
78. D.R. Taubert, J. Hartmann, J. Hollandt, J. Fischer, in *Temperature, Its Measurement and Control in Science and Industry*, vol 7, part 1, ed. by D. Ripple (AIP, New York, 2002), 7–12.
79. H. J. Jung and J. Verch. Ein Rechenverfahren zur Auswertung pyrometrischer Messungen. Optik, (38):95{109, 1973.
80. F. Sakuma, M. Kobayashi, in *Proceedings of Tempmeko 1996*, ed. by P. Marcarino (Levrotto and Bella, Torino, 1997), 305-310.
81. P. Saunders, D.R. White, *Metrologia* **27**, 41 (2004).
82. L. Bünger, Untersuchung und Anwendung von Hochleistungsleuchtdioden für die Bestimmung der nichtlinearität der spektralen Empfindlichkeit von Photodioden und Strahlungsthermometern, Diplomarbeit, University of Applied sceinces Berlin (2008).
83. J. Fischer and L. Fu, *Appl. Opt.* **32** 4187–4190 (1993).
84. J. Fischer and H. J. Jung, Determination of the Thermodynamic Temperatures of the Freezing Points of Silver and Gold by Near-Infrared Pyrometry, *Metrologia* **46**, 245–252 (1989).
85. H.C. McEvoy, G. Machin, R. Friedrich, J. Hartmann, J. Hollandt, Comparison of the new NPL primary standard Ag fixed-point blackbody source with the primary standard fixed-point of PTB, in *Proceeding of Temperature*, 909-914 (2003).
86. Y. Yamada, H. Sakate, F. Sakuma and A. Ono, A possibility of practical high temperature fixed points above the copper point *Proc. 7th Int. Symp. on Temperature and Thermal Measurements in Industry and Science (Tempmeko)* (Delft, The Netherlands: IMEKO/NMi) pp 535–40 (1999).
87. Y. Yamada, H. Sakate, F. Sakuma and A. Ono, High-temperature fixed points in the range 1150 °C to 2500 °C using metal–carbon eutectics, *Metrologia* **38** 213–219 (2001).
88. G. Machin, Y. Yamada, D. Lowe, N. Sasajima, K. Anhalt, J. Hartmann, R. Goebel, H.C. McEvoy and P. Bloembergen,2004, A comparison of high temperature fixed-points of Pt–C and Re–C constructed by BIPM, NMIJ and NPL *Proc.9th Int. Symp. on Temperature and Thermal Measurements in Industry and Science (Tempmeko) (Dubrovnik)* (Zagreb, Croatia: Laboratory for Process Measurement, Faculty of Mechanical Engineering and Naval Architecture) 1049–56.
89. K Anhalt, J. Hartmann J, D. Lowe, G. Machin, M. Sadli, Y. Yamada and P. Bloembergen, 2005 A comparison of Co–C, Pd–C, Pt–C, Ru–C and Re-C eutectic fixed points independently manufactured by three different institutes *Proc. Newrad (Davos, Switzerland)* (Physikalisch-Meteorolgisches Observatorium Davos) pp 289–90.
90. N. Sasajima, H.W.Yoon, C.E. Gibson, V.B. Khromchenko, F. Sakuma and Y. Yamada, The NIST eutectic project: construction of Co–C, Pt–C and Re–C fixed-point cells and their comparison with the NMIJ *Metrologia* **43,** S109–14 (2006).
91. D. Lowe and Y. Yamada, Reproducible metal–carbon eutectic fixed-points *Metrologia* **43** S135–9 (2006).
92. P. Bloembergen, B. B. Khlevnoy, P. Jimeno Largo, Y Yamada, Spectral and total effective emissivity of a high-temperature fixed point radiator considered in relation to the temperature drop across its back wall, Int J Thermophys **29**, 370-385 (2008).
93. P. Jimeno-Largo, Y. Yamada, P. Bloembergen, M. Villamanan and G. Machin, Numerical analysis of the temperature drop across the cavity bottom of high temperature fixed-points for radiation thermometry *Proc. 9th Int. Symp.on Temperature and Thermal Measurements in Industry and Science (Tempmeko) (Dubrovnik)* (Zagreb, Croatia: Laboratory for Process Measurement, Faculty of Mechanical Engineering and Naval Architecture) pp 335–340 (2004)

94. G. Machin, L. Wright, D. Lowe, J. Pearce, Optimizing the implementation of high temperature fixed points through the use of thermal modeling, Int J Thermophys **29**,261-270 (2008).
95. J. Hartmann and J. Fischer, Improved thermal stability of the linear pyrometer LP3 for high temperature measurements within the EU-project HIMERT, *VDI Berichte* 1784, 201-206 (2003).
96. G. Machin, C.E. Gibson, D. lowe, D.W. Allen, and H.W. Yoon, A comparison of ITS-90 and detector-based scales between NPL and NIST using metal carbon eutectics, 2004, *Proc. 9th Int. Symp.on Temperature and Thermal Measurements in Industry and Science (Tempmeko) (Dubrovnik)* (Zagreb, Croatia: Laboratory for Process Measurement, Faculty of Mechanical Engineering and Naval Architecture) pp 1057–1062.
97. M Battuello, F Girard and M Florio, Extrapolation of radiation thermometry scales for determining the transition temperature of metal–carbon points. Experiments with the Co–C, *Metrologia* **46,** 26–32 (2009).

Acknowledgement

Firstly, I would like to express my gratitude to Prof. Dr. Jürgen Hartmann and Prof. Dr. Stephan Völker for supervising this PhD thesis and Prof. Dr. Heinrich Kaase for accepting me as a PhD candidate at the section of Lighting Engineering in the Faculty of Electrical Engineering and Computer Science at the Technical University of Berlin.

I am deeply grateful to Dr. Jörg Hollandt for providing me the opportunity to do research at the Physikalisch-Technische Bundesanstalt Berlin, Dr. Klaus Anhalt for his continuous support and discussion since my first day in Berlin and to Dr. Dieter Taubert for his scientific support and helpful teaching. Their support helped substantially to gain more experience especially in the fields of radiation thermometry and absolute radiometry. In addition, I would also like to thank all the other colleagues in the department 7.3 Detector Radiometry and Radiation Thermometry for providing the technical infrastructures as well as a professional and friendly environment.

Since this work was partially performed in the working group 4.12 Photometry at the PTB Braunschweig, I would like to thank Dr. Armin Sperling for the opportunity to perform the measurements at the TULIP facility. I would also like to thank Dr.Alaa Abd-ElMageed, Michaela Schuster, Dr. Saulius Nevas and Dr. Stefan Winter for their measurements at the TULIP facility and their helpful discussions.

Furthermore, I would like to thank my employer the National Institute of Metrology Thailand, for opening the opportunity to deepen my research work and studies for a PhD degree, and the Ministry of Science and Technology Thailand for funding my scholarship in Germany.

Finally, I would like to thank my family for their wonderful and motivating support, especially my wife, Thasorn Sinhaneti, she means so much to me.